# Seismic Structure of the Mantle Beneath the Pacific Hemisphere

A DISSERTATION
SUBMITTED TO THE FACULTY OF THE GRADUATE SCHOOL
OF THE UNIVERSITY OF MINNESOTA
BY

Brian C. Bagley

IN PARTIAL FULFILLMENT OF THE REQUIREMENTS
FOR THE DEGREE OF
Doctor of Philosophy

Justin Revenaugh, Adviser

June, 2011

# Acknowledgements

I could never have completed this dissertation without the support and guidance of my advisor, Justin Revenaugh. He has always made time to provide me with assistance whenever needed, and has always provided feedback in a timely manner. He has made sure that I always had enough time to complete my research by keeping my other responsibilities at a reasonable level. I also thank Justin for making me do most of the final work independently, this has allowed me to gain confidence in my ability to continue my research career independently.

Thanks are due to the staff members that make our department run smoothly. Especially Sharron Kressler, who is is always available and able to solve problems. I also thank the members of my written, oral, and final examination committees for their work. Members of these committees include David Kohlstedt, Marc Hirschmann, and Martin Saar.

I thank Anna Courtier for helping me get started in the seismology group, her assistance was invaluable, and I enjoyed working with her. I am grateful to Lars Hansen, Andrew Haveles, and Joe Myre for insightful discussions about my research, providing assistance with LaTeX, and their friendship. I also thank Greg Beroza for providing advice on tremor related research.

The friendship of Tim Courtier, Nick Olds, Aaron Burnett, Elissa Hansen, Allison Burnett, David Fox, Lindsay Fox, and Annia Fayon is also much appreciated. It has been a pleasure to have such a good group of friends.

Much of my graduate career was funded through fellowships. This support was essential and afforded my the time necessary to complete this research. I benefited from Dennis, Murthy-Noruck, and Mooney fellowships awarded by the Department of Geology and Geophysics.

Finally, I would like to thank my family for their support. My wife, Tiffany, has made many sacrifices that made my academic career possible. She has been supportive and encouraging throughout, and I deeply appreciate it. My parents have

always been supportive, and I thank them for their help along the way. I have enjoyed all of their many visits to Minnesota over the past few years.

Chapter 1 acknowledgements: Arwen Deuss supplied the SS-precursor data used in Figure 4. The seismic data presented here was collected from Incorporated Research Institutions for Seismology (IRIS). We wish to thank Cecily Wolfe and the Ocean Hemisphere Project for supplying additional data. GMT software (Wessel and Smith, 1998) was used to prepare some of the figures. Centroid Moment Tensors were provided by Harvard University. This research was supported by NSF Geophysics EAR-0437424. This work began while Bagley was a NSF REU summer intern at the University of Minnesota.

Chapter 2 acknowledgements: GMT software (Wessel and Smith, 1998) was used to prepare some of the figures. The Incorporated Research Institutions for Seismology (IRIS), Ocean Hemisphere Project (OHP), and F-Net supplied data. This research was supported by NSF grant EAR-0437424. Courtier benefited from a Doctoral Dissertation Fellowship at the University of Minnesota.

Chapter 3 acknowledgements: The facilities of the IRIS Data Management System, and specifically the IRIS Data Management Center, were used for access to waveform and metadata required in this study. GMT software (Wessel and Smith, 1998) was used to prepare some of the figures. This research was supported by NSF grant EAR-0437424. Courtier benefited from a Doctoral Dissertation Fellowship at the University of Minnesota. Bagley was partially supported by a Fellowships from Harold Mooney and V. Rama Murthy and Janice Noruk.

Chapter 4 acknowledgements: Data preprocessing was completed using Seismic Access Code (Goldstein, P., A. Snoke, 2005; Goldstein, P., D. Dodge, M. Firpo, Lee Minner, 2003). Some of the figures were created using Generic Mapping Tools (Wessel and Smith, 1998). The facilities of the IRIS Data Management System, and specifically the IRIS Data Management Center, were used for access to waveform and metadata required in this study. Data from the TA network were made freely available as part of the EarthScope USArray facility supported by the National Science Foundation, Major Research Facility program under Cooperative Agreement EAR-0350030. HRSN data were made available by Berkeley Seismological Laboratory, University of California, Berkeley the Northern California Earthquake Data Center (NCEDC). The Pacific Northwest Seismic Network monitors seismicity in the states of Washington and Oregon (USA) with support from the U.S. Geological Survey, U.S.

Department of Energy and the State of Washington. This research was supported by NSF Geophysics EAR-0437424. Bagley was partially supported by a Fellowships from Harold Mooney and V. Rama Murthy and Janice Noruk.

# Contents

# List of Tables

# List of Figures

# Chapter 1

# Introduction to the thesis

Aside from xenoliths, the Earth's mantle is a region that is inaccessible directly, leaving us with limited tools to investigate its characteristics indirectly. Seismology is a tool well-suited for this purpose, and has provided valuable insight regarding many fundamental processes occurring within the mantle. It is fortuitous that the mantle is layered, and that these layers are often punctuated by distinct changes in density and/or velocity that are seismically detectable. By investigating the seismic structure of the mantle we are able to infer properties such as composition, temperature, anisotropy, and water content. Seismic tomography has informed our understanding of subduction and the fate of slabs, and we are beginning to realize that the lower mantle might also be rich with heterogeneity. Our picture of the Earth's mantle is becoming clearer, however, there is much that we do not understand.

Receiver function studies of the oceans are fewer and suffer the common malady of looking beneath oceanic islands, not generic oceanic crust. Most of the detailed information regarding the seismic discontinuity structure of open ocean mantle comes from bottom-side reflections that are precursors to SS phases (a shear wave that has traveled from source to receiver with one bottom-side surface bounce in between). SS and PP (a compressional wave with a path analogous to SS) precursors offer extensive geographic coverage and good sensitivity to small velocity contrasts and reasonable localization. They do not perform well for shallow reflectors, or reflectors near the larger transition zone discontinuities. In our studies we use multiple ScS reverberations to gain better resolution of these features.

The primary goals of this research are to study mantle discontinuities, and fill in some of the missing detail regarding mantle heterogeneity. We do this by examining

the Pacific ocean, beginning with the open ocean mantle, then moving to the subduction zones in the west Pacific. This region, containing the Boso Triple Junction, is one of the most complex subduction zones on the planet. Finally we continue west beneath the Sea of Japan, the Sea of Okhotsk, and the northeast Chinese craton. The changes in mantle structure across the Pacific reveal many interesting differences between the open ocean mantle and the mantle in regions of subduction.

Each chapter of this thesis is written as a separate scientific paper. The first chapter, *Upper mantle seismic shear discontinuities of the Pacific*, was published in Journal of Geophysical Research in 2008. This study focuses on upper mantle seismic structure, specifically the Gutenberg discontinuity, which marks the transition from the seismically fast lid to the low-velocity zone beneath. We observe a consistent impedance decrease at a depth of ∼80 km, over a depth interval of 30 km or less. This relatively sharp transition is difficult to reconcile with current mineral physics models, and suggests that partial melting might play a role. The X discontinuity, an impedance increase of 3–8% near 300 km depth, is present beneath much of the study area. Based on the apparent absence of melt atop the 410-km discontinuity, an intermittent and weak 520-km discontinuity and a thinned transition zone, we infer that the deep upper mantle of the central Pacific is relatively dry.

The second chapter, *Melting in the deep upper mantle oceanward of the Honshu slab*, was a joint project with Anna Courtier and was published in Physics of the Earth and Planetary Interiors in 2009. In this study we investigate the distribution of melt in the upper mantle and transition zone beneath the western Pacific. A low velocity zone is found above the 410-km discontinuity oceanward of the subducting Honshu slab at an average depth of 356 km, with a thickness that ranges from 50 km to 75 km assuming the low velocity zone continues to the 410-km discontinuity. We interpret this low velocity zone to be a layer of partial melt, oceanward of the Honshu slab. Our observations call for a maximum temperature anomaly of ∼50 °C and a resulting maximum olivine water content after melting of 0.100 wt. %.

The third chapter, *Seismic shear-wave structure of the mantle beneath northeast China and the northwest Pacific*, will soon be submitted for publication. In this work we extend the study region from to include the backarc side of the west Pacific trench systems, and northeast China. We also extend our search for discontinuities into the mid- to lower-lower mantle. We find an additional melt layer ∼65 km thick atop the 410-km discontinuity near the Nankai trench, which has similar characteristics to

melt layers observed on the oceanward side (Chapter 2). The transition zone contains a split 520-km discontinuity, possibly due to the accumulation of slab material in the transition zone. A negative reflector is found in one path beneath the northeast China craton at a depth of 598 km. Mid-mantle reflectors are found throughout the west Pacific and northeast China, and are present throughout a wide depth range (∼750–1600 km).

Finally, the last chapter, *Exploring the Geographic Distribution of Tremor: A Detection Algorithm for Sparsely Instrumented Regions*, will soon be submitted for publication. This work is unrelated to our previous mantle studies and addresses the need for an algorithm capable of detecting non-volcanic tremor (NVT) in regions that are sparsely instrumented. NVT is characterized by a weak and extended signal most prominent at 1–10 Hz. It is often correlated, both spatially and temporally, with slow-slip events along faults and populated with low-frequency earthquakes. Fault slip occurs globally in a diversity of tectonic environments, but many parts of the world are sparsely monitored; driving the need for a new detection method. Tremor is difficult to detect because it is a low amplitude transient signal, with amplitudes of ∼1 micron per second, that lack the sharp, impulsive body wave arrivals used to locate "regular" earthquakes. We have tested our method in two regions during periods of known NVT activity, with good results. A third test was conducted in a seismically quiet region to determine how the algorithm responds to various types of noise. The results of these tests are very promising, and after additional refinement (error analysis), this method should prove to be useful in the creation of a global catalog of NVT.

# Chapter 2

# Upper mantle seismic shear discontinuities of the Pacific

Brian Bagley and Justin Revenaugh
Department of Geology and Geophysics, University of Minnesota, 310 Pillsbury Drive SE, Minneapolis, MN 55455

This chapter has already been published and is reproduced by permission of American Geophysical Union. Bagley, B., and J. Revenaugh (2008), Upper mantle seismic shear discontinuities of the Pacific, Journal of Geophysical Research, 113(B12), 1-9, doi:10.1029/2008JB005692. 

Shear-wave impedance discontinuities are inventoried for eight paths connecting circum-Pacific earthquakes with seismic stations on Hawaii and Oahu. In addition to the transition zone discontinuities, we observe a consistent impedance decrease at a depth of ∼80 km that marks the transition from the fast seismic lid to the low-velocity zone. The interval over which this transition occurs is less than 30 km. The requisite impedance decrease, ascribed almost entirely to diminished velocities in the low-velocity zone, exceeds predictions for peridotite chemistries of appropriate lithospheric age. In all cases, the transition is better matched by lithosphere of roughly half of the true age. Four paths show clear evidence of the X discontinuity, an impedance increase of 3–8% near 300 km depth. The only viable explanations would require extensive eclogite or basalt-depleted mantle in the upper mantle of the western Pacific. The impedance contrast of the 410-km discontinuity, which depends on the modal fraction of mantle olivine, does not signal the presence of either, although a mixture of the two remains a possibility. We find no evidence of a low-velocity layer atop of the 410-km discontinuity. If present, it is either consistently thin ($\leq$ 15 km), highly variable in thickness (topography in excess of 60 km) or has little impedance contrast ($\leq$ 2–3%) with overlying mantle. The apparent absence of melt atop the 410-km discontinuity, an intermittent and weak 520-km discontinuity and a thinned transition zone are consistent with relatively dry conditions in the deep upper mantle of the central Pacific.

## 2.1 Introduction

The dichotomy of oceanic and continental hypsometry offers a stark visible reminder of the very different processes responsible for the creation of oceans and continents. The dichotomy is equally stark in their seismic structures (e.g., Jordan, 1979). Oceanic velocity structure largely hews to the formula of a fast, but thin, seismic lid underlain by low velocities that gradually recover with depth. Continental structure is more variable, but within tectonic categories, e.g., cratons, mobile belts, etc., there is predictability. High seismic velocities typically extend deeper; low-velocity zones are muted or absent at greater depth. Punctuating both are series of discontinuities, i.e., abrupt radial transitions in seismic velocity and other mechanical and transport properties. Under oceans, the Gutenberg (G) discontinuity (a velocity decrease at depths near 60  120 km) marks the transition between the seismic lid and the low-velocity zone (Revenaugh and Jordan, 1991c; Karato and Jung, 1998; Courtier and Revenaugh, 2007; Gaherty et al., 1996; Gung et al., 2003). While there is evidence of a possible analog under continents in the form of a region of enhanced scattering, higher attenuation and perhaps lower mean velocities (Thybo and Perchuc, 1997; Thybo, 2006), a simple G-like discontinuity is seldom seen. The Lehmann (L) discontinuity is observed under both, albeit with a preference for continents (Gu et al., 2001). Its origin(s) remains enigmatic and the designation L is applied to any velocity increases, typically small, between 150 and 250 km depth. Below L but above the 410-km discontinuity lies the X discontinuity, which, like L, designates any sharp velocity increase in its depth range (∼270–330 km). X is sighted less often than L and has no convincing tectonic bias. Neither do any of the transition zone discontinuities, which appear, from a strictly seismic perspective, outside the reach of continents and oceans.

In the last decade, receiver function studies of continental crust and mantle have refined this broad-brush understanding of seismic discontinuity structure (e.g., Bostock, 1996; Lawrence and Shearer, 2006; Chevrot et al., 1999; van der Meijde et al., 2005). Receiver function studies of the oceans are fewer and suffer the common malady of looking beneath oceanic islands, not generic oceanic crust. Most of the detailed information regarding the seismic discontinuity structure of open ocean mantle comes from bottom-side reflections that are precursors to SS (An et al., 2007; Deuss and Woodhouse, 2002; Deuss and Woodhouse, 2001; Flanagan and Shearer, 1998; Shearer, 1996; Gu and Dziewonski, 2002; Gu et al., 1998; Gossler and Kind,

1996; Deuss and Woodhouse, 2004; Schmerr and Garnero, 2006) and PP (e.g., Deuss et al., 2006; Flanagan and Shearer, 1999; Chambers et al., 2005; Shearer, 1991). SS and PP precursors offer extensive geographic coverage, especially in the Pacific hemisphere, good sensitivity to small velocity contrasts and reasonable localization (Helffrich, 2000). They do not perform well for shallow reflectors, such as G, or reflectors near the larger transition zone discontinuities, such as X near the bottom of its depth range or low-velocity layers atop the 410-km discontinuity (e.g., Revenaugh and Sipkin, 1994; Nolet and Zielhuis, 1994; Pino and Helmberger, 1997; Song et al., 2004; Gao et al., 2006; Obayashi et al., 2006; Courtier and Revenaugh, 2007; Jasbinsek and Dueker, 2007). For these features the multiple ScS method of Revenaugh and Jordan (1989, 1991abc) remains preferable.

Revenaugh and Jordan (1991c) document an extensive study of the Southwest Pacific Ocean cataloging and modeling observations of upper mantle and transition zone reflectors, leading to the G, L and X designations. With the exception of one corridor connecting earthquakes in the Tonga subduction zone with seismic station KIP in Hawaii, they did not examine any predominately open ocean paths (see also Katzman et al., 1998; Gaherty et al., 1996; Gaherty et al., 1999). Since the publication of that paper, the volume of data appropriate for multiple ScS work has swelled by an order of magnitude and it is now possible to apply the multiple ScS method extensively throughout the Pacific. This paper uses over 30 years of long-period and broadband digital records from the Hawaiian Islands to study eight open ocean paths crossing the Pacific. Our focus is primarily on structure that is hard to detect with SS precursors, but the results encompass the entire mantle.

## 2.2 Data

We collected all available long-period and broadband data from seismic stations on and near the Hawaiian Islands for events within 70°, depths greater than 75 km and magnitudes ($M_b$) of 5.6 and larger. We culled out traces with low multiple ScS signal to noise ratio and apparent source complexity, and in the process eliminated all data from temporary deployments. Remaining seismograms were deconvolved to ground velocity, rotated to transverse and radial components, band-pass filtered between 10 and 60 mHz with corner frequencies at 14 and 40 mHz, and decimated to a three-second sampling interval. The final dataset includes 127 event-receiver

pairs recorded between 1973 and 2005, with depths (z) of $81 < z < 626$ km, and magnitudes $> 5.7$ (Table S1). These were separated into eight event regions based on geographic and tectonic sampling (Figure 1). Each event region samples a swath of the Pacific narrowing toward Hawaii and containing between 5 and 40 seismograms; a representative seismogram is shown in Figure 2.

## 2.3 Methods

Mantle discontinuity depths and shear-wave impedance contrasts were calculated using the hierarchical waveform inversion/migration method of Revenaugh and Jordan (1989, 1991ab). The only change to the method was to specify the source-time function as a rectangular pulse with the half-duration of the event as reported in the global Centroid Moment Tensor (CMT) catalog (e.g., Dziewonski and Anderson (1981)). Because CMT event durations are assigned based on event magnitude, rather than modeled on an event-by-event basis, we visually verified their consistency with reverberation data for each record and adjusted them manually when necessary. Zeroth-order ScS reverberations, i.e., multiple ScS and sScS phases, are used to characterize mean mantle properties such as whole-mantle travel time and attenuation, but also to constrain a simple, one-layer, crustal structure appropriate for each path. First-order reverberations, i.e., those reflected once from a discontinuity within the mantle, are used to detect and characterize mantle reflectors. We do this by first removing from data a synthetic prediction of the zeroth-order reverberations, leaving a residual signal consisting of first- and higher-order reverberations from discontinuities throughout the mantle and noise (both ambient and signal generated) (Revenaugh and Jordan, 1991ab).

One-dimensional migration of the first-order reverberations leads to profiles of shear reflectivity versus depth for the mantle. The general velocity model of Revenaugh and Jordan (1991a) used in the migration was scaled to match the ScS travel time for each source-receiver corridor. Migration proceeds trace by trace and uses both top and bottom-side reflections whose interactions with the reflector are strung out along the great circle path. Synthetic seismograms modeling the first-order reverberation response from a unit-reflectance mantle discontinuity are cross-correlated with data. The results are stacked in the frequency domain with weighting by signal-to-noise ratio. By moving the target discontinuity through the mantle, the method

produces a 1D depth migrated estimate of normal-incidence shear-wave reflectivity. We use both top and bottom-side reflections, which differ in polarity. To avoid confusion in the discussion of reflection coefficients and for consistency with SS precursor studies, we use the sign of the bottom-side reflection which is positive for an impedance increase with depth. Note that the percent change in impedance is twice the reflection coefficient. Synthetic seismograms are also migrated, leading to a synthetic reflectivity profile that is compared to the data to interpret the locations of discontinuities within the mantle. The models are calculated in a series of iterations so that the preferred model contains the minimum number of discontinuities necessary to accurately match the data. Discontinuities were included for peaks that did not exceed the 95% confidence level (estimated by bootstrap iteration on synthetic seismograms matching the time-evolutive power spectrum of data but without phase coherence) if similar features were seen in nearby source-receiver corridors and if inclusion of the discontinuity in the synthetic substantially improved the fit to the data both in the immediate depth-range of the discontinuity and elsewhere through the influence of second and higher-order reverberations. The method is most sensitive to near radial discontinuities. Because of the frequencies and phase velocities of the arrivals we use, extended velocity transitions are well resolved. Only transitions spread over more than 15 km suffer significant downward bias in estimated reflection coefficient.

## 2.4 Results

Data and synthetic SH-reflectivity profiles for each of the eight paths are shown in Figure 3. Depths and estimated reflection coefficients for all modeled reflectors are included in Table 1. Depths are stated relative to 25-second PREM and include adjustments for crustal structure, bathymetry and mantle heterogeneity following the scheme established in Revenaugh and Jordan (1991b). Because they depend on two-way travel time our depth estimates are well constrained with an estimated standard error of 5 to 7 km for the stronger reflectors.

The transition zone discontinuities near 410 and 660 km depth are common to all eight paths. The former has an average depth of 423 km, 5 km greater than the global mean (Flanagan and Shearer, 1998). The latter has a mean depth of 661 km, and is indistinguishable from the global mean (660 km). Differencing the depths

of the two isolates structure in the transition zone (Revenaugh and Jordan, 1991a; Flanagan and Shearer, 1998). The average transition zone thickness of our paths is 238 km, which is within uncertainty of the global mean value of 242 km (Flanagan and Shearer, 1998; Lawrence and Shearer, 2006). Our results support SS precursor observations of a ∼5 to 10 km thinning of the transition zone in the central Pacific rimmed by values roughly 5 to 10 km greater than average along the circum-Pacific (Flanagan and Shearer, 1998; Gu et al., 1998).

G is detected in all of the paths except path 5, and appears split in path 8, perhaps marking an approximately bi-modal depth distribution along that path. It is characterized by a ∼5% negative reflection coefficient (shear-wave impedance decrease of 10%) at an average depth of ∼90 km. The result for path 6 differs from that published in Revenaugh and Jordan (1991c), which placed the reflector at 59 km depth. Given the magnitude of the discrepancy, we reprocessed the nine records used by Revenaugh and Jordan, obtaining a depth for G consistent with the results of path 6. We believe the origin of the discrepancy lies in the instrument response used by Revenaugh and Jordan which was hand-derived and significantly different from that provided the Incorporated Research Institutions for Seismology (IRIS). Use of an inaccurate response likely resulted in incomplete stripping of multiple ScS phases. The remaining energy was then miscast as G by the migration algorithm. The present result agrees with that of path 7 sampling oceanic lithosphere of roughly the same age. Additionally, the match between data and synthetic profiles is excellent and the result of this study is based on considerably more data (40 and 16 seismograms in paths 6 and 7, respectively, versus 9 seismograms in Revenaugh and Jordan (1991c) corridor C8). All other aspects of reflectivity profiles 6 and C8 (e.g., depth and reflection coefficient of the transition zone discontinuities) are similar.

Paths 1, 2, and 3 all show clear evidence of the X discontinuity at similar depths (299–332 km). Path 5 contains a discontinuity at 274 km with a relatively strong impedance contrast. This could be interpreted as a shallow X discontinuity or a deep L discontinuity (recall that this designation is based on depth and sign of the reflector and is not a causative association). Figure 4 shows all of our observations of L and X overlaid with data from the global study using SS precursors by Deuss and Woodhouse (2002). Comparison of the two data sets is made difficult by the vastly different geometry of sampling, namely our quasi-great-circle-path averages versus

spherical cap averages of the Deuss and Woodhouse study. Nonetheless, there is general agreement with respect to sightings of the X discontinuity.

Three of the paths in the southwest Pacific (6, 7, and 8) contain convincing evidence of the 520-km discontinuity. If it is present along other paths, it must be faint ($\leq$ 1.5% reflection coefficient), split, as has been observed elsewhere (e.g., Bagley et al., In Review; Deuss and Woodhouse, 2001; van der Meijde et al., 2005) or sufficiently variable in depth as to destructively interfere in a 1D stack. Constraining the amount of topography needed to occult a reflector similar in amplitude to those observed along paths 6, 7 and 8 is difficult as each path presents different specifics of sampling and different side-lobe structures of the 410-km and 660-km discontinuities. Assuming, however, that topography is normally distributed along the path, a standard deviation of 15 km would reduce the apparent reflection coefficient by a factor of 2 which would be sufficient to drive a weak 520-km reflector below the noise level.

## 2.5 Discussion and Conclusions

*The G Discontinuity:*

A low-velocity zone underlying the seismic lid has been recognized since Gutenberg (1959). It is usually more pronounced under oceans, especially beneath young oceanic lithosphere. Explanations for the low velocities range from the existence of a small partial melt fraction (Anderson and Sammis, 1970; Ringwood, 1975; Revenaugh and Jordan, 1991c), to bound water (Karato and Jung, 1998). It has recently been shown, however, that temperature and grain size effects alone are sufficient (Stixrude and Lithgow-Bertelloni, 2005; Faul and Jackson, 2005) and there is no need to invoke unusual composition or state. What is not explained, however, is the presence of a seismically sharp upper boundary, i.e., the lid-low velocity zone transition. Revenaugh and Jordan (1991c) associated this transition with the G reflector, an abrupt decrease in shear-wave impedance of roughly 8–10% occurring at depths ranging from 50 to 95 km depth. G is observed here in all but one path. These observations add greatly to the catalog of Revenaugh and Jordan (1991c) which was dominated by paths traversing subduction zone complexes.

Because our results do not constrain absolute velocities, we are limited in our ability to comment on the origins of G and the underlying low-velocity zone. Here we focus on the sharpness of the G reflector and the impedance decrease across it.

Modeled as a first-order discontinuity, our observations require impedance decreases between 4.7 and 14.2%. Assuming no density contrast across the transition, the requisite velocity drop equals the impedance drop. This estimate is conservative, as it is highly unlikely that density would decrease with depth through the transition. Our data do not, however, require the change in impedance to be sharp and can easily tolerate an extended transition of 10 to 15 km with little change in the estimated impedance contrast. To extend the transition further requires a greater net impedance decrease across the interval.

Using path 7 as an example, we have computed synthetic reflectivity profiles for transition intervals up to 80 km. For the purposes of modeling, the transition is modeled as a sequence of small steps spaced closely enough to accurately approximate a continuous linear gradient in impedance. The depth ranges and net impedance decrease of the transition were tuned to match data. A 50-km transition interval produces a reflectivity peak that is broader than the data peak but still an acceptable match. By 60 km, the peak is noticeably wider than any of the G reflectors we observe (Figure 5a).

On the basis of width alone, it would appear that transitions up to 50 km are consistent with data. But extended transitions require greater net impedance decreases to match the reflectivity of data and may be too large. To quantify this, we examined a number of models of Pacific upper mantle shear wave velocity obtained for lithospheric ages close to that of path 7 (Lerner-Lam and Jordan, 1987; Nishimura and Forsyth, 1989; Graves and Helmberger, 1988; Gaherty et al., 1999). For each, we computed the maximum velocity drop from the seismic lid to the LVZ. The location of the minimum velocity in these models ranges from 150 to 210 km depth, with lid thicknesses between 60 and 110 km. Maximum velocity decrements range from 6.1 to 9.9%, the largest coming from model PA5 (Gaherty et al., 1999) which used ScS reverberation results to constrain the lid-LVZ transition. Path 7, which has the second smallest G in this study, is close to the PA5 value ($\geq$ 8% versus 9.9%) for a first-order discontinuity. Extending the transition to 30 km increases the net impedance decrease to 9.8%, by 40 km it is 12.6%, by 50 km it is 15.4%, and by 60 km it is 20.8% (Figure 5b). Comparing the reflectivity of G to the maximum velocity drop across the lid-LVZ transition offers a conservative maximum transition interval, as it is unlikely that G alone accounts for the entire velocity drop. We have not considered the effects of downward bias on the apparent reflectivity of G introduced

by along-path velocity and reflector depth centroid heterogeneity and have chosen the path with the one of the smallest G reflections, furthering the conservative nature of these constraints. G appears split in subsets of path 6, the path with the smallest G reflection, suggesting that the low impedance contrast may result from destructive interference. Net impedance contrast imposes the tighter constraint on transition interval with a conservative upper limit of 30 km.

Path 7 traverses oceanic lithosphere with a mean age of ∼100 Ma. Compared with the attenuation-corrected velocity predictions of Stixrude and Lithgow-Bertelloni (2005), our results are best matched by lithospheric ages of 10 to 50 Ma. Other paths in this study also compare best with predictions for substantially (factor of $\geq 2$) younger lithosphere. The age discrepancy persists but is smaller when our results are compared against the predictions of Faul and Jackson (2005). Unlike the Stixrude and Lithgow-Bertelloni (2005) study which assumed a peridotite upper mantle, Faul and Jacksons (2005) predictions are for pure Fo90 olivine and do not consider the remaining $\geq 40\%$ of the upper mantle composition.

*The X Discontinuity:*

Discontinuities between 270 and 330 km have been found by numerous upper mantle studies employing a variety of techniques (e.g., Revenaugh and Jordan, 1991b; Deuss and Woodhouse, 2002, 2004; Zang, et al., 2003; Zhang and Lay, 1993; An et al., 2007). Seismic velocity or impedance increases in this depth range were dubbed X by Revenaugh and Jordan (1991b). They are not detected everywhere, but are widespread, having been found under ocean basins (Bagley et al., In Review; Deuss and Woodhouse, 2002, 2004), beneath continents (Deuss and Woodhouse, 2002, 2004), and near subduction zones (An et al., 2007; Deuss and Woodhouse, 2002, 2004; Revenaugh and Jordan, 1991c; Zang et al., 2003; Zhang and Lay, 1993). The variability in depth and geologic setting suggests that the X discontinuity may have more than one origin.

Several explanations have been put forth for the X discontinuity. Angel et al. (1992) and Woodland (1998) suggest that the orthorhombic to high-pressure monoclinic transition in pyroxene could be the cause of X. In a pyrolite mantle, however, the predicted impedance contrast (0.7%) is too small to account for our observations nor the majority of other documented occurrences of X. High levels of basalt depletion

produce larger contrasts (Matsukage et al., 2005), but basalt depletion has other consequences, namely lowered density and higher seismic velocities (e.g., Jordan, 1979), which do not comport well with tomography of the mid Pacific upper mantle or the geoid (e.g., Forte et al., 1995). Our data provide an independent test of this hypothesis, namely the effect of basalt-depletion on the 410-km discontinuity, which marks the olivine to wadsleyite transition. Basalt-depleted material, i.e., harzburgite contains a higher modal fraction of olivine (80%) than typical mantle peridotite (60%) (e.g., Matsukage et al., 2005). As a result, the 410-km discontinuity in harzburgite will be one-third stronger. As discussed below, the 410-km discontinuity measured along paths with X is, if anything, slightly diminished in reflectivity.

Williams and Revenaugh (2005) show that the coesite to stishovite phase transition in eclogite produces a sufficient increase in impedance to explain the seismic observations of X. This requires an extensive amount of eclogite in the mantle near 300 km along the paths with X. Olivine-poor eclogite crossing into the transition zone would substantially dim the seismic 410-km discontinuity. While the mean reflectance of the 410-km discontinuity is lower for paths with X (3.38%) than those without (3.97%), the t-statistic for the difference of the means is only 0.81 (on six degrees of freedom, the one-tailed 5% significance value of t is 1.94). A similar result holds for the ratio of reflectivity of the 410-km and 660-km discontinuities for paths with and without X (forming the ratio eliminates any overall amplitude bias in the results, e.g., an overall upward bias of reflectivity for all discontinuities along a path). This suggests that if X owes its existence to the presence of eclogitic mantle, little of that eclogite crosses into the transition zone. Given the excess density of eclogite over peridotite in the deep upper mantle and transition zone (Aoki and Takahashi, 2004), it is unclear why eclogite would be effectively segregated above 410 km depth.

Lastly, Ganguly and Frost (2006) determined that the presence of anhydrous phase B could produce a discontinuity in the depth range of X. A subduction geotherm is required to stabilize this phase. While all of our paths originate in subduction zones, the percentage of sampling in subduction-cooled mantle is less than 20% in all cases. Limiting the extent of X to just this portion of the paths would raise the required impedance contrast to greater than 20%, far above that associated with the reaction for reasonable compositions.

Concluding on X, we find no easy explanation of our observations. What is needed

is a ∼5% impedance increase near 300 km depth with little or no effect on the 410-km discontinuity and widespread occurrence throughout the Pacific. One means of accommodating the first two constraints is for X to originate within a melange of eclogite and harzburgite, i.e., something resembling former oceanic lithosphere. With the proper mix, it is possible to produce a strong X and along-path mixture of reflections from the coesite-stishovite transition in eclogite and the orthopyroxene to high-clinopyroxene transition in harzburgite – with little net effect on the reflectivity of the 410-km discontinuity. How slab-like material would come to dominate a large amount of the west-central Pacific upper mantle is a separate question.

*Water:*

Water is introduced into the upper mantle and transition zone via dehydration of subducted oceanic lithosphere (Richard et al., 2007; Ita and Stixrude, 1992). While the velocity decrements associated with reasonable water concentrations in nominally anhydrous silicates are not large, the effects of water on discontinuities can be. Courtier and Revenaugh (2007) used the discontinuity impedance ratio 520:410 along with the presence of a low velocity layer on top of the 410-km discontinuity, to infer a hydrous transition zone. The former responds to water in two ways: (1) through changes in the impedance contrast across the discontinuity and (2) through biases in estimated impedance due to changes in transition interval width. We begin by considering the latter. Below the storage capacity of olivine, water in olivine and wadsleyite leads to broadening of the 410-km discontinuity (Helffrich and Wood, 1996; Chen et al., 2002). The opposite is true of the 520-km discontinuity, which (for the Mg end-member) narrows from 60 km when dry to 15 km under water saturated conditions (Inoue et al., 1998). Reflections from extended transitions suffer from destructive interference, producing smaller reflectivity peaks and lower modeled impedance contrast. A wet upper mantle, with a broadened 410-km discontinuity and a narrowed 520-km, could result in larger estimates of 520:410, if the changes in interval thickness are sufficient. H2O-saturated melting limits the broadening of the 410-km discontinuity (Hirschmann et al., 2006), likely to less than 25 km. For our data, characterized by low frequencies and low radial ray parameter, the ∼45-km maximum narrowing predicted for the wadsleyite-ringwoodite transition is more important and could increase 520:410 by up to 50%. Next we treat the effects of

hydration on the intrinsic impedance contrasts of the 410-km and 520-km discontinuities.

To predict how the 520-km discontinuity will respond to the presence of water requires estimates of the seismic velocities and densities of wadsleyite and ringwoodite as a function of water content, temperature and pressure. These exist for Fe-free wadsleyite (Mao et al., 2008) and ringwoodite (Inoue et al., 1998; Wang et al., 2003), and for Fe-bearing ringwoodite (Jacobsen et al., 2004; Jacobsen and Smyth, 2006). The lack of experimental constraints on Fe-bearing wadsleyite restricts us to considering only Mg end-members. It is also unknown how the partitioning of water between the olivine and pyroxene/garnet components of the transition zone will vary with pressure and temperature. With these caveats firmly in mind, we find that the impedance contrasts across the seismic 520-km discontinuity should increase with increasing water wt%, but the effect is minor in comparison to observed variability in 520:410. Water has a larger effect on the reflectivity of the 410-km discontinuity, driving its reflectivity steeply downward with increasing water wt% (Mao et al., 2008). Assuming a peridotite mantle and incorporating both effects discussed above, we estimate an increase of 40 to 100% in estimated 520:410 between dry and 1.5 wt% hydrated mantle. The ratios presented here for paths with a modeled 520-km discontinuity (0.21 to 0.77) are much lower than those ($\geq 1$) obtained by Courtier and Revenaugh (2007) and presumably indicate drier conditions in the transition zone. A highly broadened 520-km discontinuity due to dry transition zone mantle may also explain our non-observations (paths 1 through 5).

Water also affects transition zone discontinuity depths. The greater storage capacity of wadsleyite over olivine stabilizes the former at lower pressures in hydrous mantle (Wood, 1995; Smyth and Frost, 2002). The converse is true of the 660-km discontinuity, where the very low storage capacities of perovskite and magnesiowustite extend the stability field of ringwoodite to greater pressures (Bolfan-Casanova et al., 2003). In this regard, water mimics low temperatures which cause the transition zone to expand (e.g., Flanagan and Shearer, 1998) and it is difficult to separate the two. Nonetheless, our results are consistent with SS precursor work that shows a thinned transition zone in the central Pacific (Flanagan and Shearer, 1998; Gu et al., 1998), consistent with dry conditions and/or warmer mid-mantle temperatures.

Notably absent from all paths is any indication of a low-velocity layer on top of the 410-km discontinuity, a feature that has been observed in a number of locations (e.g.,

Nolet and Zielhuis, 1994; Pino and Helmberger, 1997; Vinnik and Farra, 2002; Vinnik et al., 2003; Song et al., 2004; Gao et al., 2006; Obayashi et al., 2006; Courtier and Revenaugh, 2007; Jasbinsek and Dueker, 2007; Vinnik and Farra, 2007), including much of the Coral and Tasman Seas and the Sea of Japan. Shear wave velocity reductions of a few percent have led many workers to suggest partial melting within the layer, perhaps related to melting of hydrated transition zone material during passage through the wadsleyite to olivine phase transition (e.g., Bercovici and Karato, 2003). Recent work by Courtier et al. (2007) using methods similar to this study found no evidence of a low-velocity layer directly beneath Hawaii and Oahu. As with the 520-km discontinuity, it is possible for a low velocity layer atop the 410-km discontinuity to escape detection. If it is thin ($\leq$ 15 km), has a low impedance contrast with overlying material or varies considerably in thickness, its signature in 1D reflectivity profiles would be difficult to detect. Ongoing or recent subduction is common to most regions in which the low-velocity layer is observed. The absence of a strong, thick low-velocity layer beneath the central Pacific is consistent with this qualitative trend. Coupled with low 520:410 impedance ratios and a thinned transition zone, it speaks to a drier transition zone in the mid Pacific than along its subduction dominated rim.

## 2.6 References


An, Y., Gu, Y. J., Sacchi, M. D., 2007. Imaging mantle discontinuities using least squares Radon transform. Journal of Geophysical Research-Solid Earth 112 (B10), B10303.

Anderson, D. L., Sammis, C., 1970. Partial melting in the upper mantle, journal=Physics of The Earth and Planetary Interiors 3, 41–50.

Angel, R. J., Chopelas, A., Ross, N. L., 1992. Stability of high-density clinoenstatite at upper-mantle pressures. Nature (London) 358 (6384), 322–324.

Aoki, I., Takahashi, E., 2004. Density of MORB eclogite in the upper mantle; New developments in high-pressure mineral physics and applications to the Earth's interior. Physics of the Earth and Planetary Interiors 143-144, 129–143.

Bagley, B., Courtier, A. M., Revenaugh, J., In Review. Melting in the Deep Upper Mantle Oceanward of the Honshu Slab Submitted to Earth and Planetary Science Letters, February 2008.

Bercovici, D., Karato, S., 2003. Whole-mantle convection and the transition-zone water filter. Nature (London) 425 (6953), 39–44.

Bolfan-Casanova, N., Keppler, H., Rubie, D. C., 2003. Water partitioning at 660 km depth and evidence for very low water solubility in magnesium silicate perovskite. Geophysical Research Letters 30 (17), 4.

Bostock, M. G., 1996. Ps conversions from the upper mantle transition zone beneath the Canadian landmass. Journal of Geophysical Research 101 (B4), 8383–8402.

Chambers, K., Deuss, A., Woodhouse, J. H., 2005. Reflectivity of the 410-km discontinuity from PP and SS precursors. Journal of Geophysical Research 110 (B2), 13.

Chen, J., Inoue, T., Yurimoto, H., Weidner, D. J., 2002. Effect of water on olivine-wadsleyite phase boundary in the (Mg, $Fe)_2SiO_4$ system. Geophysical Research Letters 29 (18), 4.

Chevrot, S., Vinnik, L., Montagner, J.-P., 1999. Global-scale analysis of the mantle Pds phases. Journal of Geophysical Research 104 (B9), 20–20,219.

Courtier, A. M., Bagley, B., Revenaugh, J., 2007. Whole mantle discontinuity structure beneath Hawaii. Geophysical Research Letters 34 (17), L17304.

Courtier, A. M., Revenaugh, J., 2007. Deep upper-mantle melting beneath the Tasman and Coral Seas detected with multiple ScS reverberations. Earth and Planetary Science Letters, 259 (1-2), 66–76.

Deuss, A., Redfern, S. A. T., Chambers, K., Woodhouse, J. H., 2006. The Nature of the 660-Kilometer Discontinuity in Earth's Mantle from Global Seismic Observations of PP Precursors. Science 311 (5758), 198–201.

Deuss, A., Woodhouse, J., 2001. Seismic observations of splitting of the mid-transition zone discontinuity in Earth's mantle. Science 294 (5541), 354–357.

Deuss, A., Woodhouse, J. H., 2002. A systematic search for mantle discontinuities using SS-precursors. Geophysical Research Letters 29 (8), 4.

Deuss, A., Woodhouse, J. H., 2004. The nature of the Lehmann discontinuity from its seismological Clapeyron slopes. Earth and Planetary Science Letters 225 (3-4), 295–304.

Dziewonski, A. M., Anderson, D. L., 1981. Preliminary reference Earth model. Physics of the Earth and Planetary Interiors 25 (4), 297–356.

Faul, U. H., Jackson, I., 2005. The seismological signature of temperature and grain size variations in the upper mantle. Earth and Planetary Science Letters 234 (1-2), 119–134.

Flanagan, M. P., Shearer, P. M., 1998. Global mapping of topography on transition zone velocity discontinuities by stacking SS precursors. Journal of Geophysical Research, B, Solid Earth and Planets 103 (2), 2673–2692.

Flanagan, M. P., Shearer, P. M., 1999. A map of topography on the 410-km discontinuity from PP precursors. Geophysical Research Letters 26 (5), 549–552.

Forte, A. M., Dziewonski, A. M., O'Connell, R. J., 1995. Thermal and chemical heterogeneity in the mantle; a seismic and geodynamic study of continental roots; Structure, composition and evolution of the Earth's interior. Physics of the Earth and Planetary Interiors 92 (1-2), 45–55.

Gaherty, J. B., Jordan, T. H., Gee, L. S., 1996. Seismic structure of the upper mantle in a Central Pacific corridor. Journal of Geophysical Research 101 (B10), 22–22,309.

Gaherty, J. B., Wang, Y., Jordan, T. H., Weidner, D. J., 1999. Testing plausible upper-mantle compositions using fine-scale models of the 410-km discontinuity. Geophysical Research Letters 26 (11), 1641–1644.

Ganguly, J., Frost, D. J., 2006. Stability of anhydrous phase B; experimental studies and implications for phase relations in subducting slab and the X discontinuity in the mantle. Journal of Geophysical Research 111 (B6), 8.

Gao, W., Matzel, E., Grand, S. P., 2006. Upper mantle seismic structure beneath eastern Mexico determined from P and S waveform inversion and its implications. Journal of Geophysical Research 111 (B8).

Gossler, J., Kind, R., 1996. Seismic evidence for very deep roots of continents. Earth and Planetary Science Letters, 138 (1-4), 1–13.

Graves, R. W., Helmberger, D. V., 1988. Upper mantle cross section from Tonga to Newfoundland. Journal of Geophysical Research 93 (B5), 4701–4711.

Gu, Y., Dziewonski, A. M., Agee, C. B., 1998. Global de-correlation of the topography of transition zone discontinuities. Earth and Planetary Science Letters, 157 (1-2), 57–67.

Gu, Y. J., Dziewonski, A. M., 2002. Global variability of transition zone thickness. Journal of Geophysical Research 107 (B7), 17.

Gu, Y. J., Dziewonski, A. M., Ekstrom, G., 2001. Preferential detection of the Lehmann discontinuity beneath continents. Geophysical Research Letters 28 (24), 4655–4658.

Gung, Y., Panning, M., Romanowicz, B., 2003. Global anisotropy and the thickness of continents. Nature (London) 422 (6933), 707–711.

Gutenberg, B., 1959. Wave velocities below the Mohorovicic discontinuity. Geophys.J., London 2 (4), 348–352.

Helffrich, G., 2000. Topography of the transition zone seismic discontinuities. Reviews of Geophysics 38 (1), 141–158.

Helffrich, G. R., Wood, B. J., 1996. 410 km Discontinuity Sharpness and the Form of the Olivine Alpha-Beta Phase Diagram; Resolution of Apparent Seismic Contradictions. Geophysical Journal International 126 (2), F7–F12.

Hirschmann, M. M., Withers, A. C., Aubaud, C., 2006. Petrologic structure of a hydrous 410 km discontinuity; Earth's deep water cycle. Geophysical Monograph 168, 277–287.

Inoue, T., Weidner, D. J., Northrup, P. A., Parise, J. B., 1998. Elastic properties of hydrous ringwoodite (gamma-phase) in $Mg_2SiO_4$. Earth and Planetary Science Letters 160 (1-2), 107–113.

Ita, J., Stixrude, L., 1992. Petrology, elasticity, and composition of the mantle transition zone. Journal of Geophysical Research 97 (B5), 6849–6866.

Jacobsen, S. D., Smyth, J. R., 2006. Effect of water on the sound velocities of ringwoodite in the transition zone; Earth's deep water cycle. Geophysical Monograph 168, 131–145.

Jacobsen, S. D., Smyth, J. R., Spetzler, H., Holl, C. M., Frost, D. J., 2004. Sound velocities and elastic constants of iron-bearing hydrous ringwoodite. Physics of The Earth and Planetary Interiors, 143-144, 47–56.

Jasbinsek, J., Dueker, K., 2007. Ubiquitous low-velocity layer atop the 410-km discontinuity in the northern Rocky Mountains. Geochemistry Geophysics Geosystems 8, Q10004.

Jordan, T. H., 1979. The Deep Structure of the Continents. Scientific American 240, 92–107.

Karato, S., Jung, H., 1998. Water, partial melting and the origin of the seismic low velocity and high attenuation zone in the upper mantle. Earth and Planetary Science Letters 157 (3-4), 193–207.

Katzman, R., Li, Z., Jordan, T. H., 1998. High-resolution, two-dimensional vertical tomography of the Central Pacific mantle using ScS reverberations and frequency-dependent travel times. Journal of Geophysical Research 103 (B8), 17–17,971.

Lawrence, J. F., Shearer, P. M., 2006. A global study of transition zone thickness using receiver functions. Journal of Geophysical Research 111 (B6), 10.

Lerner-Lam, A. L., Jordan, T. H., 1987. How thick are the continents? Journal of Geophysical Research 92 (B13), 14–14,026.

Mao, Z., Jacobsen, S. D., Jiang, F., Smyth, J. R., Holl, C. M., Frost, D. J., Duffy, T. S., 2008. Single-crystal elasticity of wadsleyites, (beta)-$Mg_2SiO_4$, containing 0.37-1.66 wt.% $H_2O$. Earth and Planetary Science Letters 266, 78–89.

Matsukage, K. N., Jing, Z., ichiro Karato, S., 2005. Density of hydrous silicate melt at the conditions of Earth's deep upper mantle. Nature (London) 438 (7067), 488–491.

Nishimura, C. E., Forsyth, D. W., 1989. The anisotropic structure of the upper mantle in the Pacific. Geophysical Journal International 96 (2), 203–229.

Nolet, G., Zielhuis, A., 1994. Low S velocities under the Tornquist-Teisseyre zone; evidence for water injection into the transition zone by subduction. Journal of Geophysical Research 99 (B8), 15–15,820.

Obayashi, M., Sugioka, H., Yoshimitsu, J., Fukao, Y., 2006. High temperature anomalies oceanward of subducting slabs at the 410-km discontinuity. Earth and Planetary Science Letters 243 (1-2), 149–158.

Pino, N. A., Helmberger, D. V., 1997. Upper mantle compressional velocity structure beneath the West Mediterranean Basin. Journal of Geophysical Research, B, Solid Earth and Planets 102 (2), 2953–2967.

Revenaugh, J., Jordan, T. H., 1989. A study of mantle layering beneath the western Pacific. Journal of Geophysical Research 94 (B5), 5787–5813.

Revenaugh, J., Jordan, T. H., 1991a. Mantle layering from ScS reverberations; 1, Waveform inversion of zeroth-order reverberations. Journal of Geophysical Research, B12, Solid Earth and Planets 96 (12), 19,749–19,762.

Revenaugh, J., Jordan, T. H., 1991b. Mantle layering from ScS reverberations; 2, The transition zone. Journal of Geophysical Research, B12, Solid Earth and Planets 96 (12), 19,763–19,780.

Revenaugh, J., Jordan, T. H., 1991c. Mantle layering from ScS reverberations; 3, The upper mantle. Journal of Geophysical Research, B12, Solid Earth and Planets 96 (12), 19,781–19,810.

Revenaugh, J., Sipkin, S. A., 1994. Seismic evidence for silicate melt atop the 410-km mantle discontinuity. Nature (London) 369 (6480), 474–476.

Richard, G., Monnereau, M., Rabinowicz, M., 2007. Slab dehydration and fluid migration at the base of the upper mantle; implications for deep earthquake mechanisms. Geophysical Journal International 168 (3), 1291–1304.

Ringwood, A. E., 1975. Composition and petrology of the Earth's mantle. McGraw-Hill Book Co., New York, N.Y., United States (USA), United States (USA).

Schmerr, N., Garnero, E., 2006. Investigation of upper mantle discontinuity structure beneath the Central Pacific using SS precursors. Journal of Geophysical Research 111 (B8).

Shearer, P. M., 1991. Constraints on upper mantle discontinuities from observations of long-period reflected and converted phases. Journal of Geophysical Research 96 (B11), 18–18,182.

Shearer, P. M., 1996. Transition zone velocity gradients and the 520-km discontinuity. Journal of Geophysical Research 101 (B2), 3053–3066.

Smyth, J. R., Frost, D., 2002. The effect of water on the 410-km discontinuity; an experimental study. Geophysical Research Letters 29 (10), 4.

Song, T. R. A., Helmberger, D. V., Grand, S. P., 2004. Low-velocity zone atop the 410-km seismic discontinuity in the northwestern United States. Nature 427 (6974), 530–533.

Stixrude, L., Lithgow-Bertelloni, C., 2005. Mineralogy and elasticity of the oceanic upper mantle; origin of the low-velocity zone. Journal of Geophysical Research 110 (B3), 16.

Thybo, H., Perchuc, E., 1997. The seismic 8 degrees discontinuity and partial melting in continental mantle. Science 275 (5306), 1626–1629.

van der Meijde, M., van der Lee, S., Giardini, D., 2005. Seismic discontinuities in the Mediterranean mantle. Physics of the Earth and Planetary Interiors 148 (2-4), 233–250.

Vinnik, L., Farra, V., 2002. Subcratonic low-velocity layer and flood basalts. Geophysical Research Letters 29 (4), 4.

Vinnik, L., Farra, V., 2007. Low S velocity atop the 410-km discontinuity and mantle plumes. Earth and Planetary Science Letters 262 (3-4), 398–412.

Vinnik, L., Kumar, M. R., Kind, R., Farra, V., 2003. Super-deep low-velocity layer beneath the Arabian Plate. Geophysical Research Letters 30 (7), 4.

Wang, J., Sinogeikin, S., Inoue, T., Bass, J. D., 2003. Elastic properties of hydrous ringwoodite. American Mineralogist 88 (10), 1608–1611.

Wessel, P., Smith, W. H. F., 1998. New, improved version of the Generic Mapping Tools released. EOS Transactions of the American Geophysical Union 79, 579.

Williams, Q., Revenaugh, J., 2005. Ancient subduction, mantle eclogite, and the 300 km seismic discontinuity. Geology (Boulder) 33 (1), 1–4.

Wood, B. J., 1995. The effect of $H_2O$ on the 410-kilometer seismic discontinuity. Science 268 (5207), 74–76.

Woodland, A. B., 1998. The orthohombic to high-P monoclinic phase transition in Mg-Fe pyroxenes; can it produce a seismic discontinuity? Geophysical Research Letters 25 (8), 1241–1244.

Zang, S., Zhou, Y., Jiang, Z., 2003. Mantle Discontinuities Beneath Izu-Bonin and the Implications. Science in China (Series D) 46 (12), 1201–1211.

Zhang, Z., Lay, T., 1993. Investigation of upper mantle discontinuities near northwestern Pacific subduction zones using precursors to sSH. Journal of Geophysical Research 98 (B3), 4389–4405.

## 2.7 Figures

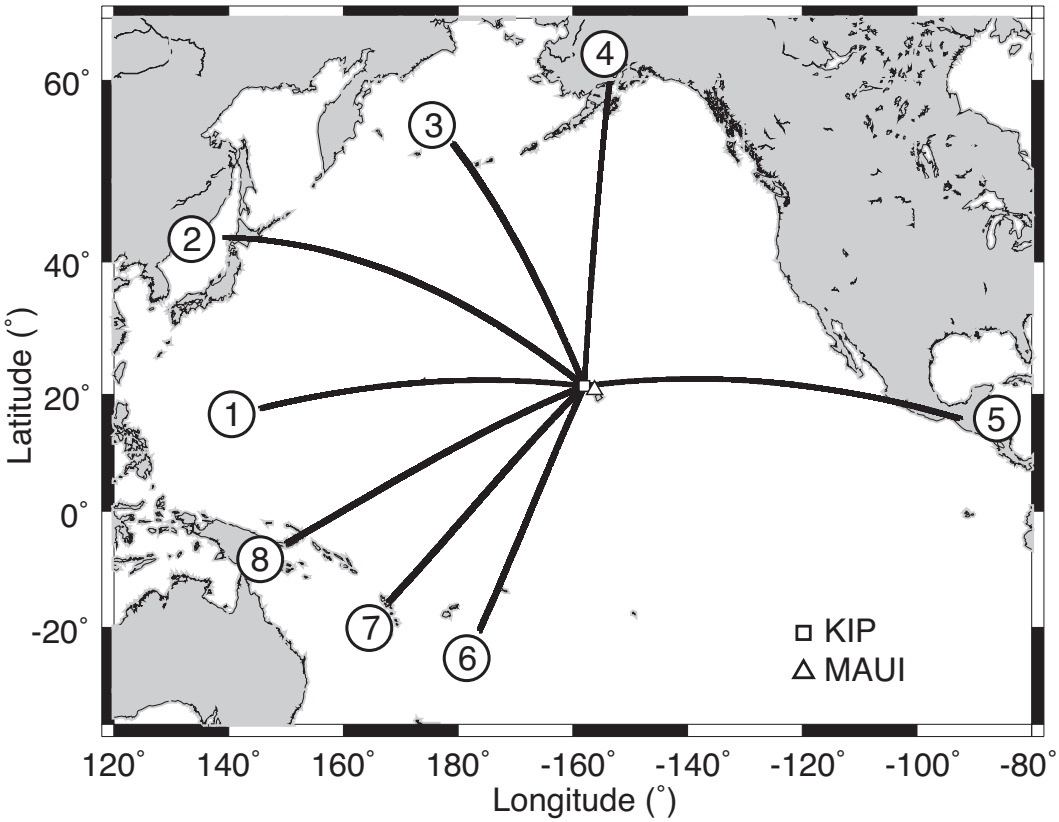


Figure 2.1: Mercator projection showing the 8 source regions (numbers) and receivers KIP and MAUI. Bold lines are the great-circle path for one event in each source region.

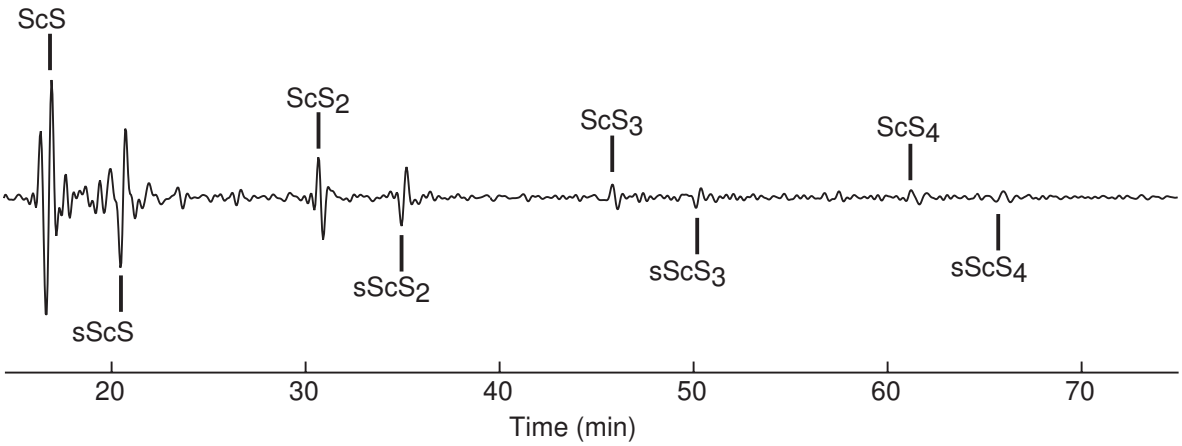


Figure 2.2: Long period, SH-polarized seismogram of the October 17, 2002 earthquake ($M_b$ 6.2, 601 km depth, Lat: -19.67 Lon: -178.60) recorded at station KIP.

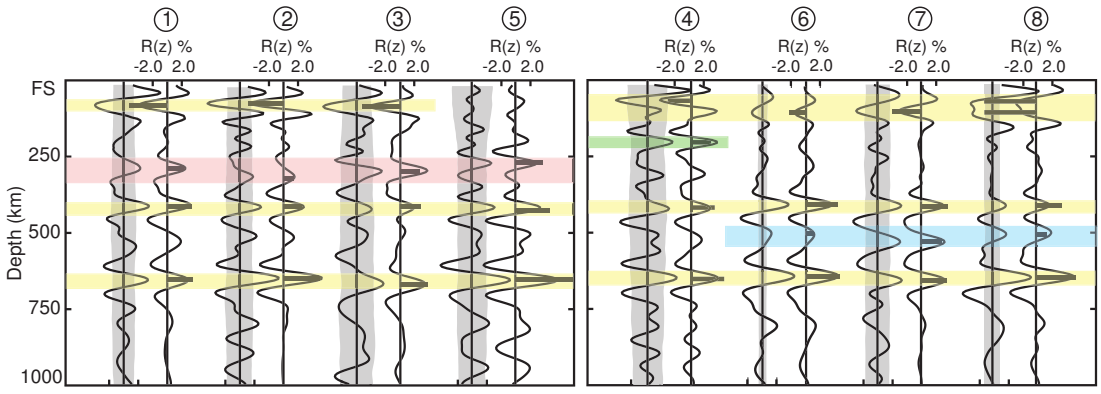


Figure 2.3: Reflectivity profiles for the eight paths in Figure 1. The abscissa is normal-incidence shear-wave reflection coefficient (one half of the fractional shear-wave impedance contrast). For each profile pair, the left-hand profile is data; the right-hand profile is the preferred synthetic profile produced using discontinuities at depths indicated by bold bars whose length is equal to the reflection coefficient. The gray ribbon along the data profile indicates the 95% confidence limit on reflector detection. X is highlighted in red, L in green, and 520 in blue. The remaining discontinuities (410, 660, and G) are highlighted in yellow.

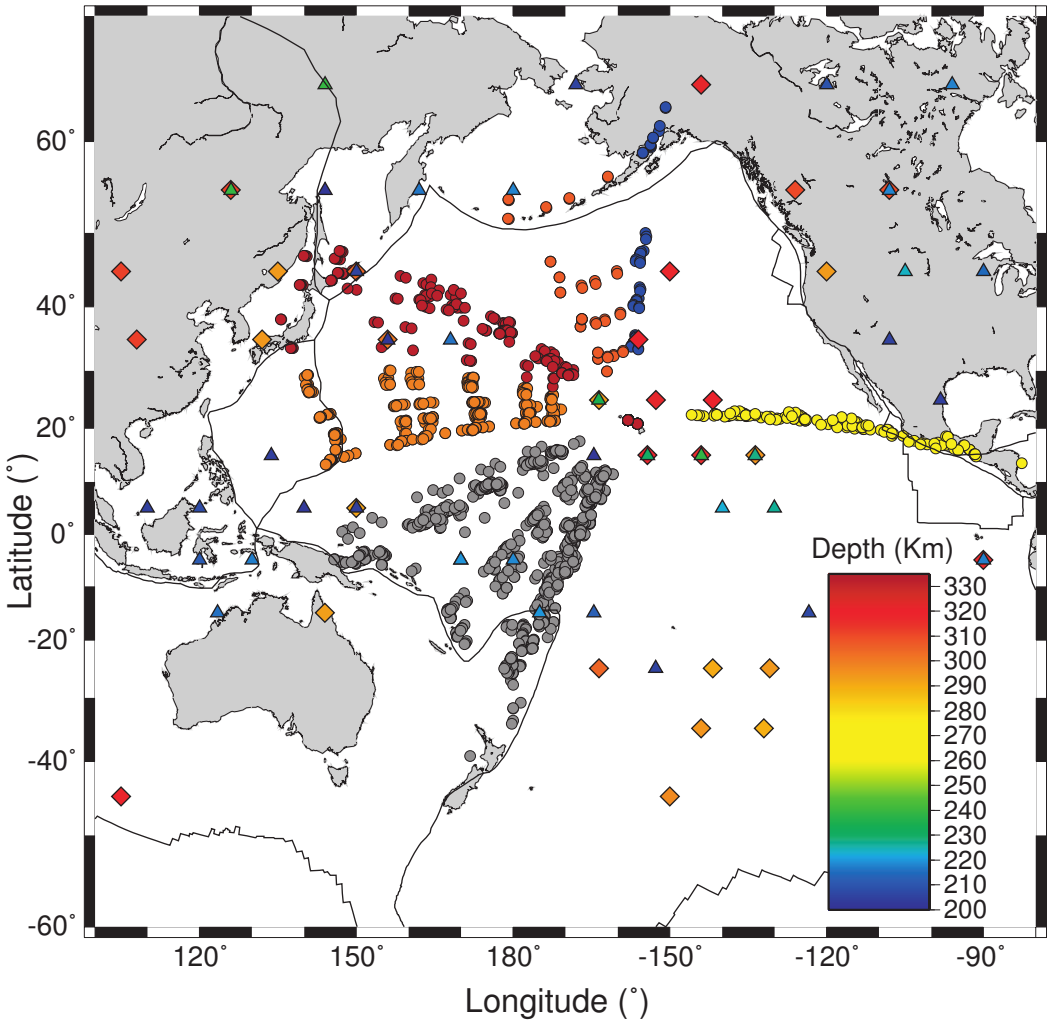


Figure 2.4: Mercator projection showing multiple ScS and sScS bounce points for this study (circles), and locations of the X (diamonds) and L (triangles) discontinuities reported by Deuss and Woodhouse (2002). Colors correspond to discontinuity depth, and grey indicates areas where X and L were not observed.

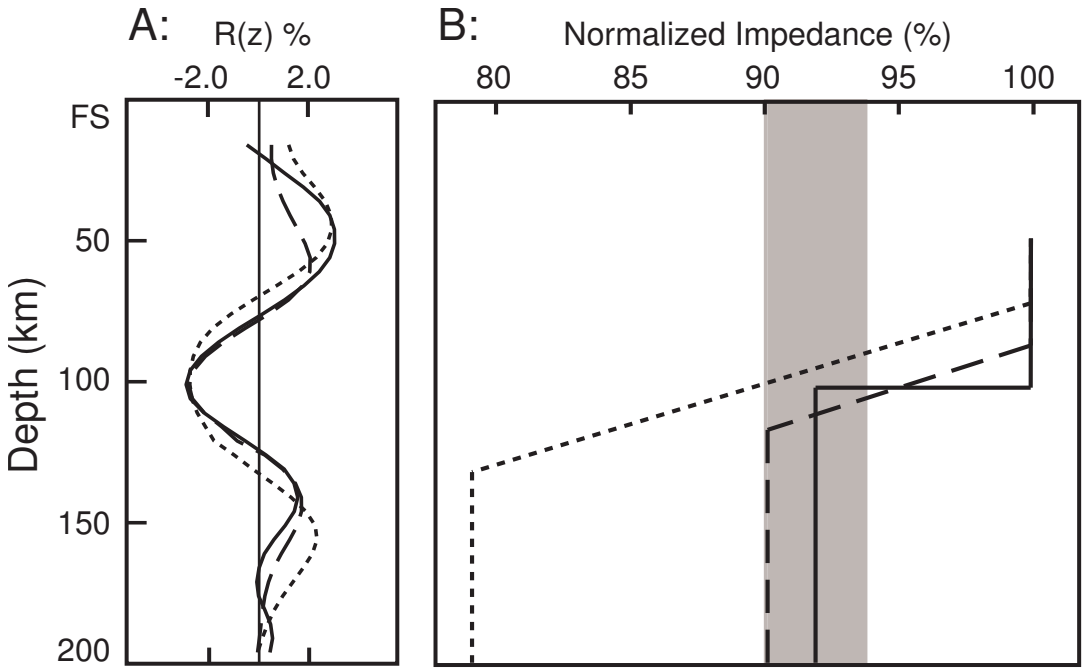


Figure 2.5: A: Comparison of data (solid line) and synthetic reflectivity profiles for the G reflector of path 7. Included are profiles for 30-km (dashed line) and 60-km (dotted line) transition intervals. B: Normalized shear-wave impedance corresponding to a first-order discontinuity (solid line) and transition of 30-km (dashed line) and 60-km (dotted line). The magnitude of the impedance decrease needed to match data increases rapidly with transition interval, reaching -20.8% (reflection coefficient of -10.4%) by 60 km. The 30-km transition interval is the largest to fall within the acceptable impedance contrast range of -6.1 to -9.9% (shaded area).

## 2.8 Tables

Table 2.1: Corrected Discontinuity Depths and Reflection Coefficients for the Eight Seismic Corridors Shown in Figure 1[a].

| | **G** | | **L** | | **X** | | **410** | | **520** | | **660** | |
|---|---|---|---|---|---|---|---|---|---|---|---|---|
| Path | z (km) | R(z) | z (km) | R(z) | z (km) | R(z) | z (km) | R(z) | z (km) | R(z) | z (km) | R(z) |
| 1 | 89 | -4.87 | | | 299 | 1.46 | 426 | 2.54 | | | 666 | 5.03 |
| 2 | 83 | -5.23 | | | 332 | 2.30 | 423 | 3.35 | | | 660 | 3.55 |
| 3 | 91 | -5.30 | | | 307 | 2.66 | 422 | 2.87 | | | 674 | 3.73 |
| 4 | 72 | -4.00 | 208 | 2.76 | | | 423 | 3.26 | | | 655 | 4.55 |
| 5 | | | | | 274 | 3.78 | 432 | 4.77 | | | 659 | 8.10 |
| 6 | 108 | -2.33 | | | | | 414 | 4.44 | 507 | 0.95 | 649 | 4.64 |
| 7 | 107 | -3.98 | | | | | 423 | 3.61 | 540 | 2.76 | 666 | 3.56 |
| 8 | 76 / 112 | -7.13 / -7.11 | | | | | 421 | 3.47 | 517 | 1.51 | 660 | 5.45 |

[a]Reflection coefficients are in units of %.

Table 2.2: (S1) Source parameters of earthquakes used in study. Paths using each event are listed in the last column. Numbers refer to Figure 1.

| **Date** | **Origin Time UTC** | **Latitude Degrees** | **Longitude Degrees** | **Depth (km)** | **Paths** |
|---|---|---|---|---|---|
| February 1, 1973 | 07:27:42 | -17.72 | -175.07 | 220 | 6 |
| July 21, 1973 | 04:19:14 | -24.83 | -179.19 | 419 | 6 |
| December 19, 1973 | 12:55:55 | -20.60 | -176.32 | 229 | 6 |
| December 28, 1973 | 05:31:04 | -23.88 | 180.00 | 526 | 6 |
| March 23, 1974 | 14:28:33 | -23.93 | 179.88 | 514 | 6 |
| June 4, 1974 | 04:14:14 | -15.89 | -175.04 | 275 | 6 |
| October 21, 1974 | 04:12:29 | -17.97 | -178.49 | 596 | 6 |
| September 8, 1974 | 05:17:27 | -3.65 | 153.97 | 420 | 8 |
| February 22, 1975 | 22:04:34 | -24.98 | -178.88 | 373 | 6 |
| November 1, 1975 | 06:14:54 | -18.39 | -177.88 | 423 | 6 |
| November 19, 1975 | 06:18:34 | -24.01 | 179.09 | 548 | 6 |
| December 25, 1975 | 23:22:20 | -4.07 | 142.11 | 106 | 8 |
| January 9, 1976 | 23:54:36 | -15.80 | 167.85 | 171 | 7 |
| February 3, 1976 | 12:27:30 | -25.14 | 179.69 | 477 | 6 |
| March 4, 1976 | 02:50:01 | -14.77 | 167.12 | 100 | 7 |
| January 21, 1977 | 06:11:05 | -18.06 | -178.37 | 602 | 6 |
| March 28, 1977 | 01:15:43 | -14.76 | 167.11 | 116 | 7 |
| July 6, 1977 | 11:28:32 | -21.00 | -178.58 | 585 | 6 |
| May 13, 1978 | 07:08:49 | -14.60 | 167.31 | 170 | 7 |
| July 28, 1978 | 10:46:14 | -18.81 | 169.00 | 209 | 6, 7 |
| August 18, 1978 | 18:52:28 | 59.89 | -153.57 | 133 | 4 |
| August 21, 1989 | 18:25:40 | -4.10 | 154.50 | 480 | 8 |
| September 16, 1989 | 23:20:53 | 16.50 | -93.67 | 108 | 5 |
| May 2, 1990 | 22:50:32 | -5.65 | 150.15 | 86 | 8 |
| June 23, 1990 | 21:38:20 | -21.55 | -176.49 | 186 | 6 |
| July 22, 1990 | 09:26:15 | -23.59 | -179.91 | 530 | 6 |
| July 27, 1990 | 12:38:02 | -15.40 | 167.43 | 131 | 7 |
| August 12, 1990 | 21:25:25 | -19.48 | 169.12 | 163 | 7 |
| December 30, 1990 | 19:14:20 | -5.10 | 150.98 | 191 | 8 |

*Continued on next page*

Table 2.2 – *Continued from previous page.*

| **Date** | **Origin Time UTC** | **Latitude Degrees** | **Longitude Degrees** | **Depth (km)** | **Paths** |
|---|---|---|---|---|---|
| January 23, 1991 | 01:12:29 | 51.96 | 178.81 | 115 | 3 |
| May 1, 1991 | 07:18:42 | 62.58 | -151.54 | 117 | 4 |
| June 9, 1991 | 07:45:02 | -20.25 | -176.22 | 273 | 6 |
| August 14, 1991 | 12:53:25 | 54.35 | -169.36 | 273 | 3 |
| August 15, 1991 | 13:36:02 | -16.10 | 167.97 | 182 | 7 |
| December 3, 1991 | 10:33:40 | -26.46 | 178.70 | 564 | 6 |
| March 13, 1992 | 16:01:04 | 52.42 | -178.98 | 207 | 3 |
| May 12, 1992 | 03:39:30 | 59.84 | -153.67 | 146 | 4 |
| July 11, 1992 | 10:44:21 | -22.28 | -178.51 | 381 | 6 |
| August 16, 1992 | 10:23:31 | -5.42 | 146.68 | 226 | 8 |
| October 11, 1992 | 19:24:27 | -19.26 | 168.91 | 130 | 7 |
| March 1, 1993 | 01:39:28 | -3.74 | 138.54 | 95 | 8 |
| April 24, 1993 | 09:54:21 | -17.87 | 179.85 | 603 | 6 |
| June 3, 1993 | 09:38:26 | -14.92 | 167.31 | 147 | 7 |
| June 15, 1993 | 13:06:34 | -4.98 | 145.48 | 218 | 8 |
| August 7, 1993 | 17:53:25 | -23.93 | 179.85 | 534 | 6 |
| March 14, 1994 | 20:51:25 | 15.99 | -92.43 | 164 | 5 |
| April 10, 1994 | 17:36:57 | 14.72 | -92.00 | 81 | 5 |
| December 27, 1994 | 17:32:51 | -31.97 | 179.86 | 213 | 6 |
| March 31, 1995 | 14:01:41 | 38.15 | 135.06 | 365 | 1 |
| April 8, 1995 | 17:45:13 | 21.83 | 142.69 | 267 | 2 |
| April 13, 1995 | 02:34:37 | -13.52 | 170.49 | 626 | 7 |
| June 24, 1995 | 06:58:08 | -3.96 | 153.91 | 376 | 8 |
| June 29, 1995 | 12:24:03 | -19.49 | 169.27 | 137 | 7 |
| August 14, 1995 | 04:37:21 | -4.90 | 151.50 | 135 | 8 |
| August 23, 1995 | 07:06:03 | 18.86 | 145.22 | 595 | 2 |
| August 24, 1995 | 06:28:55 | 18.85 | 145.12 | 602 | 2 |
| August 24, 1995 | 07:54:43 | 18.82 | 145.04 | 612 | 2 |
| October 9, 1995 | 13:43:44 | -21.43 | 170.12 | 121 | 6, 7 |
| October 20, 1995 | 19:21:29 | 18.71 | 145.54 | 225 | 2 |
| October 21, 1995 | 02:38:57 | 16.84 | -93.47 | 161 | 5 |

*Continued on next page*

Table 2.2 – *Continued from previous page.*

| **Date** | **Origin Time UTC** | **Latitude Degrees** | **Longitude Degrees** | **Depth (km)** | **Paths** |
|---|---|---|---|---|---|
| December 30, 1995 | 02:07:16 | 63.32 | -150.74 | 140 | 4 |
| January 11, 1996 | 03:51:34 | -8.49 | 158.72 | 91 | 7 |
| February 1, 1996 | 07:18:04 | 44.85 | 146.27 | 170 | 1 |
| February 14, 1996 | 21:26:56 | 29.25 | 140.45 | 141 | 2 |
| February 22, 1996 | 14:59:09 | 45.26 | 148.54 | 124 | 1 |
| May 2, 1996 | 13:34:28 | -4.54 | 154.89 | 504 | 8 |
| July 6, 1996 | 21:36:29 | 21.97 | 142.83 | 241 | 2 |
| July 15, 1996 | 16:51:22 | 18.73 | 145.63 | 177 | 2 |
| December 22, 1996 | 14:53:28 | 43.21 | 138.92 | 227 | 1 |
| December 31, 1996 | 12:41:42 | 15.83 | -92.97 | 101 | 5 |
| April 23, 1997 | 19:44:28 | 13.99 | 144.90 | 101 | 2 |
| September 4, 1997 | 04:23:36 | -26.50 | 178.32 | 607 | 6 |
| November 15, 1997 | 07:05:17 | 43.81 | 145.02 | 161 | 1 |
| November 15, 1997 | 18:59:25 | -15.13 | 167.34 | 120 | 7 |
| December 22, 1997 | 02:05:52 | -5.56 | 147.84 | 178 | 8 |
| May 15, 1998 | 05:58:06 | 14.18 | 144.88 | 154 | 2 |
| July 9, 1998 | 19:39:44 | 60.52 | -153.18 | 154 | 4 |
| September 8, 1998 | 09:10:03 | 13.26 | 144.01 | 141 | 2 |
| November 15, 1998 | 02:44:08 | -21.56 | -176.45 | 143 | 6 |
| December 27, 1998 | 00:38:27 | -21.63 | -176.38 | 148 | 6 |
| January 12, 1999 | 02:32:26 | 26.74 | 140.17 | 441 | 2 |
| April 5, 1999 | 11:08:04 | -5.63 | 149.63 | 139 | 8 |
| April 20, 1999 | 19:04:08 | -31.89 | -179.04 | 96 | 6 |
| May 12, 1999 | 17:59:22 | 43.03 | 143.84 | 103 | 1 |
| May 18, 1999 | 04:19:56 | -5.74 | 148.40 | 122 | 8 |
| July 3, 1999 | 05:30:10 | 26.32 | 140.48 | 431 | 2 |
| September 19, 1999 | 03:18:56 | -3.69 | 150.89 | 426 | 8 |
| December 7, 1999 | 21:29:44 | -15.85 | -174.13 | 134 | 6 |
| December 12, 1999 | 17:57:29 | 14.77 | -91.19 | 156 | 5 |
| January 8, 2000 | 16:47:15 | -16.86 | -174.20 | 147 | 6 |
| January 15, 2000 | 12:49:43 | -21.13 | -179.20 | 614 | 6 |

*Continued on next page*

Table 2.2 – *Continued from previous page.*

| **Date** | **Origin Time UTC** | **Latitude Degrees** | **Longitude Degrees** | **Depth (km)** | **Paths** |
|---|---|---|---|---|---|
| January 20, 2000 | 06:13:02 | 56.63 | -161.90 | 224 | 3 |
| February 15, 2000 | 02:05:01 | 17.68 | 145.40 | 522 | 2 |
| March 28, 2000 | 11:00:23 | 22.34 | 143.73 | 127 | 2 |
| May 8, 2000 | 10:28:26 | -4.46 | 150.02 | 493 | 6, 8 |
| June 14, 2000 | 02:15:25 | -25.57 | 177.97 | 595 | 6 |
| June 21, 2000 | 16:25:06 | 14.11 | 144.96 | 112 | 2 |
| July 10, 2000 | 09:58:19 | 46.83 | 145.42 | 360 | 1 |
| August 6, 2000 | 07:27:13 | 28.86 | 139.56 | 395 | 2 |
| October 27, 2000 | 04:21:52 | 26.27 | 140.46 | 388 | 2 |
| December 18, 2000 | 01:19:19 | -21.13 | -179.19 | 621 | 6 |
| December 22, 2000 | 10:13:01 | 44.79 | 147.20 | 140 | 1 |
| January 19, 2001 | 01:12:52 | 15.40 | -92.72 | 94 | 5 |
| February 26, 2001 | 05:58:22 | 46.82 | 144.53 | 392 | 1 |
| July 4, 2001 | 07:06:32 | -21.72 | -176.73 | 180 | 6 |
| July 28, 2001 | 07:32:43 | 59.06 | -155.12 | 145 | 4 |
| October 3, 2001 | 17:25:13 | 47.08 | 148.63 | 285 | 1 |
| November 28, 2001 | 14:32:33 | 15.57 | -93.11 | 85 | 5 |
| January 30, 2002 | 08:42:03 | 18.19 | -95.91 | 111 | 5 |
| June 3, 2002 | 09:15:01 | 27.56 | 139.78 | 489 | 2 |
| October 17, 2002 | 04:23:53 | -19.67 | -178.60 | 601 | 6 |
| November 17, 2002 | 04:53:54 | 47.82 | 146.21 | 459 | 1 |
| January 4, 2003 | 05:15:03 | -20.56 | -177.79 | 376 | 6 |
| March 14, 2003 | 12:54:11 | -17.39 | -175.22 | 271 | 6 |
| June 12, 2003 | 08:59:20 | -5.94 | 154.70 | 177 | 8 |
| July 27, 2003 | 02:04:10 | -21.04 | -176.61 | 205 | 6 |
| July 27, 2003 | 06:25:32 | 47.15 | 139.25 | 470 | 1 |
| August 25, 2003 | 06:28:35 | 14.03 | -91.07 | 98 | 5 |
| November 6, 2003 | 10:38:03 | -19.37 | 168.93 | 110 | 7 |
| November 12, 2003 | 08:26:46 | 33.63 | 137.02 | 391 | 1 |
| January 25, 2004 | 11:43:13 | -16.71 | -174.25 | 139 | 6 |
| March 12, 2004 | 22:13:14 | -15.50 | -175.09 | 275 | 6 |

*Continued on next page*

Table 2.2 – *Continued from previous page.*

| **Date** | **Origin Time UTC** | **Latitude Degrees** | **Longitude Degrees** | **Depth (km)** | **Paths** |
|---|---|---|---|---|---|
| August 7, 2004 | 11:49:13 | 17.20 | -95.22 | 107 | 5 |
| December 28, 2004 | 21:07:35 | 53.29 | -173.82 | 256 | 3 |
| February 2, 2005 | 02:30:26 | 14.08 | 144.72 | 159 | 2 |
| February 5, 2005 | 03:34:26 | 16.01 | 145.87 | 143 | 2 |
| March 17, 2005 | 13:37:37 | 15.14 | -91.38 | 186 | 5 |

# Chapter 3

# Melting in the deep upper mantle oceanward of the Honshu slab

Brian Bagley*[1], Anna M. Courtier[2], and Justin Revenaugh[1]

[1]Department of Geology and Geophysics, University of Minnesota, 310 Pillsbury Drive SE, Minneapolis, MN 55455, USA

[2]Department of Geology and Environmental Science, James Madison University, 800 S. Main Street, MSC 6903, Harrisonburg, VA 22807, USA

This chapter has already been publish and is included with permission from Physics of the Earth and Planetary Interiors. Bagley, B., A. M. Courtier, and J. Revenaugh (2009), Melting in the deep upper mantle oceanward of the Honshu slab, Physics of the Earth and Planetary Interiors, 175(3-4), 137-144, doi:10.1016/j.pepi.2009.03.007.

We examine the upper mantle and transition zone beneath the western Pacific using multiple ScS reverberations. A low velocity zone (LVZ) is found above the 410-km discontinuity oceanward of the subducting Honshu slab at an average depth of 356 km, with a thickness that ranges from 50 km to 75 km assuming the LVZ continues to the 410-km discontinuity, which is locally elevated. The low-velocity region is evident in previous tomographic studies, and our results suggest that the anomaly is best explained by a layer of partial melt. The layer may be entrained from above by subduction or produced in situ by the combined effects of water and temperature. A self-consistent model that explains local P-wave velocities (Obayashi et al., 2006) and our observations calls for a maximum temperature anomaly of $\sim$50 °C and a resulting maximum olivine water content after melting of 0.100 wt. %.

## 3.1 Introduction

Seismic observations of a low velocity zone (LVZ) directly above the mantle transition zone are becoming more frequent with increasingly high-resolution studies of the upper mantle. Revenaugh and Sipkin (1994) made the first observation of a LVZ in the deep upper mantle beneath eastern China and the Sea of Japan using multiple ScS reverberations. They suggested that the LVZ was a layer of negatively buoyant melt resting atop the 410-km discontinuity. Since then, similar explanations have been invoked to account for observations in a variety of geologic settings. Most of these study areas are located above subducting slabs (Revenaugh and Sipkin, 1994; Pino and Helmberger, 1997; Song et al., 2004; Gao et al., 2006; Courtier and Revenaugh, 2007), and the observations are most commonly attributed to regions of water-induced partial melting above the transition zone. Similar observations exist in other geologic settings as well. Most recently, Vinnik and Farra (2007) found a LVZ with an average depth of 350 km at numerous continental locations in Asia, Africa, and Antarctica using S-wave receiver functions. Vinnik and Farra (2002), Vinnik et al. (2003), and Vinnik and Farra (2007) associate the LVZ with areas of continental flood basalts and also relate the feature to a local change in the hydration state of the mantle.

A LVZ oceanward of subduction has been found in many P- and S-wave tomographic studies (e.g., Bijwaard et al., 1998; Fukao et al., 2001; Zhao, 2004; Obayashi et al., 2006). The LVZ oceanward of the Honshu slab imaged by P- and S-wave tomography has been attributed to hot upwelling due to local-scale convection or a rising mantle plume (Zhao, 2004). Obayashi et al. (2006) used triplicated P-waves to establish the first non-tomographic observation of this LVZ. Their P-wave velocity models and waveform analysis indicate that the layer is $\sim$50 km thick and is also associated with a temperature increase of 200 °C. An explanation requiring both increased temperature and either anomalously high iron or water content was put forward by the authors. Their model also requires a velocity decrease near the 410-km discontinuity and a depression of the 410-km discontinuity on the order of 10's of kilometers. The mechanism proposed for producing the melt layer is a hydrous, hot upwelling that melts during phase transformation to olivine, with the resulting melt then entrained toward the subducting slab. In this scenario the Petit-spot (Hirano et al., 2001; Fujiwara et al., 2007) is assumed to be the surface expression of this

activity. The location of this LVZ makes the combined analysis of P-wave tomography, triplicated P-waves (Obayashi et al., 2006), and multiple ScS reverberations (this study) ideal.

Water-induced melting, resulting from the combination of high water content in the transition zone and the lower water storage capacity of minerals in the upper mantle, is usually invoked to explain the presence of a LVZ in the deep upper mantle. The transition zone is a potential reservoir for water due to the enhanced water storage capacity of the transition zone minerals, wadsleyite and ringwoodite, over that of upper and lower mantle mineral assemblages (e.g., Kohlstedt et al., 1996; Hirschmann et al., 2005; Bolfan-Casanova, 2005; Murakami et al., 2002; Bolfan-Casanova et al., 2000). The effects of variations in water content and water storage capacity in the transition zone and overlying upper mantle have been topics of recent debate (Bercovici and Karato, 2003; Hirschmann et al., 2006a; Leahy and Bercovici, 2007). If the water content of material upwelling from the transition zone exceeds the local storage capacity of the overlying upper mantle, melting will occur (Hirschmann et al., 2005). Hirschmann et al. (2006a) suggested that the melt layer would have a maximum thickness of $\sim$7 km, unless the water storage capacity of the upper mantle continued to diminish toward the surface, in which case melt would persist all the way to the surface. The transition zone water filter hypothesis (Bercovici and Karato, 2003; Karato et al., 2006; Leahy and Bercovici, 2007) predicts a laterally extensive, possibly global, melt layer above the 410-km discontinuity varying in thickness from 3 m (Leahy and Bercovici, 2007) to 10 km (Bercovici and Karato, 2003). All of these thickness estimates are at odds with layer thicknesses of the seismic observations of LVZs atop the 410-km discontinuity. Seismic studies generally describe the thickness of the melt layer as the distance from the top of the LVZ to the top of the 410-km discontinuity. S-wave triplication and ScS reverberation methods yield melt layer thicknesses that range from $\sim$20 (Song et al., 2004) to 100 km thick (Revenaugh and Sipkin, 1994).

Possible mechanisms for producing a layer of partial melt thicker than that predicted by petrologic and geodynamic studies are discussed in Courtier and Revenaugh (2007). If olivine above the transition zone is under-saturated with water, and the storage capacity declines with decreasing depth, then the onset of melting would occur at shallower depths (Courtier and Revenaugh, 2007). The resulting melt may be negatively buoyant (Matsukage et al., 2005; Sakamaki et al., 2006) and would percolate

down toward the 410-km discontinuity, creating a thick LVZ. Additional debate exists regarding the dynamics of the melt layer itself. Due to the flux balance that occurs between diffuse upwelling and localized downwelling in subduction zones, Bercovici and Karato (2003), Karato et al. (2006), and Leahy and Bercovici (2007) predict that negatively buoyant melt would eventually sink or become entrained by slabs and assimilated back into the transition zone. This effectively creates a scenario where water is sequestered in the transition zone, which may be problematic considering the balance required between the exosphere and the Earths internal water budget. If this balance is not maintained, a decrease in eustatic sea level might occur during periods of increased subduction (for a review see Hirschmann, 2006b), although this would presumably be balanced, at least in part, by lower mean oceanic lithosphere age and reduced bathymetry. Honda et al. (2007) also propose a scenario whereby slab entrainment is responsible for the localization of hot material atop the transition zone. In this scenario, anomalously hot material is transported from nearby regions within the shallow upper mantle towards the subduction zone and downward. Further entrainment of the material is kinetically inhibited by the 410-km discontinuity, which causes the melt to pool in the deep upper mantle. This model does not consider the effects of water.

If the seismically observed LVZ above the transition zone is caused by water-induced melting above the 410-km discontinuity, there must be a mechanism to introduce water to the region. Irifune et al. (1998) and Shieh et al. (1998) showed that dense hydrous magnesium silicates (DHMS) present in subducting slabs transition into superhydrous phase B and phase D at transition zone and mid-mantle pressures. These phases and water stored in nominally anhydrous minerals (e.g., Kohlstedt et al., 1996; Katayama and Nakashima, 2003) may introduce water into the transition zone and possibly the deep mantle (in the case of DHMS) within subduction complexes. However, while this provides a source of mantle water on the arc side of the slab, it does not introduce significant amounts of water to the mantle below the subducting plate.

Variability in discontinuity depths can help to discern whether temperature or water is a cause of the anomalous observations above the 410-km discontinuity. Due to the Clapeyron slopes of the olivine components in the upper mantle, high temperatures would cause the 410-km discontinuity to deepen (e.g., Katsura et al., 2004a), while the 660-km discontinuity would occur at a shallower depth (e.g., Katsura et al.,

2003). Water present as hydrogen in point defects in mineral structures affects the transition zone discontinuities as well. The behavior predicted at 410 km depth is attributed to the stabilization of wadsleyite in the presence of water. Wood (1995) and Smyth and Frost (2002) predict that the 410-km discontinuity will broaden and migrate to a shallower depth in response to a hydrous, but undersaturated, transition zone. Chen et al. (2002) predicts that the 410-km discontinuity will sharpen and migrate to a shallower depth if the region is saturated with water. The 660-km discontinuity is also affected by the presence of water and may deepen (Higo et al., 2001). The competing effects of water and temperature on discontinuity structure, as well as the additional presence of carbon, or varying amounts of iron can make the changes in transition zone discontinuity depths difficult to interpret.

We re-examine the region sampled by Obayashi et al. (2006) whose combination of regional P-wave tomography and P-waveform modeling was not able to determine the sharpness of the upper boundary of the LVZ on top of the 410-km discontinuity. Here we use multiple ScS reverberations, SH-polarized shear phases that are reflected off of the core-mantle boundary and discontinuities within the mantle. In addition to being more sensitive to changes in shear strength than compressional waves, multiple ScS reverberations require sharp (less than 15 to 20 km thick) changes in velocity and/or density, making them better suited for distinguishing between diffuse thermal anomalies and partial melt horizons.

## 3.2 Data

We conducted a study of the transition zone and upper mantle beneath the Philippine Sea and the Pacific Ocean (Figure 1a). We collected all archived broadband and long-period seismic records of nearby events with magnitude ($M_b$) $> 5.7$ and hypocentral depths greater than 80 km. These seismograms (e.g., Figure 2) were rotated, deconvolved to ground velocity, and decimated to a three-second sampling interval following Revenaugh and Jordan (1989). A cosine-squared zero-phase bandpass filter was applied; filter parameters are listed in Table 1. Each seismogram was visually inspected, and those with low signal-to-noise ratios or apparent source complexity were discarded from the dataset. We additionally excluded events with source depths between 300 and 450 km in the near-subduction paths to ensure that potential observations of a LVZ above the 410-km discontinuity are not the result of effects of

misinterpreted depth phases.

The resulting dataset includes 45 events that occurred between 1995 and 2005, with depths (z) of $101 < z < 612$ km, and magnitudes of $5.7 < M_b < 7.6$ (Table 2). These data were divided into seven source-receiver paths that contain between 12 and 32 seismograms each. The seismic corridors were selected to discretely sample the arc and oceanward side of the slabs located along the western edge of the Pacific plate with as little geologic overlap as possible, paying close attention the geography of the low-velocity anomaly identified by Obayashi et al. (2006).

## 3.3 Method

We use the inversion/migration method of Revenaugh and Jordan (1991a, 1991b) to extract mantle layering information from zeroth- and first-order multiple ScS reverberations. First order top- and bottom-side $ScS_n$ (n = 1 – 4) reflections from 410 km for paths containing a LVZ above the 410-km discontinuity are shown in Figure 3. The migration folds information from both top- and bottom-side reflections from mantle discontinuities into a 1D depth profile (e.g., Figure 4a) of radial normal-incidence shear-wave reflection coefficient (one half of the shear-wave impedance contrast). It is relatively insensitive to along-path velocity heterogeneity, which imposes a small downward bias in estimated reflection coefficient magnitude.

Synthetic seismograms are computed and migrated in the same manner as the data to produce model profiles. Discontinuities are added to the initially smooth background model to match data profiles. We add as few discontinuities as necessary to obtain an accurate match, relying in part on previous modeling and nearby paths for guidance in selecting reflector ensembles. Occasionally, ghost discontinuities arise from the partial chance correlation of reverberations related to multiple ScS and those from multiple sScS from different discontinuities. These ghost discontinuities can have reflectivity peaks that exceed the 95% confidence level but are well matched in a synthetic model without introducing a discontinuity into the velocity model. Estimated reflector depths are corrected to PREM (Dziewonski and Anderson, 1981) using a waveform inversion derived crustal model, digital bathymetry/topography of the free surface, and 3D velocity variability, following Revenaugh and Jordan (1991b).

## 3.4 Results

Reflectivity profiles for all paths in the study are shown in Figure 4; the corresponding depths and impedance contrasts can be found in Table 1. The Hales discontinuity (see Revenaugh and Jordan (1991c) for discontinuity nomenclature) is found in all of the paths except Paths E, F and G, and depths of the observations range between 52 and 66 km. The Gutenberg discontinuity is found beneath the island of Honshu (Path B) at a depth of 99 km, and in the ocean-crossing paths (F and G) at depths of 83 and 89 km, respectively. The Lehmann discontinuity is found in all three paths originating from the Izu Bonin trench (Paths C, D, and E) and varies in depth between 214 and 239 km. There is evidence of the X discontinuity in both of the ocean-crossing corridors (Paths F and G). All of the paths contain the 410-km and 660-km discontinuities. Paths C and E contain evidence of the 520-km discontinuity, with the discontinuity split in the latter path. Paths B, C, and D are modeled best by additionally placing a LVZ above the 410-km discontinuity, with a thickness ($\delta$) that ranges from 50 km $< \delta <$ 75 km (Figure 4a). In all cases, a discontinuity is modeled in the synthetic only when it is required to match the data profile. The inclusion of the discontinuity in our model indicates that the match between data and synthetic profiles improved upon the addition of the discontinuity. Ghost discontinuities that are matched in the synthetic without the addition of a discontinuity at the depth in the synthetic are not indicative of true mantle structure. To cast aside any doubt concerning whether the LVZs we model are real or ghost features, we have included synthetic profiles with and without the LVZ in Figure 4a. This clearly shows that the addition of the LVZ to the velocity model is required to match the data profiles. Figure 4b is an example of two paths (A and E) that appear to have an LVZ in the data profile. However, modeling this feature is not required to obtain a good match between the data and synthetic profiles, and this feature is therefore considered a ghost discontinuity in these paths. We find no significant depression or uplift of either the 410-km or 660-km discontinuities between paths. We also observe discontinuities in the mid-mantle, which are outside the scope of this paper.

## 3.5 Discussion

Our paths sample the region studied by Obayashi et al. (2006) as closely as allowed by the differing source-receiver geometries required by the two different methods. The

region where Obayashi et al. (2006) observed the LVZ is well sampled by our data and our results are similar to theirs, with the exception of the region directly east of Taiwan. We sample this region in Path E and see no evidence of a LVZ, whereas they report a localized LVZ between the Ryuku and Izu-Bonin trenches. Path E covers a broad geographic area compared to the extent of the anomaly observed by Obayashi et al. (2006), so its absence in our data may be a result of the lateral averaging that occurs along our source-receiver path. Figure 1b shows the geographic location of the three paths (B, C, and D) containing evidence of a LVZ overlaid by contours marking the depth of the slab (Niu et al., 2005). All three paths clearly sample the mantle oceanward of the slab at 410 km depth, although completely avoiding interaction with the slab is not possible. However, arrivals due to the slab (an inclined feature) would not stack coherently across the collection of top- and bottom-side reverberations with varying numbers of core reflections and differing sources. The LVZ we observe must be due to a sub-horizontal feature present above the 410-km discontinuity.

The thickness (delta) of the melt layer we observe is on the same order as that used by Obayashi et al. (2006) in their model. As previously discussed, none of the geodynamic (Bercovici and Karato, 2003; Leahy and Bercovici, 2007; Karato et al., 2006) or petrologic (Hirschmann et. al., 2006a) studies offer a mechanism to explain a melt layer this thick, but these studies assume that the material upwelling from the transition zone is saturated as it passes through the 410-km discontinuity, and melts immediately. If, however, the upwelling material is water-rich but not saturated at 410 km depth, it may not melt until it reaches saturation at shallower depths in the upper mantle (e.g., Courtier and Revenaugh, 2007). If melting occurs near 350 km, the melt will be near the density crossover with ambient mantle rocks (Agee and Walker, 1993; Ohtani et al., 1995). If water content varies, some melts may be buoyant and others dense, helping to explain both the LVZ at depth and the surface volcanism of the overlying Petit-spot (Fujiwara et al., 2007). The resulting melt that remains sequestered in the deep upper mantle may have a zero degree dihedral angle (Cmiral et al., 1998; Yoshino et al., 2007), and the signature of melt in the surrounding mantle may be preserved due to surface tension (Hier-Majumder et al., 2006). This remnant signature of melt could explain the apparent melt thickness observed seismically and may enable seismic detection at lower melt-fractions since thin melt films are highly effective at reducing shear modulus (e.g., Walsh, 1969). The depth of the 410-km discontinuity changes in a predictable manner in response

to changes in temperature and/or water. Trade-offs in the response of the 410-km discontinuity to slab uplift and increased temperature or water content outside the slab exist and make interpretation of discontinuity depths difficult. Warmer temperatures should cause the 410-km discontinuity to deepen, whereas colder temperatures have the opposite effect (Katsura et al., 2004a). Increased water content should cause the 410-km discontinuity to broaden and migrate to shallower depths (Wood, 1995; Helffrich and Wood, 1996; Smyth and Frost, 2002). Although the depth variations we observe between paths are small, the three paths sampling the LVZ have the shallowest 410-km discontinuity depths (Table 1). This limits the temperature excess in the region and suggests the importance of water in creating the partial melt layer. Dry peridotite does not melt until ∼2100 °C at 350 km depth (Zhang and Herzberg, 1994). For an average mantle potential temperature of 1350 °C (e.g., Courtier et al., 2007), the corresponding temperature at 350 km depth is 1445 °C (Katsura et al., 2004b). Under these conditions a temperature anomaly of 655 °C is required to induce melting due solely to temperature. Such a large temperature anomaly is not indicated by tomography (Obayashi et al., 2006) or by our estimates of discontinuity depth, which would be sensitive to a depression of the magnitude predicted by such a temperature anomaly despite horizontal averaging.

Recent high-pressure studies of olivine (Smyth et al., 2006; Litasov et al., 2007) provide a method for estimating water content in the pressure-temperature range of the LVZ we observe. The estimated maximum water content in olivine at 1445 °C in the presence of melt is ∼0.229 wt %. This value is below the water storage capacity of olivine without melt present (∼0.394 wt %; Hirschmann et al., 2005), but well above the normal water content of the average mid-ocean ridge basalt (MORB) (∼0.011 wt %; Workman and Hart, 2005). While the amount of water required to induce melting by hydration alone may be a reasonable water content on the arcside of a subducting slab, a mechanism for obtaining a comparable water content oceanward of the slab has not been suggested to date. Given the extremely high temperature anomaly or increased amount of water needed for melting to occur due to either temperature or water alone, we conclude that if the LVZ we observe is the result of in-situ melting, it must be induced by the combined effects of temperature and water.

Obayashi et al. (2006) estimated a 200–250 °C temperature anomaly in the region based on P-wave velocity anomalies from 350 km to the top of the 410-km discontinuity. Under their hypothesis as well as ours, this is a region of partial melt, making

it difficult to separate the velocity decrement due to temperature alone. The P-wave velocity anomalies they observe above the transition zone, as well as the depths and reflection coefficients for the LVZ in our preferred models are influenced by temperature and melt, and so P-wave velocity anomalies occurring below the 410-km discontinuity, where there is likely no melt, provide a better proxy for temperature. Regional tomography (Obayashi et al., 2006) shows a maximum P-wave velocity anomaly of -0.6% near 500 km depth. This depth was chosen to reduce any effect of tomographic smearing from the anomaly above the transition zone. We estimate the corresponding temperature anomaly to be 155 °C, using the tomographic velocity anomaly and a value of 0.0039% per °C (Cammarano et al., 2003) to relate velocity deviation with temperature. The values from Cammarano et al. (2003) are based on a 1300 °C geotherm. We use an average mantle potential temperature of 1350 °C, therefore the 155 °C calculated using the 1300 °C geotherm and a P-wave velocity anomaly of -0.6% is an upper bound for the temperature anomaly in the study area. Since tomographic models are often blurred and may indicate velocity anomalies smaller than actual magnitude, we also compute the temperature anomaly associated with a 67% larger anomaly (P-wave velocity decrement of -1.0%) obtaining a temperature anomaly of 255 °C.

We estimate an upper bound for local water content as well. Including the 155 °C anomaly, the mantle potential temperature at 350 km is 1600 °C (Katsura et al., 2004b). Combining the results from Smyth et al. (2006) and Litasov et al. (2007) we estimate the maximum water content in olivine in this region to be 0.100 wt. %. This value is for water content in olivine in the presence of melt and is therefore an estimate of the current water content in olivine, rather than the amount of water in olivine before melting occurred.

The ScS reverberation method is sensitive to sharp density and velocity contrasts; therefore a diffuse thermal anomaly is unlikely to produce a sufficient impedance contrast to cause observable higher-order reflections. In our models, the top of the LVZ is marked by an impedance decrease of -1.0 to -2.0%. Partial melting has a larger effect on S-wave velocities than P-wave velocities, and the ratio dlnVs:dlnVp in the presence of partial melt at depths near 350 km is approximately 2.3:1 (Berryman, 2000). If we assume that density does not change across the top of the LVZ, then the impedance contrast we observe is due solely to changes in velocity. If density does change across the boundary, it would likely increase rather than decrease, making our

calculation a minimum estimate. Obayashi et al. (2006) estimates the total P-wave velocity reduction due to temperature and melt to be 2.2 %. To compare this with our S-wave velocity reduction ∼350 km we need to subtract the P-wave velocity reduction due to temperature, which we take to be 0.6%, the velocity decrement in the presumably melt-free transition zone. Using 1.6 % as the P-wave velocity reduction due solely to melt (Obayashi et al., 2006) we estimate an average dlnVs:dlnVp ratio of 2.0:1 across the three paths (B, C, and D) where the LVZ is located. Estimates for the individual paths vary from 1.3:1  2.5:1. Although there is considerable uncertainty in both the numerator and denominator, the results are at least consistent with predicted velocity ratios. Paths F and G, the two ocean-crossing paths, help to constrain the extent of the melt layer oceanward of Japan. The reflectivity profiles for these paths (Figure 4c) show no evidence of melt above the 410-km discontinuity, indicating that the LVZ we observe is localized near the subduction zone (Figure 1) and does not extend significantly out into the central Pacific.

This interpretation requires hot material upwelling from at least transition zone depths. Mantle material near the subduction zone is normally entrained by the slab and pulled downward. However, the slab under Japan is a flat-lying slab that does not penetrate the 660-km discontinuity (e.g., van der Hilst et al., 1991; Fukao et al., 2001). This slab geometry is indicative of trench migration (Christensen, 1996; Olbertz et al., 1997; Christensen, 2001), which may reduce downward entrainment, perhaps facilitating ascent of a hot upwelling through the transition zone.

Honda et al. (2007) propose that the velocity anomaly atop the 410-km discontinuity in the study area results from the entrainment of hot material originally located at a shallower depth, likely the remains of a former mantle plume. The anomalous material is entrained by the overlying plate and remains entrained as the plate is subducted. In their model, penetration of the 410-km discontinuity by the anomalous material is kinetically inhibited due to its higher temperature. The residence time of the anomaly above the transition zone is on the order of 100 Myr and depends on temperature and viscosity. However, as discussed previously, slab entrainment in the area may be weak due to the stalling of the slab within the transition zone. Additionally, unless melting occurs under water rich conditions, a temperature anomaly equal to that predicted earlier for dry peridotite melting at 350 km depth would have to be present, which is not supported by topography of the 410-km discontinuity. For these reasons, we prefer the mechanism of in-situ melting resulting from the combined

effects of increased temperature and water content.

## 3.6 Conclusions

This region provides a unique source-receiver geometry, allowing analysis of mantle structure at transition zone depths using tomography, P-wave triplications, and ScS reverberations. LVZ anomalies also appear in the deep upper mantle near other subduction zones in tomographic models, indicating these may be a fairly common phenomenon. Using an impedance-sensitive method that requires coherent reflections from discontinuities in the mantle, we detect the same LVZ observed by Obayashi et al. (2006). One scenario they propose attributes the LVZ to a combination of increased temperature and a 50-km thick partial melt layer. Our results confirm that this is indeed a possibility and is more likely than other mechanisms that have been proposed, including increased iron content or purely thermal anomalies. If the LVZ were the result of melting due to either temperature or water alone, unrealistically high temperature or a mechanism for introducing large amounts water into the transition zone oceanward of subduction is required. We favor a simpler solution, attributing the melt layer to the combined effects of water and temperature, and estimate a maximum temperature anomaly of 155 °C and a resulting maximum olivine water content after melting of 0.100 wt. %. In our interpretation, melting occurs at the upper boundary of the LVZ, and some melt may escape upwards feeding Petit-spot volcanism. Additionally, the presence of melt should lower viscosity near the slab. This would result in less material being entrained by subduction and carried into the transition zone.

## 3.7 References


Agee, C. B., Walker, D., 1993. Olivine flotation in mantle melt. Earth and Planetary Science Letters 114 (2-3), 315–324.

Bercovici, D., Karato, S., 2003. Whole-mantle convection and the transition-zone water filter. Nature (London) 425 (6953), 39–44.

Berryman, J. G., 2000. Seismic velocity decrement ratios for regions of partial melt in the lower mantle. Geophysical Research Letters 27 (3), 421–424.

Bijwaard, H., Spakman, W., Engdahl, E. R., 1998. Closing the gap between regional and global travel time tomography. Journal of Geophysical Research 103 (B12), 30–30,078.

Bolfan-Casanova, N., Keppler, H., Rubie, D. C., 2000. Water partitioning between nominally anhydrous minerals in the MgO-$SiO_2$-$H_2O$ system up to 24 GPa; implications for the distribution of water in the Earth's mantle. Earth and Planetary Science Letters 182 (3-4), 209–221.

Bolfan-Casanova, N., Kleppe, A. K., Welch, M. D., Wright, K., 2005. Water in the Earth's mantle; Protons in minerals. Mineralogical Magazine 69 (3), 229–257.

Cammarano, F., Goes, S., Vacher, P., Giardini, D., 2003. Inferring upper-mantle temperatures from seismic velocities. Physics of the Earth and Planetary Interiors 138 (3-4), 197–222.

Chen, J., Inoue, T., Yurimoto, H., Weidner, D. J., 2002. Effect of water on olivine-wadsleyite phase boundary in the (Mg, $Fe)_2SiO_4$ system. Geophysical Research Letters 29 (18), 4.

Christensen, U., 1996. The influence of trench migration on slab penetration into the lower mantle. Earth and Planetary Science Letters 140 (1-4), 27–39.

Christensen, U., 2001. Geodynamic models of deep subduction. Physics of the Earth and Planetary Interiors 127 (1-4), 25–34.

Cmiral, M., Gerald, J. D. F., Faul, U. H., Green, D. H., 1998. A close look at dihedral angles and melt geometry in olivine-basalt aggregates; a TEM study. Contributions to Mineralogy and Petrology 130 (3-4), 336–345.

Courtier, A. M., Bagley, B., Revenaugh, J., 2007. Whole mantle discontinuity structure beneath Hawaii. Geophysical Research Letters 34 (17), L17304.

Courtier, A. M., Revenaugh, J., 2007. Deep upper-mantle melting beneath the Tasman and Coral Seas detected with multiple ScS reverberations. Earth and Planetary Science Letters, 259 (1-2), 66–76.

Dziewonski, A. M., Anderson, D. L., 1981. Preliminary reference Earth model. Physics of the Earth and Planetary Interiors 25 (4), 297–356.

Fujiwara, T., Hirano, N., Abe, N., Takizawa, K., 2007. Subsurface structure of the "petit-spot" volcanoes on the northwestern Pacific Plate. Geophysical Research Letters 34 (13), L13305.

Fukao, Y., Widiyantoro, S., Obayashi, M., 2001. Stagnant slabs in the upper and lower mantle transition region. Reviews of Geophysics 39 (3), 291–323.

Gao, W., Matzel, E., Grand, S. P., 2006. Upper mantle seismic structure beneath eastern Mexico determined from P and S waveform inversion and its implications. Journal of Geophysical Research 111 (B8).

Helffrich, G. R., Wood, B. J., 1996. 410 km Discontinuity Sharpness and the Form of the Olivine Alpha-Beta Phase Diagram; Resolution of Apparent Seismic Contradictions. Geophysical Journal International 126 (2), F7–F12.

Hier-Majumder, S., Ricard, Y., Bercovici, D., 2006. Role of grain boundaries in magma migration and storage. Earth and Planetary Science Letters 248 (3-4), 735–749.

Higo, Y., Inoue, T., Irifune, T., Yurimoto, H., 2001. Effect of water on the spinel-postspinel transformation in $Mg_2SiO_4$. Geophysical Research Letters 28 (18), 3505–3508.

Hirano, N., Kawamura, K., Hattori, M., Saito, K., Ogawa, Y., 2001. A new type of intra-plate volcanism; young alkali-basalts discovered from the subducting Pacific Plate, northern Japan Trench. Geophysical Research Letters 28 (14), 2719–2722.

Hirschmann, M. M., 2006. Water, melting, and the deep Earth $H_2O$ cycle. Annual Review of Earth and Planetary Sciences 34, 629–653.

Hirschmann, M. M., Aubaud, C., Withers, A. C., 2005. Storage capacity of $H_2O$ in nominally anhydrous minerals in the upper mantle. Earth and Planetary Science Letters 236 (1-2), 167–181.

Hirschmann, M. M., Withers, A. C., Aubaud, C., 2006. Petrologic structure of a hydrous 410 km discontinuity; Earth's deep water cycle. Geophysical Monograph 168, 277–287.

Honda, S., Morishige, M., Orihashi, Y., 2007. Sinking hot anomaly trapped at the 410km discontinuity near the Honshu subduction zone, Japan. Earth and Planetary Science Letters, 261 (3-4), 565–577.

Inoue, T., Weidner, D. J., Northrup, P. A., Parise, J. B., 1998. Elastic properties of hydrous ringwoodite (gamma-phase) in $Mg_2SiO_4$. Earth and Planetary Science Letters 160 (1-2), 107–113.

Karato, S., Bercovici, D., Leahy, G., Richard, G., Jing, Z., 2006. The transition-zone water filter model for global material circulation; where do we stand?; Earth's deep water cycle. Geophysical Monograph 168, 289–313.

Katayama, I., Nakashima, S., 2003. Hydroxyl in clinopyroxene from the deep subducted crust; evidence for $H_2O$ transport into the mantle. American Mineralogist 88 (1), 229–234.

Katsura, T., Yamada, H., Nishikawa, O., Song, M., Kubo, A., Shinmei, T., Yokoshi, S., Aizawa, Y., Yoshino, T., Walter, M. J., Ito, E., ichi Funakoshi, K., 2004a. Olivine-wadsleyite transition in the system $(Mg,Fe)_2SiO_4$. Journal of Geophysical Research 109 (B2), 12.

Katsura, T., Yamada, H., Shinmei, T., Kubo, A., Ono, S., Kanzaki, M., Yoneda, A., Walter, M. J., Ito, E., Urakawa, S., Funakoshi, K., Utsumi, W., 2003. Post-spinel transition in $Mg_2SiO_4$ determined by high P-T in situ X-ray diffractometry; Phase transitions and mantle discontinuities. Physics of the Earth and Planetary Interiors 136 (1-2), 11–24.

Katsura, T., Yokoshi, S., Song, M., Kawabe, K., Tsujimura, T., Kubo, A., Ito, E., Tange, Y., Tomioka, N., Saito, K., Nozawa, A., ichi Funakoshi, K., 2004b. Thermal expansion of $Mg_2SiO_4$ ringwoodite at high pressure. Journal of Geophysical Research 109 (B12), 10.

Kohlstedt, D. L., Keppler, H., Rubie, D. C., 1996. Solubility of water in the alpha , beta and gamma phases of $(Mg,Fe)_2SiO_4$. Contributions to Mineralogy and Petrology 123 (4), 345–357.

Leahy, G., Bercovici, D., 2007. On the dynamics of a hydrous melt layer above the transition zone. J. Geophys. Res 112.

Litasov, K., Ohtani, E., Kagi, H., Jacobsen, S., Ghosh, S., 2007. Temperature dependence and mechanism of hydrogen incorporation in olivine at 12.5–14.0 GPa. Geophysical Research Letters 34 (16), L16314.

Matsukage, K. N., Jing, Z., Karato, S., 2005. Density of hydrous silicate melt at the conditions of Earth's deep upper mantle. Nature (London) 438 (7067), 488–491.

Murakami, M., Hirose, K., Yurimoto, H., Nakashima, S., Takafuji, N., 2002. Water in Earth's lower mantle. Science 295 (5561), 1885–1887.

Niu, F., Levander, A., Ham, S., Obayashi, M., 2005. Mapping the subducting Pacific slab beneath southwest Japan with Hi-net receiver functions. Earth and Planetary Science Letters 239 (1-2), 9–17.

Obayashi, M., Sugioka, H., Yoshimitsu, J., Fukao, Y., 2006. High temperature anomalies oceanward of subducting slabs at the 410-km discontinuity. Earth and Planetary Science Letters 243 (1-2), 149–158.

Ohtani, E., Nagata, Y., Suzuki, A., Kato, T., 1995. Melting relations of peridotite and the density crossover in planetary mantles; Chemical evolution of the mantle. Chemical Geology 120 (3-4), 207–221.

Olbertz, D., Wortel, M., Hansen, U., 1997. Trench migration and subduction zone geometry. Geophysical Research Letters 24 (3), 221–224.

Pino, N. A., Helmberger, D. V., 1997. Upper mantle compressional velocity structure beneath the West Mediterranean Basin. Journal of Geophysical Research, B, Solid Earth and Planets 102 (2), 2953–2967.

Revenaugh, J., Jordan, T. H., 1989. A study of mantle layering beneath the western Pacific. Journal of Geophysical Research 94 (B5), 5787–5813.

Revenaugh, J., Jordan, T. H., 1991a. Mantle layering from ScS reverberations; 1, Waveform inversion of zeroth-order reverberations. Journal of Geophysical Research, B12, Solid Earth and Planets 96 (12), 19,749–19,762.

Revenaugh, J., Jordan, T. H., 1991b. Mantle layering from ScS reverberations; 2, The transition zone. Journal of Geophysical Research, B12, Solid Earth and Planets 96 (12), 19,763–19,780.

Revenaugh, J., Jordan, T. H., 1991c. Mantle layering from ScS reverberations; 3, The upper mantle. Journal of Geophysical Research, B12, Solid Earth and Planets 96 (12), 19,781–19,810.

Revenaugh, J., Sipkin, S. A., 1994. Seismic evidence for silicate melt atop the 410-km mantle discontinuity. Nature (London) 369 (6480), 474–476.

Sakamaki, T., Suzuki, A., Ohtani, E., 2006. Stability of hydrous melt at the base of the Earth's upper mantle. Nature 439 (7073), 192–194.

Shieh, S. R., Mao, H.-K., Hemley, R. J., Ming, L. C., 1998. Decomposition of phase D in the lower mantle and the fate of dense hydrous silicates in subducting slabs. Earth and Planetary Science Letters 159 (1-2), 13–23.

Smyth, J., Frost, D., Nestola, F., Holl, C., Bromiley, G., 2006. Olivine hydration in the deep upper mantle: Effects of temperature and silica activity. Geophys. Res. Lett 33, 12–5.

Smyth, J. R., Frost, D., 2002. The effect of water on the 410-km discontinuity; an experimental study. Geophysical Research Letters 29 (10), 4.

Song, T. R. A., Helmberger, D. V., Grand, S. P., 2004. Low-velocity zone atop the 410-km seismic discontinuity in the northwestern United States. Nature 427 (6974), 530–533.

van der Hilst, R. D., Engdahl, R., Spakman, W., Nolet, G., 1991. Tomographic imaging of subducted lithosphere below Northwest Pacific island arcs. Nature (London) 353 (6339), 37–43.

Vinnik, L., Farra, V., 2002. Subcratonic low-velocity layer and flood basalts. Geophysical Research Letters 29 (4), 4.

Vinnik, L., Farra, V., 2007. Low S velocity atop the 410-km discontinuity and mantle plumes. Earth and Planetary Science Letters 262 (3-4), 398–412.

Vinnik, L., Kumar, M. R., Kind, R., Farra, V., 2003. Super-deep low-velocity layer beneath the Arabian Plate. Geophysical Research Letters 30 (7), 4.

Walsh, J., 1969. New analysis of attenuation in partially melted rock. Journal of Geophysical Research 74 (17), 4333–4337.

Wessel, P., Smith, W., 1998. New, improved version of Generic Mapping Tools released: EOS Trans. Amer. Geophys. U 79 (47), 579.

Wood, B. J., 1995. The effect of $H_2O$ on the 410-kilometer seismic discontinuity. Science 268 (5207), 74–76.

Workman, R., Hart, S., 2005. Major and trace element composition of the depleted MORB mantle (DMM). Earth and Planetary Science Letters 231 (1-2), 53–72.

Yoshino, T., Nishihara, Y., Karato, S., 2007. Complete wetting of olivine grain boundaries by a hydrous melt near the mantle transition zone. Earth and Planetary Science Letters, 256 (3-4), 466–472.

Zhang, J., Herzberg, C., 1994. Melting experiments on anhydrous peridotite KLB-1 from 5.0 to 22.5 GPa. Journal of Geophysical Research 99 (B9), 17–17,742.

Zhao, D., 2004. Global tomographic images of mantle plumes and subducting slabs: insight into deep Earth dynamics. Physics of The Earth and Planetary Interiors, 146 (1-2), 3–34.

## 3.8 Figures

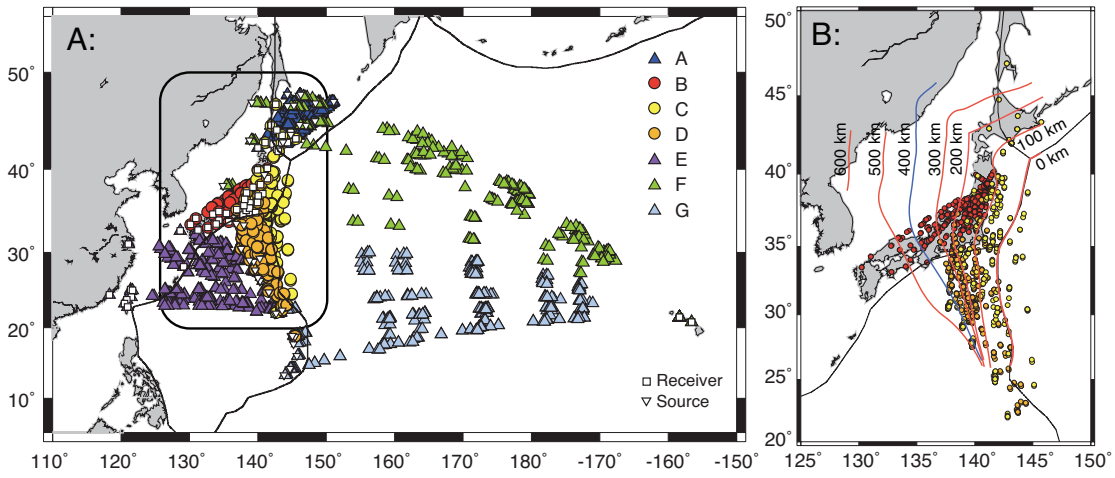


Figure 3.1: A: Multiple ScS surface bounce points for the seven paths in this study. Circles indicate paths where melt was inferred (Paths B, C, and D). Triangles indicate paths were no melt was required (Paths A, E, F, and G). B: ScS surface bounce points for paths B, C, and D with depth contours for the subducting slab (Niu et al., 2005). Source (squares) and receivers (inverted triangles) are also shown; the exact coordinates for the sources can be found in Table 1. Note that all of these paths sample the region oceanward of the slab at depths up to 410 km.

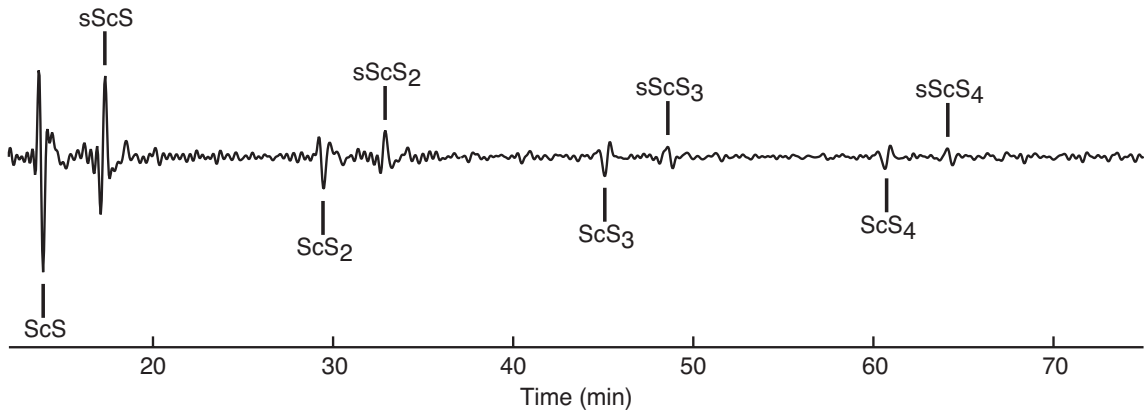


Figure 3.2: Long period, SH-polarized seismogram from the October 3, 2001 earthquake (47.080°N, 148.630°E, 280 km depth) recorded at station URH (42.930°N, 143.671°E) with multiple ScS phases within the reverberative interval labeled. Reflections from the transition zone discontinuities are prominent in the intervals between multiple ScS pairs.

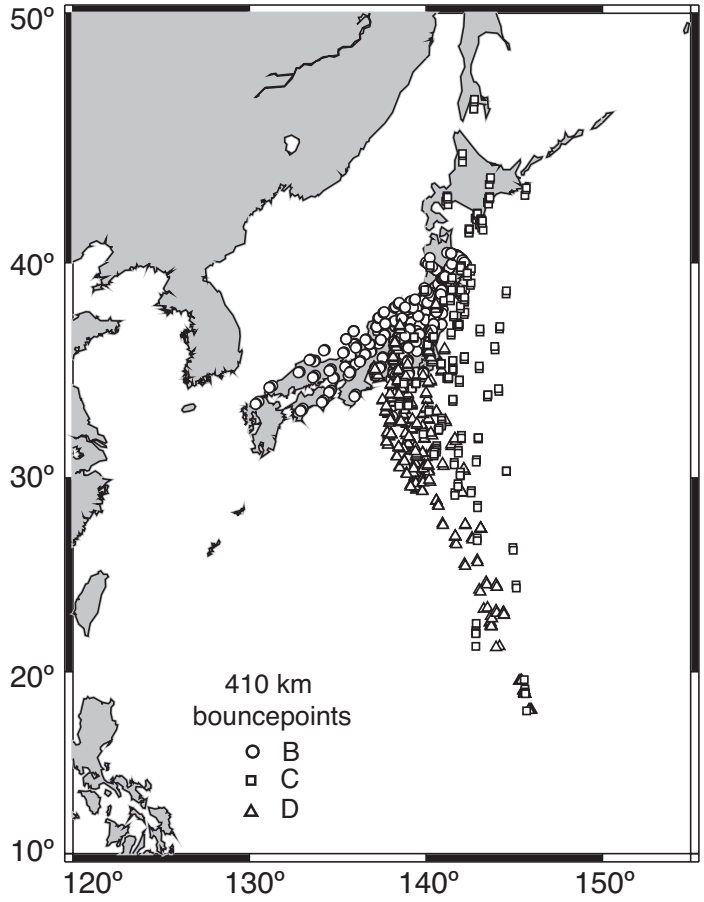


Figure 3.3: First order top- and bottom-side $ScS_n$ (n=1 – 4) reflections from 410 km for paths containing a LVZ above the 410-km discontinuity. Individual paths (B, C, and D) are indicated with a circle, square, and triangle, respectively.

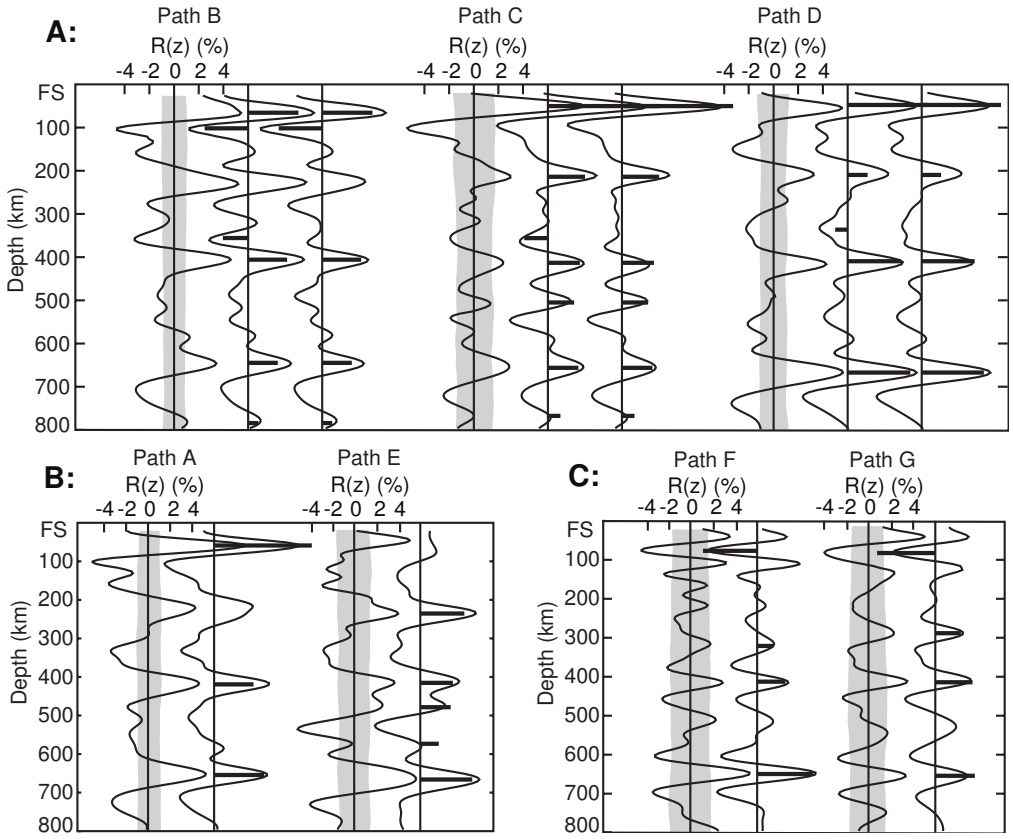


Figure 3.4: SH reflectivity profiles. R(z) (%) with depth from the free surface (FS) to 800 km. The gray bands displayed with data profiles represent the 95% confidence interval for incoherent colored noise. The magnitude of the reflection coefficients listed in Table 1 are shown as horizontal bars. See Figure 1 for path locations and the text for a discussion of peaks exceeding the gray bands that are not modeled with a discontinuity. A: Reflectivity profiles for the three source-receiver paths (B, C, and D) requiring a LVZ atop the transition zone. For each path, data is shown on the left, synthetic data from the preferred model containing the LVZ is shown in the middle, and synthetic data from a model containing no LVZ is shown on the right. B: Data (left) and synthetic (right) reflectivity profiles for the two paths (A and E) adjacent to the paths containing melt. C: Data (left) and synthetic (right) reflectivity profiles for the two ocean-crossing paths (F and G).

## 3.9 Tables

Table 3.1: Discontinuity depths [z (km)] and reflection coefficients [R(z) (%)] from preferred synthetic reflectivity profiles. Bandpass filter parameters provided are low cut, low corner, high corner, and high cut in mHz. TZ = Transition Zone. The errors associated with the LVZ reflection coefficients for paths containing melt were calculated using the jackknife method. See Figure 1 for path locations.

| **Path** | **Filter** | **Hales** | **Gutenberg** | **Lehmann** | **X** | **Melt** | **410** | **Mid TZ** | **660** |
|---|---|---|---|---|---|---|---|---|---|
| | | z, R(z) | z, R(z) | z, R(z) | z, R(z) | z, R(z) | z, R(z) | z, R(z) | z, R(z) |
| A | 8 10 45 60 | 60 8.9 | | | | | 426 3.6 | | 663 4.5 |
| B | 8 10 45 60 | 66 5.4 | | | | 359 -2.0 + 0.8 | 409 3.2 | | 649 2.4 |
| C | 8 10 45 60 | 53 9.0 | | 218 3.0 | | 364 -1.9 + 0.6 | 422 2.6 | 514 2.1 | 667 2.5 |
| D | 8 10 45 60 | 52 6.4 | | 214 1.6 | | 343 -1.0 + 0.9 | 416 4.3 | | 675 5.1 |
| E | 8 10 45 60 | | | 239 4.0 | | | 422 3.0 | 485 2.8 | 674 4.7 |
| | | | | | | | | 581 1.7 | |
| F | 15 17 40 60 | | 83 -5.2 | | 332 2.3 | | 423 3.3 | | 660 5.0 |
| G | 12 14 40 60 | | 89 -4.9 | | 299 1.5 | | 426 2.5 | | 666 3.6 |

Table 3.2: Source parameters for the earthquakes used in study. Paths using each event are listed in the last column. Letters refer to Figure 1.

| **Date** | **Time UTC** | **Lat Deg** | **Lon Deg** | **Depth (km)** | $M_b$ | **Paths** |
|---|---|---|---|---|---|---|
| March 31, 1995 | 14:01:41 | 38.15 | 135.06 | 365 | 6.2 | F |
| April 8, 1995 | 17:45:13 | 21.83 | 142.69 | 267 | 6.7 | G |
| August 23, 1995 | 07:06:03 | 18.86 | 145.22 | 595 | 7.1 | G |
| August 24, 1995 | 06:28:55 | 18.85 | 145.12 | 602 | 5.8 | G |
| August 24, 1995 | 07:54:43 | 18.82 | 145.04 | 612 | 6.1 | G |
| October 20, 1995 | 19:21:29 | 18.71 | 145.54 | 225 | 6.1 | G |
| February 1, 1996 | 07:18:04 | 44.85 | 146.27 | 170 | 6.2 | F |
| February 14, 1996 | 21:26:56 | 29.25 | 140.45 | 141 | 6.0 | G |
| February 22, 1996 | 14:59:09 | 45.26 | 148.54 | 124 | 6.3 | A,F |
| March 16, 1996 | 22:04:06 | 28.98 | 138.94 | 477 | 6.7 | C,D,E |
| June 26, 1996 | 03:22:03 | 27.73 | 139.75 | 468 | 6.3 | C,D |
| July 6, 1996 | 21:36:29 | 21.97 | 142.83 | 241 | 6.2 | C,G |
| July 15, 1996 | 16:51:22 | 18.73 | 145.63 | 176 | 6.3 | C,D,E,G |
| December 22, 1996 | 14:53:28 | 43.21 | 138.92 | 226 | 6.5 | F |
| April 23, 1997 | 19:44:28 | 13.99 | 144.90 | 101 | 6.5 | G |
| November 15, 1997 | 07:05:17 | 43.81 | 145.02 | 161 | 6.1 | A,F |
| February 7, 1998 | 01:13:37 | 24.79 | 141.75 | 525 | 5.9 | C,D |
| February 7, 1998 | 01:19:00 | 24.83 | 141.75 | 525 | 6.4 | C,E |
| February 28, 1998 | 17:38:49 | 33.46 | 138.12 | 291 | 5.7 | B |
| May 15, 1998 | 05:58:06 | 14.18 | 144.88 | 154 | 6.1 | G |
| September 8, 1998 | 09:10:03 | 13.26 | 144.01 | 141 | 6.1 | G |
| January 12, 1999 | 02:32:26 | 26.74 | 140.17 | 440 | 6.0 | G |
| May 12, 1999 | 17:59:22 | 43.03 | 143.84 | 102 | 6.5 | F |
| July 3, 1999 | 05:30:10 | 26.32 | 140.48 | 430 | 6.1 | G |
| February 15, 2000 | 02:05:01 | 17.68 | 145.40 | 522 | 5.9 | G |
| March 28, 2000 | 11:00:23 | 22.34 | 143.73 | 126 | 7.6 | D,E,G |
| June 9, 2000 | 22:35:14 | 30.47 | 137.68 | 472 | 5.8 | C,D |
| June 9, 2000 | 23:31:45 | 30.49 | 137.73 | 485 | 6.3 | C,E |
| June 21, 2000 | 16:25:06 | 14.11 | 144.96 | 112 | 5.9 | G |

*Continued on next page*

Table 3.2 – *Continued from previous page.*

| **Date** | **Time UTC** | **Lat Deg** | **Lon Deg** | **Depth (km)** | $M_b$ | **Paths** |
|---|---|---|---|---|---|---|
| July 10, 2000 | 09:58:19 | 46.83 | 145.42 | 360 | 6.1 | F |
| August 6, 2000 | 07:27:13 | 28.86 | 139.56 | 395 | 7.4 | G |
| October 27, 2000 | 04:21:52 | 26.27 | 140.46 | 388 | 6.3 | G |
| December 22, 2000 | 10:13:01 | 44.79 | 147.20 | 140 | 6.3 | A,F |
| February 26, 2001 | 05:58:22 | 46.82 | 144.53 | 392 | 6.1 | F |
| October 3, 2001 | 17:25:13 | 47.08 | 148.63 | 285 | 5.9 | A,F |
| December 2, 2001 | 13:01:54 | 39.40 | 141.09 | 123 | 6.5 | B |
| June 3, 2002 | 09:15:01 | 27.56 | 139.78 | 488 | 5.9 | C,D,E,G |
| November 17, 2002 | 04:53:54 | 47.82 | 146.21 | 459 | 7.3 | F |
| November 17, 2002 | 04:53:48 | 47.95 | 146.42 | 470 | 5.8 | A |
| July 27, 2003 | 06:25:32 | 47.15 | 139.25 | 470 | 6.8 | A,F |
| November 12, 2003 | 08:26:46 | 33.63 | 137.02 | 391 | 6.4 | F |
| July 8, 2004 | 10:30:49 | 47.20 | 151.30 | 128 | 6.4 | A |
| November 7, 2004 | 02:02:26 | 47.95 | 144.48 | 474 | 6.2 | A |
| February 2, 2005 | 02:30:26 | 14.08 | 144.72 | 159 | 6.3 | G |
| February 5, 2005 | 03:34:26 | 16.01 | 145.87 | 143 | 6.6 | G |

# Chapter 4

# Seismic shear-wave structure of the mantle beneath northeast China and the northwest Pacific

Brian Bagley[1], Anna M. Courtier[2], and Justin Revenaugh[1]

[2]Department of Geology and Geophysics, University of Minnesota, 310 Pillsbury Drive SE, Minneapolis, MN 55455

[2]Department of Geology and Environmental Science, James Madison University, MSC 6903, Harrisonburg, VA 22807

Using multiple ScS reverberations we examine mantle structure beneath northeast China and the northwest Pacific. We find several upper mantle discontinuities including a melt layer with a mean thickness of 64 km atop the 410-km discontinuity, present on both sides of the subducting slab near the Nankai trench. The transition zone contains a split 520-km discontinuity in several paths, and tomographic images show stagnant slabs at this depth. Based on recent experimental work (Saikia, A., Frost, D. J., Rubie, D. C., 2008. Splitting of the 520-kilometer seismic discontinuity and chemical heterogeneity in the mantle. Science 319 (5869), 1515–1518) we believe it may be slab-related. A negative reflector is found in one path beneath the northeast China craton at a depth of 598 km. Mid-mantle reflectors are found in all of our paths and are present throughout a wide depth range (∼750–1600 km).

## 4.1 Introduction

The Boso triple junction, formed by the intersection of the Sagami trough, Izu-Bonin trench, and Japan trench is the only known triple junction between three trenches on Earth. The Japan trench is formed by the subduction of the Pacific plate beneath the North American plate at a rate of ∼8.5 cm/yr (Seno and Takano, 1989; Zang et al., 2002). The oceanic crust being subducted here is relatively old (∼120 Ma) (Müller et al., 2008) and cold, resulting in steeply-dipping subduction (∼30°) (e.g., Yoshii, 1979). Farther to the south, subduction of the Pacific plate at a rate of ∼6.0 cm/yr (Seno and Takano, 1989; Zang et al., 2002) forms the Izu-Bonin trench. Westward subduction of the relatively younger (∼30 Ma) (Müller et al., 2008) Philippine Sea plate beneath the Eurasian plate (∼4.5 cm/yr) forms the Ryukyu trench, and subduction to the north beneath the North American plate (∼2.5 cm/yr) creates the Sagami trough (Seno and Takano, 1989; Zang et al., 2002). Subduction angles for these two regions are markedly different, 40° beneath the Ryukyu trench and 10° beneath the Sagami trough (Katsumata and Sykes, 1969).

Thermal models based on these characteristics predict that the Philippine Sea plate is 300° to 500° warmer beneath southwest Japan, relative to northwest Japan (Peacock and Wang, 1999). This most likely results in slab dehydration at shallow depths and possible slab melting in southwest Japan, whereas volcanism in northwest Japan is thought to originate from melting of the overlying mantle wedge (Morris, 1995; Peacock and Wang, 1999). These predications, based on geochemical analysis and thermal modeling, are supported by seismic tomography of the region (Nakajima and Hasegawa, 2007). Subducting slabs are believed to be an important control on water content in the transition zone and lower mantle (Richard et al., 2007). Slabs that melt at shallow depths, or that do not penetrate the transition zone, are incapable of delivering water to greater depths within the mantle. The complexity of this region gives rise to abundant mantle heterogeneity, and it is reflected in our observations.

The upper mantle is rich with seismic discontinuities that inform our understanding of processes that occur within the mantle. The Hales (H) discontinuity is a velocity increase often observed at depths of ∼40 to 90 km with apparently no preference for continental or oceanic lithosphere (Hales, 1969; Revenaugh and Jordan, 1991c; Levin and Park, 2000; Bagley et al., 2009) (See Revenaugh and Jordan, 1991c for a complete review of upper mantle discontinuities and their nomenclature). The

Gutenberg (G) discontinuity (a decrease in velocity at depths between ∼60 to 120 km) has become synonymous with the Lithosphere-Asthenosphere Boundary (LAB) (e.g., Rychert and Shearer, 2009; Rychert et al., 2010; Fischer et al., 2010). Whether or not the negative discontinuities we find under oceans and continents, at a variety of depths, all have the same origin(s) remains to be proved. Additionally, it is premature to assume that the G discontinuity defines the LAB; it is just as plausible that they arise for separate reasons and are both influenced in a similar way (e.g., temperature and/or water). Velocity increases between ∼150 and 250 km are designated as the Lehmann (L) discontinuity, while velocity increases between ∼270 and 330 km are referred to as X. A low-velocity layer (LVL) above the 410-km discontinuity has been observed in multiple locations (e.g., Revenaugh and Sipkin, 1994; Song et al., 2004; Obayashi et al., 2006; Courtier and Revenaugh, 2007; Vinnik and Farra, 2007; Bagley et al., 2009). Each of these upper mantle discontinuities have been investigated using a variety of seismic methods and multiple explanations for there origin(s) have been proposed, however we do not know for certain what causes any of them.

The upper and mid-mantle are separated by the transition zone, which is bracketed by the 410- (above) and 660-km (below) discontinuities. An additional discontinuity at 520 km is often found and is sometimes observed to be split, occurring at depths of 500 and 560 km (e.g., Deuss and Woodhouse, 2001; Bagley et al., 2009). These discontinuities are due to the phase transition from olivine to wadsleyite (410 km), wadsleyite to ringwoodite (520 km), and the disassociation of ringwoodite to perovskite and ferropericlase (660 km) (see Helffrich (2000) for a review). The 410- and 660-km discontinuities are observed globally (e.g., Flannagan and Shearer, 1998), while the 520-km discontinuity appears as an intermittent feature. The 520-km discontinuity is possibly a global discontinuity, and its absence from some studies could be attributed to poor data quality or conditions in the transition zone (i.e., temperature and/or water) that obscure its detection. The transition zone discontinuities respond in a predictable way to water and temperature, in dry conditions the 520-km discontinuity broadens and migrates to shallower depths (Inoue et al., 1998), which might make it difficult to detect.

Seismic structure in the mid-mantle has been has been detected by many researchers using a wide range of methods (e.g., Revenaugh and Jordan, 1991c; Kawakatsu and Niu, 1994; Niu and Kawakatsu, 1997; Kruger et al., 2001; Deuss and Woodhouse, 2002; Kaneshima and Helffrich, 2003; Gorbatov and Kennett, 2003; Castle and van

der Hilst, 2003; Niu et al., 2003; Revenaugh and Sipkin, 2004; Vanacore et al., 2006; Courtier and Revenaugh, 2008). As these studies demonstrate, mid-mantle reflectors are more commonly found in regions of active or ancient subduction, and this has led many to suggest slab-related explanations for their presence (e.g., Courtier and Revenaugh, 2008; Vanacore et al., 2006; Castle and van der Hilst, 2003; Kruger et al., 2001). Tomographic images of slabs penetrating into the mid- to lower-mantle lend credibility to this assumption (e.g., Fukao et al., 2009; Fukao et al., 2001; Kárason and van der Hilst, 2000). The depth distribution of these reflectors (∼750–1600 km) and their seemingly sporadic occurrence has made it difficult to formulate a reasonable hypothesis explaining their origin(s). Seismically detecting steeply-dipping reflectors, or sub-horizontal reflectors with abundant topography, is problematic for many methods. The obvious questions is: What could cause a subducting slab to stall, and flatten, at mid-mantle depths?

Discontinuities in the mantle arise for a variety of reasons, our ability to detect them is often influenced by the dominant frequency of the phases we choose to analyze, and the preferential instrumentation of continents creates a bias in global studies. The source-receiver geometry of this region makes ScS reverberations well-suited for this study. We have collected 14 years of teleseismic data which allows us to extend our previous (predominately oceanic) study (Bagley et al., 2009) to include the backarc region of Japan, and northeast China. This region, dominated by subduction, is the perfect place to try and learn more about the mantle structure.

## 4.2 Data

We collected all available long-period and broadband data from seismic stations within 60° of the Japanese island arc system. All events had depths greater than 75 km, and magnitudes ($M_b$) of 5.6 and larger. These were culled on the basis of multiple ScS signal to noise ratio and apparent source simplicity, which eliminated all data from temporary deployments. Remaining seismograms were deconvolved to ground velocity, rotated to transverse and radial components, band-pass filtered with a low cut at 8 mHz, a low corner at 10 mHz, a high corner between 45 and 50 mHz, a high cut between 60 and 70 mHz, and decimated to a three-second sampling interval. The final dataset includes 32 events that occurred between 1994 and 2007, with depths (z) of $102 < z < 586$ km, and magnitudes $> 5.7$ (Table 1). In order to investigate

potential mantle variability related to tectonic setting, these data were separated into ten source-receiver paths based on geographic and tectonic sampling (Figure 1). Each path contains between 6 and 32 seismograms; a sample seismogram is shown in Figure 2.

## 4.3 Method

Mantle discontinuity depths and shear-wave impedance contrasts were calculated using the hierarchical waveform inversion method of Revenaugh and Jordan (1989, 1991a, b). The only change to the method was that the source time function was taken to be a rectangular pulse with the half-duration of the event as reported in the global Centroid Moment Tensor (CMT) catalog (e.g., Dziewonski and Anderson, 1981). Because these are assigned based on event magnitude, rather than modeled on an event-by-event basis, we visually verified their consistency with reverberation data for each record and adjusted them manually when necessary. Zeroth-order ScS reverberations, i.e., multiple ScS and sScS phases, are used to characterize mean mantle properties such as whole-mantle travel time and attenuation, but also to constrain a simple, one-layer, crustal structure appropriate for each path. First-order reverberations, i.e., those reflected once from a discontinuity within the mantle, are used to detect and characterize internal mantle reflectors. We do this by first removing from data a synthetic prediction of the zeroth-order reverberations, leaving a residual signal consisting of first- and higher-order reverberations from discontinuities throughout the mantle and noise (both ambient and signal generated) (Revenaugh and Jordan, 1991a, b).

One-dimensional migration of the first-order reverberations leads to profiles of shear reflectivity versus depth for the mantle (Figures 3 and 4). The general velocity model of Revenaugh and Jordan (1991a) used in the migration was scaled to match the ScS travel time for each source-receiver corridor. Migration proceeds trace by trace and uses both top and bottom-side reflections whose interactions with the reflector are strung out along the great circle path. Synthetic seismograms modeling the first-order reverberation response from a unit-reflectance mantle discontinuity are cross-correlated with data. The results are stacked in the frequency domain with weighting by signal-to-noise ratio. By moving the target discontinuity through the

mantle, the method produces a 1D depth migrated estimate of shear-wave reflectivity. Synthetic seismograms are also migrated, leading to a synthetic reflectivity profile that is compared to the data to interpret the locations of discontinuities within the mantle. The models are calculated in a series of iterations so that the preferred model contains the minimum number of discontinuities necessary to accurately match the data. Discontinuities were included for peaks that did not exceed the 95% confidence level (estimated by bootstrap iteration on synthetic seismograms matching the time-evolutive power spectrum of data but without phase coherence) if similar features were seen in adjacent source-receiver corridors and if inclusion of the discontinuity in the synthetic greatly improved the fit to the data. The method is most sensitive to near radial discontinuities. Because of the frequencies and phase velocities of the arrivals we use, extended velocity transitions are well resolved. Only transitions spread over more than 15 km suffer significant downward bias in estimated reflection coefficient.

## 4.4 Results

Reflectivity profiles for paths lacking a LVL are shown in Figure 3, and profiles that require a LVL are shown in Figure 4; the corresponding depths and reflection coefficients for both figures can be found in Table 2. Depths are stated relative to 25-s PREM and include corrections for crustal structure, bathymetry, and mantle heterogeneity following the scheme established by Revenaugh and Jordan (1991b). Because they depend on two-way travel time, our depth estimates are well constrained with an estimated standard error of 5–7 km for the stronger reflectors. Five of the ten paths (6–10) are from a previous study (Bagley et al., 2009), and their synthetic reflectivity profiles have been modified to include mid-mantle discontinuities. Upper mantle structure for these paths has not changed, with the exception of path 8 (path E from Bagley et al., 2009), which includes a H discontinuity in this study. Adding mid-mantle discontinuities to our models causes only minor changes to the depths and reflection coefficients of the upper mantle and transition zone discontinuities.

H is found in all paths except path 5, has a mean depth of 54 km, and a wide range of reflection coefficients (3.9–10.0%). Much of the variability in the reflection coefficients is due to paths 4, 6, and 10 ($> 8.8\%$), which is extremely high for the H discontinuity. The station locations for these paths are all located on Hokkaido,

the northernmost island of Japan. It is possible that something inherent to this geographic location, or the stations, has biased our reflection coefficients. Revenaugh and Sipkin (1994) suggested that reflection coefficients and discontinuity depths may be strongly biased by unmodeled reverberations due to an anomalously thick crust. In our model we used crustal thicknesses of 20 km, 15 km, and 15 km for paths 4, 6, and 10, respectively. Miyamachi et al. (1994) estimated the Mohorovičić discontinuity to be 32 km deep beneath the Hidaka Mountains in southeastern Hokkaido, 20 km beneath the Konsen Plateau, and 30 to 36 km in western Hokkaido and the Tohoku region. In a Vibroseis seismic reflection study Arita et al. (1997) were unable to clearly image the Mohorovičić discontinuity, and suggested that it might be deeper than 50 km beneath the Hidaka Mountains.

G is found in paths 1–3, 5, and 7 and has a wide range of depths (z) $88 > z < 153$ km, and reflection coefficients (R(z)) $-0.7 > R(z) < -6.7\%$. A discontinuity due to an increase in velocity is present in paths 2, 5, and 8–10 at a depth range of 208–285 km. It is common to interpret velocity increases between 150 and 250 km as L, and velocity increases between 270 and 330 km as X (Deuss and Woodhouse, 2002; Revenaugh and Jordan, 1991c; Bagley and Revenaugh, 2008). Based on this criteria we interpret the discontinuity in path 2 as X, and the discontinuities in paths 5, and 8–10 as L. Another plausible interpretation would be that they are all L, the one in path 2 being unusually deep.

A LVL in the deep upper mantle is present in five paths (2, 3, 7, 9, and 10), although it could possibly be omitted in path 3. Reflectivity profiles for these paths (Figure 4) include synthetic traces for two models; one with the LVL (red line) and one without (blue line). It is clear that including the LVL in the model provides a better fit to these data, and that the feature we are modeling is not a side-lobe of the 410-km discontinuity. The discontinuity we model is the top of the LVL, and we assume that the layer extends all the way to the top of the 410-km discontinuity. Based on this assumption the thickness of the LVL ranges from 31 to 76 km, and the mean reflection coefficient is -1.5%. The characteristics of the LVL in path 3 are much different from the other paths containing a LVL. If we exclude path 3, the mean depth is 64 km, and the mean reflection coefficient is -1.7%.

The 410- and 660-km discontinuities are present in all paths, and the mean transition zone thickness is 247 km, which is consistent with the global mean of 242 km

(Flanagan and Shearer, 1998; Lawrence and Shearer, 2006). The 520-km discontinuity is present in six paths (1–3, 5, 8, and 10) and is split in paths 3, 5, and 8. Path 3 contains an additional transition zone discontinuity at 598 km, with a reflection coefficient of -2.5%. The 660-km discontinuities in paths 4 and 5 are depressed 17 and 11 km, respectively, which is notably larger than the depth variation of the 660-km discontinuities in the other paths.

Mid-mantle discontinuities at a wide range of depths are common to all paths. Some of these are small features ($R(z) < 1.0\%$) and do not exceed the 95% confidence level. However, if their addition to our model provided a better match between the synthetic and data profiles they were included. A few paths contained three mid-mantle discontinuities, so we categorized our results in three depth ranges; 750–850 km (M1), 851–1000 km (M2), and 1001–1600 km (M3).

## 4.5 Discussion

*The Gutenberg Discontinuity*

Observations of the G discontinuity in this study range in depth from 88 km to 155 km, and the associated reflection coefficients range from -0.7% to -6.7%. The variability in depth is not surprising, as many workers have had similar results in both local and global studies (discussed below). The extremely low reflection coefficient in path 3 (-0.7%) is somewhat enigmatic, path 3 also contains an H discontinuity with a relatively large reflection coefficient (6.5%). It is conspicuous that the three paths with the largest reflection coefficients for H (paths 4, 6, and 10) lack a G discontinuity. The apparent lack of G in these paths might be due to multiples from the H discontinuity destructively interfering with G, and for path 3 this results in a G diminished in amplitude.

Our depths are in good agreement with other regional studies (e.g., Feng et al, 2010; Chen et al., 2008; Revenaugh and Jordan, 1991c). For the purpose of clarifying this discussion we will assume that the depth of G defines lithospheric thickness since that is how most other studies choose to discuss their findings. Feng et al. (2010) used surface wave tomography to image the North China craton and found a variation in lithospheric thickness from ∼150 km (west) to ∼100 km (east). A S-to-P receiver function study of the northeast North China craton (Chen et al., 2008) reveals a similar result; a lithosphere that thins from west (∼100–130 km) to east (∼60–70 km).

Revenaugh and Sipkin (1994), using ScS phases, reported depths of the G discontinuity that vary from 131–158 km (west) to 80–133 km (northeast). Global studies of LAB thickness (e.g., Rychert et al., 2010; Rychert and Shearer, 2009) suggest that lithospheric thickness might be correlated with tectonic environments. Rychert et al. (2010) provides a comprehensive review of LAB depths, focusing on receiver function studies. They concluded that lithospheric thickness is ∼150–300 km beneath Precambrian shields and ∼40–120 km beneath oceans and Phanerozoic magmatic zones, and our results are consistent with these findings.

*Low-Velocity Layer*

Evidence of a LVL above the transition zone was first reported by Revenaugh and Sipkin (1994), since then many more discoveries in similar geologic environments (i.e., subduction zones) have been made (e.g., Pino and Helmberger, 1997; Song et al., 2004; Gao et al., 2006; Courtier and Revenaugh, 2007). LVLs beneath continents (Vinnik and Farra, 2002; Vinnik et al., 2003; Vinnik and Farra, 2007; Wittlinger and Farra, 2007) and oceanward of subducting slabs (Obayashi et al., 2006; Bagley et al., 2009) have also been found. These LVLs are interpreted as the seismic signature of partial melting in the deep upper mantle and seem to indicate that this phenomenon occurs on a larger scale than we previously thought. Five of our paths that show evidence of melt (paths 2, 3, 7, 9, and 10), albeit path 3 is questionable. Paths 7, 9, and 10 sample the oceanward side of the slab (Figure 5), while paths 1 and 2 predominately sample the backarc side of the slab (see Bagley et al., 2009 for details regarding paths 3, 7, and 9). With the addition of only one new path containing melt we are unable to draw any new conclusions about the generation and/or emplacement of melt in this region.

*Transition Zone Discontinuities*

The transition zone discontinuities are among the most studied discontinuities in the mantle, primarily because they are relatively sharp global features, and are easily detected by most methods. Laboratory experiments have provided us with details of the phase changes that give rise to the transition zone discontinuities, and how these phase changes respond to changes in pressure, temperature, and mineral assemblage. Based on Clapeyron slopes calculated for the 410-km discontinuity, it should migrate to shallower depths as temperature decreases or water content increases and become

less reflective (Akaogi et al., 1989; Bina and Helffrich, 1994; Katsura et al., 2004). The 660-km discontinuity is expected deepen as temperatures decrease or water increases (Katsura et al., 2003). This has led many workers to use transition zone thickness, and the depths of the 410- and 660-km discontinuities, as proxies for temperature and/or water content in the transition zone. Our results do not show a significant increase in transition zone thickness, although the 660-km discontinuity is depressed 17 km in path 4, and 11 km in path 5; the expected observation in subduction zones near the slab. The 410-km discontinuity is also depressed in those paths, 17 km in path 4 and 15 km in path 5, resulting in transition zone thicknesses (250 km, path 4; 246 km, path 5) that are indistinguishable within error from the global mean ($\sim$242 km). Shearer Masters (1992) also observe an anomalously deep 660-km discontinuity near Kamchatka, which varies in depth with a peak-to-peak amplitude of $\sim$30 km. Based on estimates of the Clapeyron slope for the 660-km discontinuity they predict that temperature changes between 300 to 600 K would be required to create this type of topography. Since we observe anomalous depths in only two paths it is difficult to draw conclusions about transition zone conditions from these results.

The discontinuity at 520 km is believed to result from the phase change of wadsleyite to ringwoodite (Katsura and Ito, 1989; Shearer, 1990), and based on the Clapeyron slope for this phase change, the 520-km discontinuity should sharpen and migrate to shallower depths as temperature decreases and/or water content increases (Inoue et al., 1998; Helffrich, 2000). A sharper 520-km discontinuity has been observed in areas of subduction (Courtier and Revenaugh, 2006; Courtier and Revenaugh, 2007), and they concluded that the increase in reflectivity is indicative of water-rich transition zone. In some studies the 520-km discontinuity is split (e.g., Deuss and Woodhouse, 2001; Chambers et al., 2005; Bagley et al., 2009), while other studies show no evidence for splitting (Courtier and Revenaugh, 2006). When split, two discontinuities are observed at depths of approximately 500 and 560 km (Deuss and Woodhouse, 2001), which is consistent with the three paths in this study (paths 2, 5, and 8) that have a split 520-km discontinuity. The reflectivity profiles for these three paths require a split 520-km discontinuity, however in two of the paths (paths 2 and 5), the evidence is far from overwhelming.

An explanation for the presence of two mid-transition zone discontinuities has been elusive. Deuss and Woodhouse (2001) suggested that the discontinuity near 500 km was due to the wadsleyite to ringwoodite phase change, while the deeper

discontinuity near 560 km might be caused by the exsolution of Ca-perovskite from garnet. Ita and Stixrude (1992) had suggested that the exsolution of Ca-perovskite might be responsible for the 520-km discontinuity, and lacking observations of splitting there was no reason to consider a more complicated scenario. Saikia et al. (2008) conducted high-pressure (15–24 Gpa) and high-temperature (1400°C–1600°C) to test the solubility of $CaSiO_3$ perovskite in majorite garnet. They concluded that in fertile peridotite (i.e., peridotite enriched in Ca and Al) at 1400°C the wadsleyite to ringwoodite phase change produces a strong discontinuity at ∼500–520 km, and the exsolution of Ca-perovskite produces a weak discontinuity near 540 km. At 1600°C the two merge and form a single discontinuity at ∼540–560 km. In compositions similar to midocean ridge basalt (MORB) the wadsleyite to ringwoodite phase change does not occur, but exsolution of Ca-perovskite causes a strong discontinuity near 560 km. They concluded that a mantle enriched in MORB would have two discontinuities; a weak discontinuity near 500 km due to the wadsleyite to ringwoodite phase change, and a stronger discontinuity near 560 km due to the exsolution of Ca-perovskite from garnet. However, they could not completely rule out the possibility that temperature variation alone might be responsible for the two discontinuities. In addition to water, temperature, and Ca, the wadsleyite to ringwoodite transition is sensitive to Fe (Hirschmann et al., 2005; Demouchy et al., 2005). With all of these influences to consider care should be taken when inferring transition zone conditions based on changes in the depth and sharpness of the 520-km discontinuity.

Stagnant slabs in the transition zone could provide the Ca enrichment needed for the scenario proposed by Saikia et al. (2008), making subduction zones the obvious place to test their hypothesis. If true, splitting of the 520-km discontinuity should correlate with regions where slab material accumulates in the transition zone. To examine this possibility we will compare the results of several studies and see if the results are consistent with regional and global seismic tomography. Deuss and Woodhouse (2001) and Courtier and Revenaugh (2006) both sample a large portion of North America. At transition zone depths the Farallon slab is clearly visible in the west and southwestern United States (Schmid et al., 2002; van der Lee and Nolet, 1997; Fukao et al., 2009). From the midwest to the eastern United States the Farallon slab is not stagnant at transition zone depths, it is a steeply dipping feature that descends into the lower mantle. Courtier and Revenaugh (2006), using multiple ScS reverberations,found clear evidence for the 520-km discontinuity, however none

of them are split. Using SS precursors, Deuss and Woodhouse (2001) analyzed four stacks of seismic data for the northern United States (their cross section c to C). The 520-km discontinuity is split in the two eastern stacks, missing from one of the western stacks, and not split in the remaining western stack. The results from Courtier and Revenaugh (2006) could be due to the effects of path averaging if there is significant topography along the path, or if the path samples regions where the stagnant slab is present and regions where it is not (e.g., the western paths). A P-to-S receiver function of the northeast United States (Li et al., 1998) also has evidence for a split 520-km discontinuity, although it is tenuous. These results seem to show exactly the opposite from what is expected, i.e. correlation with the region where there is slab accumulation in the transition zone.

The tomography for the area surrounding Japan shows abundant evidence for slabs stalled in the transition zone (e.g., Kárason and van der Hilst, 2000; Fukao et al., 2009, and references therein). Splitting of the 520-km in this region is found in this study (paths 2, 5, and 8) and by Deuss and Woodhouse (2001). Splitting in our study seems to be confined to paths that are perpendicular to trenches. Near the trench the subducted slab has not reached transition zone depths (that would only happen for a near vertical subduction angle), which is seen in tomographic images with trench perpendicular cross sections (e.g., Kárason and van der Hilst, 2000). If splitting of the 520-km discontinuity is related to slab accumulation, our observations would be consistent with that. A similar comparison between observations might be possible for the Coral Sea region (Courtier and Revenaugh, 2007), using tomography from Kárason and van der Hilst (2000) and Bijwaard et al. (1998). However, the overlap in coverage, and the observations of a split 520-km discontinuity are minimal (only present in 2 paths).

Another expected characteristic of a split 520-km discontinuity, if due to exsolution of Ca-perovskite, is that the shallower discontinuity near 500 km should be weaker than the deeper discontinuity near 560 km. We do not observe this in our data, nor is it characteristic of the results from Courtier and Revenaugh (2006) and Courtier and Revenaugh (2007). In fact, in all of these studies we consistently find the opposite to be true; the shallower feature is always a stronger reflector. This might arise from an increase in water that is expected to be present in the transition zone when large amounts of slab material is present. Frequency content of the seismic phases also play a role, when split detection of the two discontinuities might be

preferentially detected by short-period shear wave studies. Future studies that are aimed at detection of the 520-km discontinuity would be useful in determining the role of stagnant slabs in the transition zone.

The negative discontinuity (R(z), -2.5%) we observe at 598 km is only present in one path (path 3), however a similar feature is found in the literature, so it is worthy of a brief discussion. Shen and Blum (2003) found negative a feature beneath southern Africa near 600 km. Shen et al. (2008) found a similar feature beneath many stations in China using P-to-S converted phases. They attribute this low velocity feature to the accumulation of basaltic crust at the base of the transition zone. Most recently, Gao et al., (2010) found a velocity decrease at depths ∼450–660 km beneath some stations in northeast China, however they do not speculate about a possible origin. The suggestion that this feature is due to accumulated basaltic crust in the transition zone does not seem consistent with the predictions by Saikai et al. (2008) (discussed above).

*Mid-Mantle Reflectors*

The western Pacific has been referred to as a graveyard for fallen slabs (Fukao et al., 2009), and tomography shows that many slabs in this region accumulate at the base of the transition zone (see Fukao et al., 2009 for a complete review). However, stagnant slabs are temporary, they eventually penetrate the 660-km discontinuity and descend into the lower mantle; also visible in the aforementioned tomography. Wen and Anderson (1997), based on a geoid inversion, proposed that a chemical boundary layer might exist near 920 km. A chemical boundary layer at depths near 1200–1600 km caused by the high- to low-spin transition of $Fe^{2+}$ in ferropericlase has been suggested by Cammarano et al. (2010). Numerical modeling (Morra et al., 2010) is consistent with the existence of such a layer, and their results show that slabs might stall for a extended period of time, possibly tearing and/or fragmenting. These predictions imply a mantle rich with both long- and short-wavelength heterogeneity, and suggest that the convection style is layered, not global.

Figure 6 shows the spatial distribution of our mid-mantle observations, there does not seem to be any obvious pattern to their distribution. Their inclusion in our profiles is questionable which limits our ability to comment on their origin(s). Additionally, some of these reflectors can be modeled as velocity decreases with the same fit to data, in all cases we have chosen to model them as positive velocity changes. This

decision is based on evidence from other studies, and motivated by hydrodynamics in the mid-to-lower mantle. Density decreases are hydrodynamically instable in the lower mantle (Revenaugh and Jordan, 1991d), making it more favorable to model the velocity changes as positive. This assumes that the velocity decrease is due solely to a decrease in density, which might be a bad assumption.

Their have been a host of suggestions for the possible origins of mid-mantle reflectors (see Courtier and Revenaugh, 2008 for a review), however the most common suggestion is that they are related to slabs present in the lower mantle. Our results are consistent with this, however there are many instances of paired reflectors at nearby depths that are difficult to explain under this scenario. If we have included false observations in our model, that might explain the paired reflectors and obscure any pattern that would otherwise be present. We conclude that these results support the notion of mantle heterogeneity at mid-mantle depths, however they do not provide any insight about its origin(s). A better way to analyze this region, rather than including all possible reflectors, might be to employ the technique used by Revenaugh and Jordan (1991b). They used variance-weighted stacks of the reflectivity profiles to test for consistency, allowing them to resolve features with reflectivity coefficients as low as 0.5%. For the paths crossing northeast China including data from the Chinese National Digital Seismic Network might increase our ability to resolve some of these small amplitude features.

## 4.6 Conclusions

This study reveals the complex mantle structure that exists in the western Pacific. We find a G discontinuity at depths that are consistent with other studies of this region, underlain by intermittent observation of L and X. Crustal thicknesses reported for Hokkaido might explain our anomalously high reflection coefficients for H in some paths, and perhaps the lack of a G discontinuity in others. A melt layer near a depth of 350 km exists near the Nankai trough, appearing on both sides of the subducting slab. The 520-km discontinuity is split in some of our paths, and based on regional tomography, we conclude that exsolution of Ca-perovskite due to stagnant slabs at the base of the transition zone might be the cause. However, we note that observations of a split 520-km discontinuity beneath North America are not consistent with that explanation. A negative discontinuity at 528 km is found in one

path, and has been reported in other studies of this region. We are unable to speculate about its origin(s) and can not completely eliminate the possibility that it is an artifact. Seismic structure is not confined to the upper mantle, but is present in all of our paths and persists to depths near 1600 km. These reflectors may be slab-related, but future work in the western Pacific that focuses on the deeper reflectors is needed to elucidate their cause.

## 4.7 References


Akaogi, M., Ito, E., Navrotsky, A., 1989. Olivine-modified spinel-spinel transitions in the system $Mg_2SiO_4$–$Fe_2SiO_4$: Calorimetric measurements, thermochemical calculation, and geophysical application. Journal of Geophysical Research 94 (B11), 15671.

Bagley, B., Courtier, A. M., Revenaugh, J., 2009. Melting in the deep upper mantle oceanward of the Honshu slab. Physics of the Earth and Planetary Interiors 175 (3-4), 137.

Bagley, B., Revenaugh, J., 2008. Upper mantle seismic shear discontinuities of the Pacific. Journal of Geophysical Research 113 (B12), B12301.

Bijwaard, H., Spakman, W., Engdahl, E. R., 1998. Closing the gap between regional and global travel time tomography. Journal of Geophysical Research 103 (B12), 30055.

Bina, C., Helffrich, G., 1994. Phase transition Clapeyron slopes and transition zone seismic discontinuity topography. Journal of Geophysical Research 99 (B8), 15,853–15,860.

Cammarano, F., Marquardt, H., Speziale, S., Tackley, P. J., 2010. Role of iron-spin transition in ferropericlase on seismic interpretation: A broad thermochemical transition in the mid mantle? Geophysical Research Letters 37 (3).

Castle, J. C., 2003. Searching for seismic scattering off mantle interfaces between 800 km and 2000 km depth. Journal of Geophysical Research 108 (B2).

Chambers, K., 2005. Reflectivity of the 410-km discontinuity from PP and SS precursors. Journal of Geophysical Research 110 (B2).

Chen, L., Tao, W., Zhao, L., Zheng, T., 2008. Distinct lateral variation of lithospheric thickness in the Northeastern North China Craton. Earth and Planetary Science Letters 267 (1-2), 56.

Courtier, A., Revenaugh, J., 2006. A water-rich transition zone beneath the eastern United States and Gulf of Mexico from multiple ScS reverberations. Vol. 168 of Earth's Deep Water Cycle. AGU, Washington, D. C., pp. 181–193.

Courtier, A., Revenaugh, J., 2007. Deep upper-mantle melting beneath the Tasman and Coral Seas detected with multiple ScS reverberations. Earth and Planetary Science Letters 259 (1-2), 66.

Courtier, A. M., Revenaugh, J., 2008. Slabs and shear wave reflectors in the midmantle. Journal of Geophysical Research 113 (B8).

Demouchy, S., 2005. Pressure and temperature-dependence of water solubility in Fe-free wadsleyite. American Mineralogist 90 (7), 1084.

Deuss, A., 2002. A systematic search for mantle discontinuities using SS-precursors. Geophysical Research Letters 29 (8).

Deuss, A., Woodhouse, J., 2001. Seismic observations of splitting of the mid-transition zone discontinuity in Earth's mantle. Science 294 (5541), 354–7.

Dziewonski, A., 1981. Preliminary reference Earth model. Physics of The Earth and Planetary Interiors 25 (4), 297.

Feng, M., van der Lee, S., An, M., Zhao, Y., 2010. Lithospheric thickness, thinning, subduction, and interaction with the asthenosphere beneath China from the joint inversion of seismic S-wave train fits and Rayleigh-wave dispersion curves. Lithos 120 (1-2), 116.

Fischer, K. M., Ford, H. A., Abt, D. L., Rychert, C. A., 2010. The Lithosphere-Asthenosphere Boundary. Annual Review of Earth and Planetary Sciences 38 (1), 551.

Flanagan, M. P., Shearer, P. M., 1998. Global mapping of topography on transition zone velocity discontinuities by stacking SS precursors. Journal of Geophysical Research 103 (B2), 2673.

Fujiwara, T., Hirano, N., Abe, N., Takizawa, K., 2007. Subsurface structure of the "petit-spot" volcanoes on the northwestern Pacific Plate. Geophysical Research Letters 34 (13).

Fukao, Y., Obayashi, M., Nakakuki, T., 2009. Stagnant Slab: A Review. Annual Review of Earth and Planetary Sciences 37 (1), 19.

Fukao, Y., Widiyantoro, S., Obayashi, M., 2001. Stagnant slabs in the upper and lower mantle transition region. Reviews of Geophysics 39 (3), 291.

Gao, W., Matzel, E., Grand, S. P., 2006. Upper mantle seismic structure beneath eastern Mexico determined from P and S waveform inversion and its implications. Journal of Geophysical Research 111 (B8).

Gao, Y., Suetsugu, D., Fukao, Y., Obayashi, M., Shi, Y., Liu, R., 2010. Seismic discontinuities in the mantle transition zone and at the top of the lower mantle beneath eastern China and Korea: Influence of the stagnant Pacific slab. Physics of the Earth and Planetary Interiors 183 (1-2), 288.

Gorbatov, A., Kennett, B., 2003. Joint bulk-sound and shear tomography for Western Pacific subduction zones. Earth and Planetary Science Letters 210 (3-4), 527.

Gudmundsson, Ó., Sambridge, M., 1998. A regionalized upper mantle (RUM) seismic model. Journal of Geophysical Research 103 (B4), 7121.

Hales, A., 1969. A seismic discontinuity in the lithosphere. Earth and Planetary Science Letters 7 (1), 44.

Helffrich, G., 2000. Topography of the transition zone seismic discontinuities. Reviews of Geophysics 38 (1), 141.

Hirschmann, M., Aubaud, C., Withers, A., 2005. Storage capacity of $H_2O$ in nominally anhydrous minerals in the upper mantle. Earth and Planetary Science Letters 236 (1-2), 167.

Inoue, T., Weidner, D. J., Northrup, P. A., Parise, J. B., 1998. Elastic properties of hydrous ringwoodite ($\gamma$-phase) in $Mg_2SiO_4$. Earth and Planetary Science Letters 160 (1-2), 107.

Ita, J., Stixrude, L., 1992. Petrology, Elasticity, and Composition of the Mantle Transition Zone. Journal of Geophysical Research 97 (B5), 6849.

Kaneshima, S., 2003. Subparallel dipping heterogeneities in the mid-lower mantle. Journal of Geophysical Research 108 (B5).

Kárason, H., van der Hilst, R., 2000. Constraints on mantle convection from seismic tomography. Vol. 121 of Geophysical Monograph, The History and Dynamics of Global Plate Motions. American Geophysical Union, Washington, DC.

Katsumata, M., Sykes, L. R., 1969. Seismicity and Tectonics of the Western Pacific: Izu-Mariana-Caroline and Ryukyu-Taiwan Regions. Journal of Geophysical Research 74 (25), 5923.

Katsura, T., 2003. Post-spinel transition in $Mg_2SiO_4$ determined by high P–T in situ X-ray diffractometry. Physics of The Earth and Planetary Interiors 136 (1-2), 11.

Katsura, T., 2004. Olivine-wadsleyite transition in the system $(Mg,Fe)_2SiO_4$. Journal of Geophysical Research 109 (B2).

Katsura, T., Ito, E., 1989. The System $Mg_2SiO_4$-$Fe_2SiO_4$ at High Pressures and Temperatures: Precise Determination of Stabilities of Olivine, Modified Spinel, and Spinel. Journal of Geophysical Research 94 (B11), 15663.

Kawakatsu, H., Niu, F., 1994. Seismic evidence for a 920-km discontinuity in the mantle. Nature 371 (6495), 301.

Krüger, F., Baumann, M., Scherbaum, F., Weber, M., 2001. Mid mantle scatterers near the Mariana Slab detected with a double array method. Geophysical Research Letters 28 (4), 667.

Kumar, P., Kawakatsu, H., 2011. Imaging the seismic lithosphere-asthenosphere boundary of the oceanic plate. Geochemistry Geophysics Geosystems 12 (1).

Lawrence, J. F., Shearer, P. M., 2006. A global study of transition zone thickness using receiver functions. Journal of Geophysical Research 111 (B6).

Levin, V., 2000. Shear zones in the Proterozoic lithosphere of the Arabian Shield and the nature of the Hales discontinuity. Tectonophysics 323 (3-4), 131.

Li, A., Fischer, K. M., Wysession, M. E., Clarke, T. J., 1998. Mantle discontinuities and temperature under the North American continental keel. Nature 395 (6698), 160–163.

Morra, G., Yuen, D., Boschi, L., Chatelain, P., Koumoutsakos, P., Tackley, P., 2010. The fate of the slabs interacting with a density/viscosity hill in the mid-mantle. Physics of the Earth and Planetary Interiors 180 (3-4), 271.

Morris, P. A., 1995. Slab melting as an explanation of Quaternary volcanism and aseismicity in southwest Japan. Geology 23 (5), 395.

Müller, R. D., Sdrolias, M., Gaina, C., Roest, W. R., 2008. Age, spreading rates, and spreading asymmetry of the world's ocean crust. Geochemistry Geophysics Geosystems 9 (4).

Nakajima, J., Hasegawa, A., 2007. Tomographic evidence for the mantle upwelling beneath southwestern Japan and its implications for arc magmatism. Earth and Planetary Science Letters 254 (1-2), 90.

Niu, F., 2003. Seismic evidence for a chemical heterogeneity in the midmantle: A strong and slightly dipping seismic reflector beneath the Mariana subduction zone. Journal of Geophysical Research 108 (B9).

Niu, F., Kawakatsu, H., 1997. Depth variation of the mid-mantle seismic discontinuity. Geophysical Research Letters 24 (4), 429.

Obayashi, M., Sugioka, H., Yoshimisu, J., Fukao, Y., 2006. High temperature anomalies oceanward of subducting slabs at the 410-km discontinuity. Earth and Planetary Science Letters 243 (1-2), 149.

Peacock, S. M., 1999. Seismic Consequences of Warm Versus Cool Subduction Metamorphism: Examples from Southwest and Northeast Japan. Science 286 (5441), 937.

Pino, N. A., Helmberger, D. V., 1997. Upper mantle compressional velocity structure beneath the West Mediterranean Basin. Journal of Geophysical Research 102 (B2), 2953.

Revenaugh, J., Jordan, T. H., 1991a. Mantle Layering From ScS Reverberations 1. Waveform Inversion of Zeroth-Order Reverberations. Journal of Geophysical Research 96 (B12), 19749.

Revenaugh, J., Jordan, T. H., 1991b. Mantle Layering From ScS Reverberations 2. The Transition Zone. Journal of Geophysical Research 96 (B12), 19763.

Revenaugh, J., Jordan, T. H., 1991c. Mantle Layering From ScS Reverberations 3. The Upper Mantle. Journal of Geophysical Research 96 (B12), 19781.

Revenaugh, J., Jordan, T. H., 1991d. Mantle Layering From ScS Reverberations 4. The Lower Mantle and Core-Mantle Boundary. Journal of Geophysical Research 96 (B12), 19811.

Revenaugh, J., Sipkin, S. A., 1994. Mantle discontinuity structure beneath China. Journal of Geophysical Research 99 (B11), 21911.

Rychert, C. A., Shearer, P. M., 2009. A global view of the lithosphere-asthenosphere boundary. Science 324 (5926), 495–8.

Rychert, C. A., Shearer, P. M., Fischer, K. M., 2010. Scattered wave imaging of the lithosphere–asthenosphere boundary. Lithos 120 (1-2), 173.

Saikia, A., Frost, D. J., Rubie, D. C., 2008. Splitting of the 520-kilometer seismic discontinuity and chemical heterogeneity in the mantle. Science 319 (5869), 1515–8.

Schmid, C., Goes, S., van der Lee, S., Giardini, D., 2002. Fate of the Cenozoic Farallon slab from a comparison of kinematic thermal modeling with tomographic images. Earth and Planetary Science Letters 204 (1-2), 17.

Seno, T., Takano, T., 1989. Seismotectonics at the Trench-Trench-Trench triple junction off central Honshu. Pure and Applied Geophysics PAGEOPH 129 (1-2), 27.

Shearer, P. M., 1990. Seismic imaging of upper-mantle structure with new evidence for a 520-km discontinuity. Nature 344 (6262), 121.

Shearer, P. M., Masters, T. G., 1992. Global mapping of topography on the 660-km discontinuity. Nature 355 (6363), 791.

Shen, Y., 2003. Seismic evidence for accumulated oceanic crust above the 660-km discontinuity beneath southern Africa. Geophysical Research Letters 30 (18).

Song, T.-R. A., Helmberger, D. V., Brudzinski, M. R., Clayton, R. W., Davis, P., Pérez-Campos, X., Singh, S. K., 2009. Subducting slab ultra-slow velocity layer coincident with silent earthquakes in southern Mexico. Science 324 (5926), 502–6.

Song, T.-R. A., Helmberger, D. V., Grand, S. P., 2004. Low-velocity zone atop the 410-km seismic discontinuity in the northwestern United States. Nature 427 (6974), 530–3.

van der Lee, S., Nolet, G., 1997. Upper mantle velocity S structure of North America. Journal of Geophysical Research 102 (B10), 22,815–22838.

Vanacore, E., Niu, F., Kawakatsu, H., 2006. Observations of the mid-mantle discontinuity beneath Indonesia from S to P converted waveforms. Geophysical Research Letters 33 (4).

Vinnik, L., 2002. Subcratonic low-velocity layer and flood basalts. Geophysical Research Letters 29 (4).

Vinnik, L., 2003. Super-deep low-velocity layer beneath the Arabian plate. Geophysical Research Letters 30 (7).

Vinnik, L., Farra, V., 2007. Low S velocity atop the 410-km discontinuity and mantle plumes. Earth and Planetary Science Letters 262 (3-4), 398.

Wen, L., Anderson, D., 1997. Layered mantle convection: A model for geoid and topography. Earth and Planetary Science Letters 146 (3-4), 367.

Wessel, P., Smith, W. H. F., 1998. New, improved version of generic mapping tools released. Eos, Transactions American Geophysical Union 79 (47), 579.

Wittlinger, G., Farra, V., 2007. Converted waves reveal a thick and layered tectosphere beneath the Kalahari super-craton. Earth and Planetary Science Letters 254 (3-4), 404.

Xuzhang, S., Zhou, H., Kawakatsu, H., 2008. Mapping the upper mantle discontinuities beneath China with teleseismic receiver functions. Earth Planets Space 60 (7), 713–719.

Yoshii, T., 1979. A detailed cross-section of the deep seismic zone beneath northeastern Honshu, Japan. Tectonophysics 55 (3-4), 349.

Zang, S. X., Chen, Q. Y., Ning, J. Y., Shen, Z. K., Liu, Y. G., 2002. Motion of the Philippine Sea plate consistent with the NUVEL-1A model. Geophysical Journal International 150 (3), 809.

## 4.8 Figures

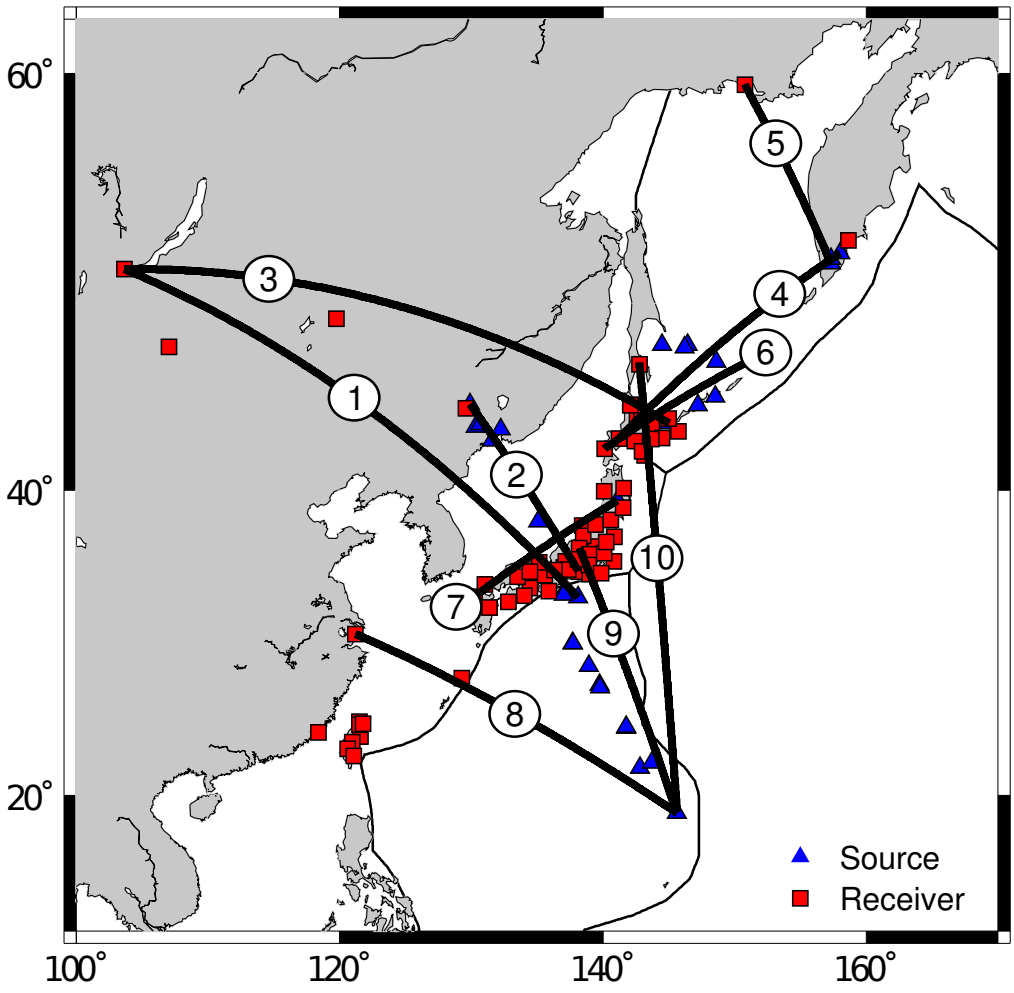


Figure 4.1: Mercator projection showing locations of sources (blue triangles) and receivers (red squares) used in this study. Bold lines show the regions sampled by the source-receiver combinations. Path numbers are shown in the circles.

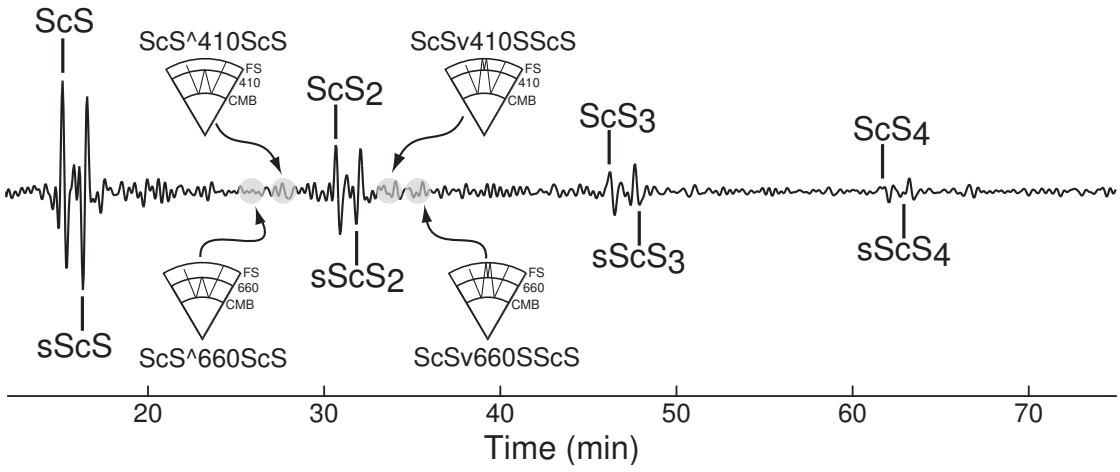


Figure 4.2: Long period, SH-polarized seismogram of the November 15, 1997 earthquake ($M_b$ 6.1, 161 km depth, Lat: 43.81 Lon: 145.02) recorded at station MDJ. Schematic representations of first-order $ScS_2$ reverberations are also shown; bottom-side reflections are shown on the left and top-side reflections are shown on the right. FS = Free Surface, 410 = 410-km discontinuity, CMB = core-mantle boundary.

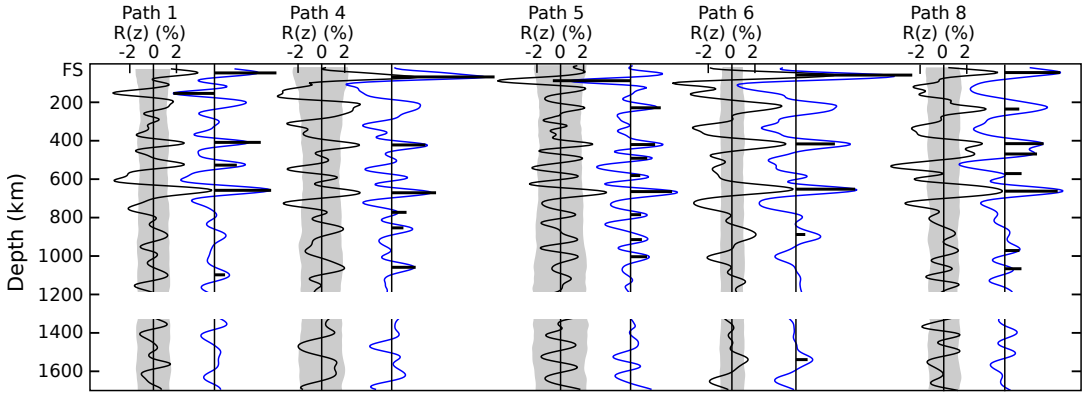


Figure 4.3: Reflectivity profiles for the five paths that do not contain a LVL. The abscissa is shear-wave reflection coefficient (R(z), %), the ordinate is depth (z, km). The black line is data, the blue line is the preferred synthetic profile. The horizontal bold bars mark the depth of the discontinuity modeled and their length is equal to the amplitude of the reflection coefficient. The gray ribbon along the data profile indicates the 95% confidence limit on reflector detection. The gap in data and synthetic profiles from 1200 to 1320 km results from unstable travel time estimates due to partial cancellations of top- and bottom-side reflections in that depth range.

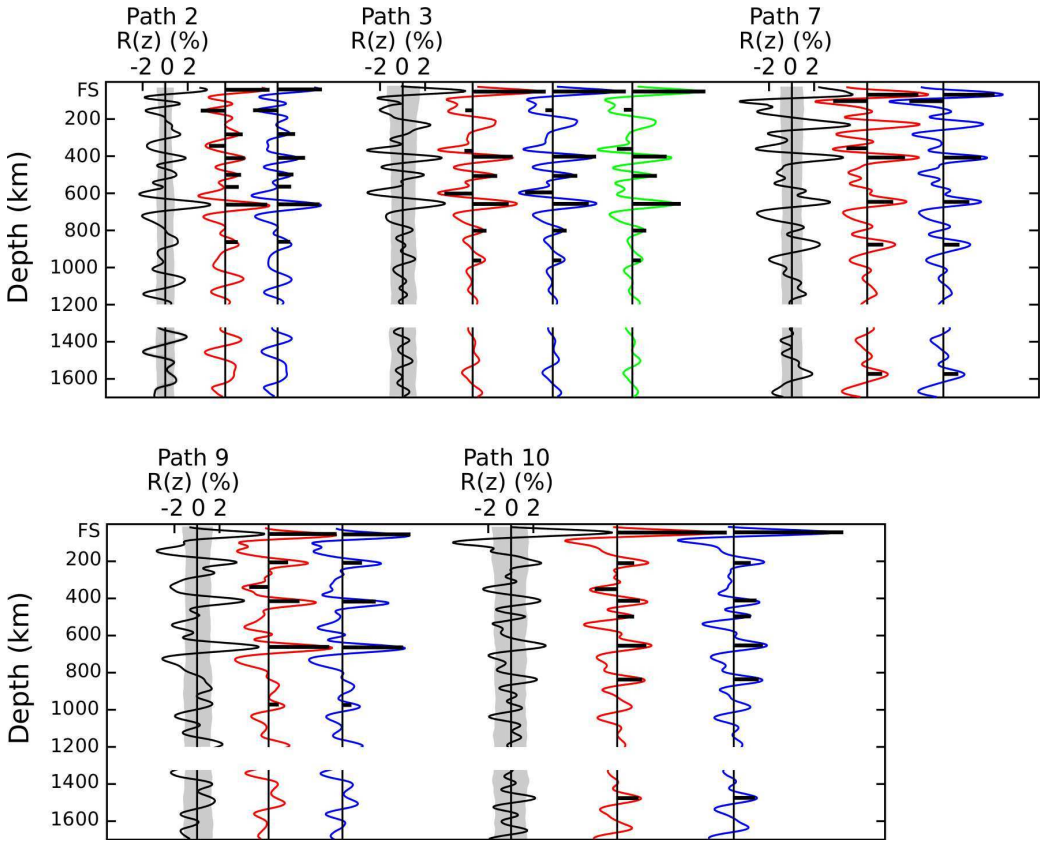


Figure 4.4: Reflectivity profiles for the five paths that contain a LVL. The abscissa is shear-wave reflection coefficient. The black line is data, the red line is the synthetic profile from a model containing a LVL, the blue line is the synthetic profile from a model that does not contain a LVL. The green line for path 3 is the synthetic profile from a model with the discontinuity at 598 km removed (see results section). The horizontal bold bars mark the depth of the discontinuity modeled and their length is equal to the amplitude of the reflection coefficient. The gray ribbon along the data profile indicates the 95% confidence limit on reflector detection. The gap in data and synthetic profiles from 1200 to 1320 km results from unstable travel time estimates due to partial cancellations of top- and bottom-side reflections in that depth range.

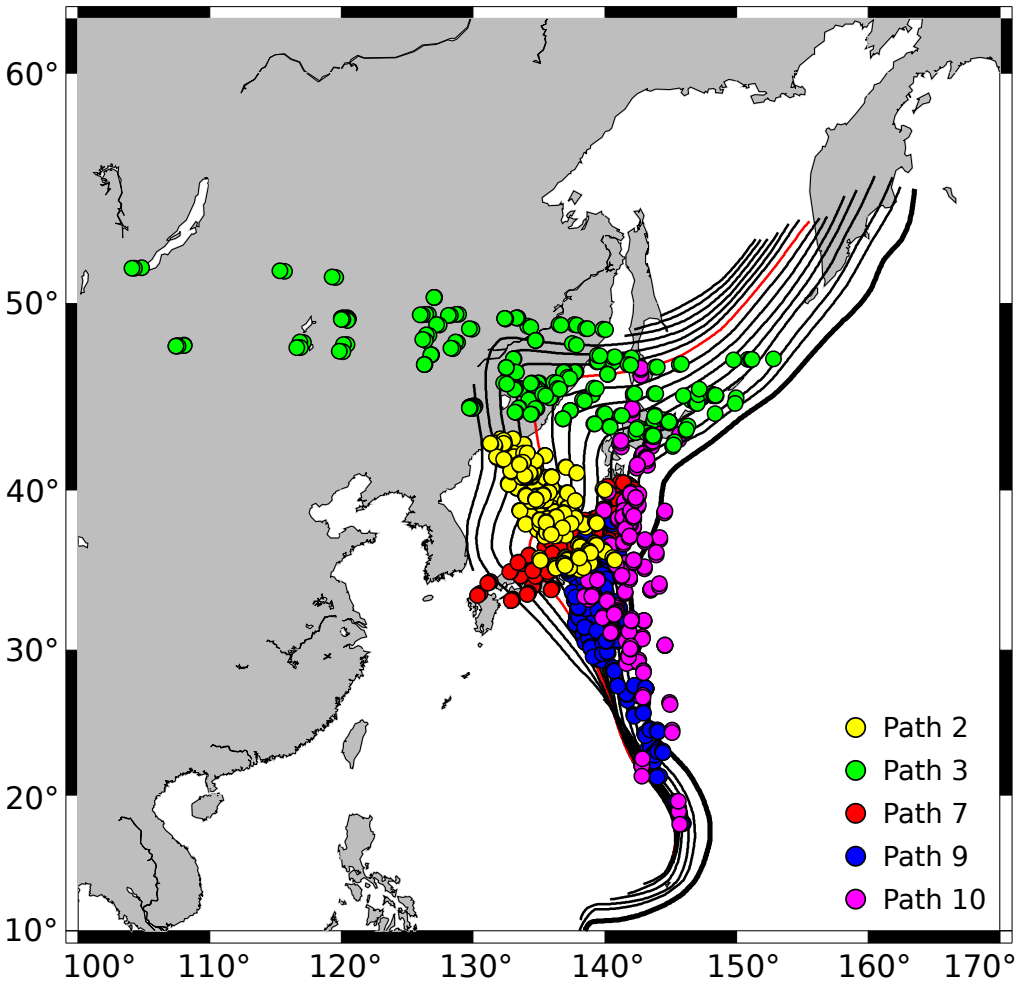


Figure 4.5: First order top- and bottom-side $ScS_n$ (n=1–4) reflections from 400 km for paths containing a LVL above the 410-km discontinuity. Individual paths are indicated by color circles (see legend). Contour lines (Gudmundsson and Sambridge, 1998) indicate depth to the top of the slab (defined by the seismogenic zone), the contour interval is 50 km, and the first bold line is 0 km (trench location). The red contour line corresponds to a depth of 400 km.

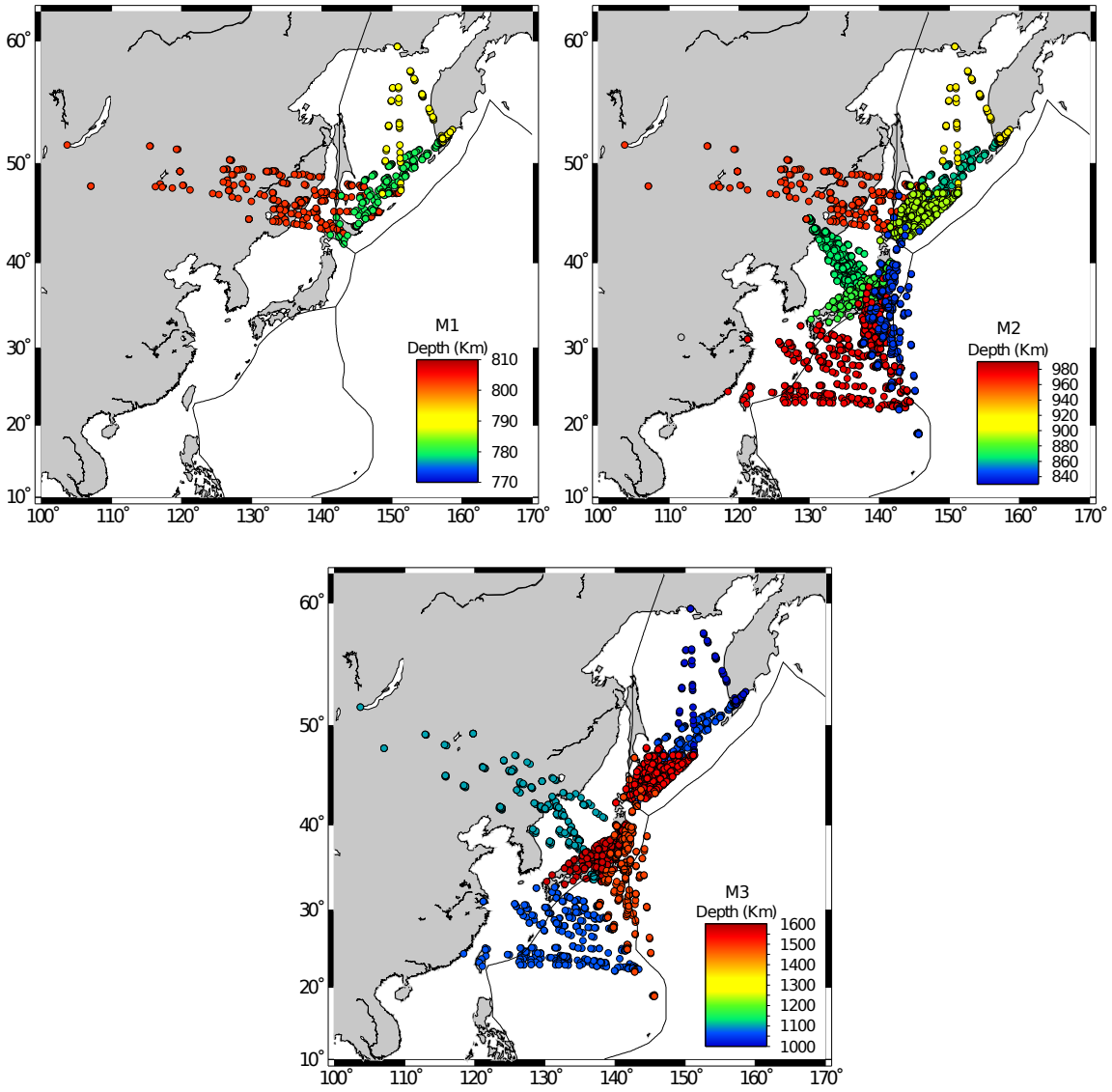


Figure 4.6: Spatial distribution of mid-mantle discontinuities, separated into three depth categories M1, M2, and M3 (see text for details).

## 4.9 Tables

Table 4.1: Source parameters for the earthquakes used in this study. Paths using each event are listed in the last column, numbers refer to Figure 1.

| **Date** | **Time UTC** | **Lat Deg** | **Lon Deg** | **Depth (km)** | $M_b$ | **Paths** |
|---|---|---|---|---|---|---|
| August 2, 1994 | 14:17:52 | 52.43 | 158.04 | 147 | 5.9 | 4 |
| March 31, 1995 | 14:01:41 | 38.15 | 135.06 | 361 | 6.2 | 1 |
| July 7, 1995 | 21:15:20 | 33.97 | 137.13 | 334 | 6.0 | 1 |
| February 22, 1996 | 14:59:09 | 45.26 | 148.54 | 124 | 6.3 | 3, 6 |
| March 16, 1996 | 22:04:06 | 28.98 | 138.94 | 477 | 6.7 | 8, 9, 10 |
| June 26, 1996 | 03:22:03 | 27.73 | 139.75 | 468 | 6.3 | 9, 10 |
| July 6, 1996 | 21:36:29 | 21.97 | 142.83 | 241 | 6.2 | 10 |
| July 15, 1996 | 16:51:22 | 18.73 | 145.63 | 176 | 6.3 | 8, 9, 10 |
| November 15, 1997 | 07:05:17 | 43.81 | 145.02 | 161 | 6.1 | 3, 6 |
| February 7, 1998 | 01:13:37 | 24.79 | 141.75 | 525 | 5.9 | 8, 9, 10 |
| February 7, 1998 | 01:19:00 | 24.83 | 141.75 | 525 | 6.4 | 10 |
| February 28, 1998 | 17:38:49 | 33.46 | 138.12 | 291 | 5.7 | 1, 7 |
| April 8, 1999 | 13:10:34 | 43.61 | 130.35 | 565 | 7.1 | 2 |
| May 12, 1999 | 17:59:22 | 43.03 | 143.84 | 102 | 6.5 | 3 |
| February 13, 2000 | 02:57:09 | 42.85 | 131.57 | 514 | 6.0 | 2 |
| March 28, 2000 | 11:00:23 | 22.34 | 143.73 | 126 | 7.6 | 8, 9 |
| June 9, 2000 | 22:35:14 | 30.47 | 137.68 | 472 | 5.8 | 8, 9, 10 |
| June 9, 2000 | 23:31:45 | 30.49 | 137.73 | 485 | 6.3 | 10 |
| December 22, 2000 | 10:13:01 | 44.79 | 147.20 | 140 | 6.3 | 3, 6 |
| October 3, 2001 | 17:25:13 | 47.08 | 148.63 | 285 | 5.9 | 5, 6 |
| December 2, 2001 | 13:01:54 | 39.40 | 141.09 | 123 | 6.5 | 1, 7 |
| June 3, 2002 | 09:15:01 | 27.56 | 139.78 | 488 | 5.9 | 8, 9, 10 |
| June 28, 2002 | 17:19:30 | 43.75 | 130.67 | 566 | 7.3 | 2 |
| September 15, 2002 | 08:39:33 | 44.83 | 129.92 | 586 | 6.4 | 2 |
| October 16, 2002 | 10:12:21 | 51.95 | 157.32 | 112 | 6.2 | 5, 4 |
| November 17, 2002 | 04:53:48 | 47.95 | 146.42 | 470 | 7.3 | 6 |
| November 17, 2002 | 04:53:54 | 47.82 | 146.21 | 461 | 5.8 | 3 |

*Continued on next page*

Table 4.1 – *Continued from previous page.*

| **Date** | **Time UTC** | **Lat Deg** | **Lon Deg** | **Depth (km)** | $M_b$ | **Paths** |
|---|---|---|---|---|---|---|
| August 31, 2003 | 23:08:01 | 43.48 | 132.24 | 480 | 6.2 | 2 |
| November 12, 2003 | 08:26:46 | 33.63 | 137.02 | 372 | 6.4 | 1 |
| July 8, 2004 | 10:30:49 | 47.20 | 151.30 | 128 | 6.4 | 3, 5, 6 |
| November 7, 2004 | 02:02:26 | 47.95 | 144.48 | 474 | 6.2 | 3, 6 |
| May 30, 2007 | 20:22:13 | 52.16 | 157.32 | 123 | 6.4 | 5, 4 |

Table 4.2: Discontinuity depths (z, km) and reflection coefficients (R(z), %) from preferred synthetic reflectivity profiles. See Figure 1 for path locations.

| **Path** | **H** | **G** | **L** | **X** | **Melt** | **410** | **Mid TZ** | **660** | **M1** | **M2** | **M3** |
|---|---|---|---|---|---|---|---|---|---|---|---|
| | z, R(z) | z, R(z) | z, R(z) | z, R(z) | z, R(z) | z, R(z) | z, R(z) | z, R(z) | z, R(z) | z, R(z) | z, R(z) |
| 1 | 48 5.3 | 153 -3.5 | | | | 411 4.0 | 530 1.9 | 662 4.9 | | | 1102 0.9 |
| 2 | 44 3.9 | 155 -2.2 | | 285 1.6 | 348 -1.4 | 413 1.7 | 503 1.4 | 664 3.7 | | 866 1.1 | |
| | | | | | | | 569 1.2 | | | | |
| 3 | 52 6.5 | 152 -0.7 | | | 373 -0.7 | 404 3.5 | 508 2.2 | 659 3.2 | 803 1.2 | 963 0.8 | |
| | | | | | | | 598 -2.5 | | | | |
| 4 | 70 8.8 | | | | | 427 2.9 | | 677 3.8 | 780 1.3 | 861 1.0 | 1066 2.1 |
| 5 | | 88 -6.7 | 231 2.6 | | | 425 2.1 | 496 1.4 | 671 3.6 | 791 0.9 | 922 1.0 | 1011 1.4 |
| | | | | | | | 587 0.8 | | | | |
| 6 | 60 10.0 | | | | | 420 3.3 | | 656 5.1 | | 892 0.8 | 1542 1.0 |
| 7 | 66 4.5 | 99 -3.0 | | | 357 -1.8 | 407 3.4 | | 646 2.3 | | 876 1.4 | 1570 1.3 |
| 8 | 45 4.7 | | 235 1.2 | | | 417 3.3 | 471 2.8 | 665 4.5 | | 975 1.3 | 1069 1.4 |
| | | | | | | | 573 1.4 | | | | |
| 9 | 55 6.0 | | 208 1.7 | | 343 -1.7 | 419 2.7 | | 666 5.4 | | 976 0.9 | |
| 10 | 48 9.7 | | 213 1.5 | | 355 -2.0 | 418 2.0 | 503 1.5 | 661 2.6 | | 843 2.2 | 1481 1.9 |

# Chapter 5

# Exploring the Geographic Distribution of Tremor: A Detection Algorithm for Sparsely Instrumented Regions

Brian Bagley and Justin Revenaugh
Department of Geology and Geophysics, University of Minnesota, 310 Pillsbury Drive SE, Minneapolis, MN 55455

Non-volcanic tremor is an intriguing phenomenon that occurs in a wide variety of tectonic settings. It has been found in subduction zones (e.g., Cascadia, Japan, Mexico, Costa Rica, and Alaska) and the San Andreas strike slip fault system. Fault slip occurs globally in a diversity of tectonic environments so it is reasonable to believe that it might be accompanied by non-volcanic tremor, however many parts of the world are sparsely monitored. Even in regions where seismic arrays exist they are often not suitable for the methods currently being used, most of which require a dense array to accommodate the use of various cross-correlation techniques. Developing a comprehensive overview of where tremor occurs, and where it doesn't occur, is key to understanding the mechanics behind it. For this reason we have developed a method for non-volcanic tremor detection that requires only two stations. We have tested our method in two regions during periods of known non-volcanic tremor activity. A third test was conducted in a region without non-volcanic tremor and/or large magnitude earthquakes. The results of these tests are very promising, and this method should prove to be useful in the creation of a global catalog.

## 5.1 Introduction

The discovery of non-volcanic tremor (herein referred to as tremor) has changed our fundamental understanding of the processes occurring at plate margins, and done so quite quickly ($\sim$ 10 years). Tremor is often correlated, both spatially and temporally, with slow-slip events along faults and populated with low-frequency earthquakes (LFEs) (Rogers and Dragert, 2003; Obara and Hirose, 2006; Shelly et al., 2006, 2007a; Maeda et al., 2009; Wech et al., 2009; Kao et al., 2009). In regions where tremor has been observed to be periodic (e.g., Cascadia) it is referred to as Episodic Tremor and Slip (ETS) (Rogers and Dragert, 2003). Tremor and LFEs have emerged as signals with the potential to inform earthquake forecasting and hazard mitigation (e.g., Wech et al., 2009; Gomberg et al., 2010). Unlike large earthquakes ($M_w$ >7.0) that may only occur every few centuries, the recurrence interval of LFEs is on the order of days (e.g., Shelly, 2010) during a period of tremor activity.

Fault slip occurs globally in a diversity of tectonic environments, but many parts of the world are sparsely monitored. There is considerable variation in the characteristics of tremor, presumably this results from differences in local tectonics. In Japan, tremor is widely observed with Philippine Sea plate subduction in the Nankai Trough, but is not observed at all with Pacific Plate subduction in the Japan Trench (Obara, 2002). Until recently it was thought that slow slip occurred without tremor in New Zealand (Delahaye et al., 2009). However, tremor triggered by the February 27, 2010 Chilean earthquake ($M_w$ 8.8) near the Hikurangi subduction zone was recently discovered (Fry et al., 2010). Initial locations suggest the tremor is located on the southern end of the north island, and it appears to be modulated by love waves from the earthquake. In addition to subduction zones, tremor has been detected outside of subduction zone environments on the San Andreas Fault (SAF) system in California.

In the past decade the most prominently studied areas have been the Nankai Trough subduction zone in southwest Japan (e.g., Obara, 2002; Obara and Hirose, 2006; Shelly et al., 2006, 2007a; Ide et al., 2007), the Cascadia subduction zone (e.g., Dragert et al., 2001; Rogers and Dragert, 2003; Kao et al., 2005), and the San Andreas strike slip fault system (SAF) (e.g. Nadeau and Dolenc, 2005; Gomberg et al., 2008; Shelly, 2009). Non-volcanic tremor has also been discovered in Costa Rica (Schwartz et al., 2007), Alaska (Peterson and Christensen, 2009), and Mexico (Payero et al., 2008). The basic characteristics of tremor, a weak and extended signal most prominent at 1–10 Hz, are similar in all of these regions (Figure 1). Tremor on the

SAF has shorter recurrence intervals and duration, smaller peak amplitudes, and less energy release than tremor in subduction zones (Nadeau and Dolenc, 2005). There are also subtle differences in tremor amongst the various subduction zones and these may be attributable to slab age (temperature), subduction rate, and compositional differences in the crust and upper mantle. Despite these variations, the working hypothesis is that tremor and slow-slip are related and that the fundamental explanation for slow-slip is likely common to all locations.

Tremor is difficult to detect because it is a low amplitude transient signal, with amplitudes of $\sim$ 1 micron per second, that lack the sharp, impulsive body wave arrivals used to locate regular earthquakes. Most methods developed to detect tremor have been based on cross-correlation techniques, which has worked well in areas (i.e. Japan) that benefit from dense seismic arrays (Obara, 2002; Shelly et al., 2007a; Brown et al., 2009; Suda et al., 2009). In Cascadia, where the station coverage is not as dense as southwest Japan, Kao et al. (2007) developed a detection technique that employs a moving average and scintillation index. In this case waveform cross-correlation is not used, however tremor arrivals must be present at three nearby ($\sim$ 100 km) stations for the arrival to be classified as coherent tremor (distance and number of stations are tunable parameters). This has worked very well in Cascadia, such that this detection method is used operationally in the real-time Tremor Activity Monitoring System (TAMS) (Kao et al., 2008). Creager and Wech (2008) developed a method known as Waveform Envelop Correlation and Clustering (WECC) that is used for real-time monitoring in the Pacific northwest. Based on the WECC method Wech (2010) created an interactive tremor map that is available to the public online (http://www.pnsn.org/tremor). Japan also has a real-time monitoring system, Automatic Tremor Monitoring System (ATMOS), based on the method developed by Suda et al. (2009). A number of other detection algorithms have been developed and tested in Japan and/or Cascadia (Brudzinski and Allen, 2007; Ghosh et al., 2009, 2010; Maceira et al., 2010), all with good results.

From the beginning, fluids have been thought to be very important to the tremor process (Julian, 2002). In most cases fluids are thought to be responsible for the elevated pore pressures that possibly trigger slip events, though where the fluids originate is still uncertain. In subduction zones like Japan and Cascadia (i.e. relatively warm) dehydration of the subducting slab could be an important source for fluids (e.g., Julian, 2002; Rogers and Dragert, 2003; Kao et al., 2009). Regions of high P-

to S-wave velocity ratios (Vp/Vs) in tomographic images have been shown to coincide with the tremor source region in Japan (Shelly et al., 2006). At a finer scale, Matsubara et al. (2009) showed a correlation between tremor sources and regions of high Vp/Vs beneath southwestern Japan and similar results using stacked receiver functions have been reported for Cascadia (Audet et al., 2009, 2010), consistent with high pore pressures. In colder subduction zones such as Costa Rica, fluids may be due to the dehydration of lower temperature hydrous phases (e.g., Brown et al., 2009). Slab dehydration certainly does not apply to the SAF, however fluids might be derived from serpentinite bodies present at depth, or from deep mantle sources (Nadeau and Guilhem, 2009). The possibility that fluids might be responsible for enabling slip by lowering pore-fluid pressure suggests the magnitude of stresses involved are low. Low levels of stress are also supported by the observation of tremor being triggered or modulated by earth tides and surface waves from distant earthquakes (Shelly et al., 2007b, Rubinstein et al., 2008; Nakata et al., 2008; Thomas et al., 2009).

Triggering of non-volcanic tremor by surface waves from earthquakes has been observed on the SAF (Peng et al., 2008; Gomberg et al., 2008; Shelly, 2009; Nadeau and Guilhem, 2009). Love waves from the Mw 7.8 2002 Denali earthquake triggered tremor in Cascadia (Rubenstein et al., 2007) and, as mentioned previously, triggered tremor has also been recently observed in New Zealand (Fry et al., 2010). Obara (2002) documented triggered tremor in Japan before and after local moderately sized earthquakes. Modulation by Earth tides has also been well documented in Japan (e.g., Shelly et al., 2007b; Nakata et al., 2008) and Cascadia (e.g., Rubenstein et al., 2008; Lambert et al., 2009). Triggering, whether by Earth tides or earthquakes, has reinforced the notion that the effective normal stresses along the slowly slipping portion of the fault are low and fluids likely play a role.

Accurate detection and source location are essential for the future of earthquake hazards and/or forecasting. Chapman and Melbourne (2009) have used slow-slip to constrain the down-dip limit of stress accumulation on the plate interface. Their results suggest that the potential rupture zone is located at a depth of 25 km, inland, rather than at a depth of 15 km, offshore, as previously thought (Hyndman and Wang, 1993; Hyndman and Wang, 1995). This shifts the potential rupture zone of the next megathrust earthquake closer to metropolitan areas and requires a reassessment of potential ground motion. Tremor also seems to be anti-correlated with larger seismic events, or put another way, tremor correlates well with the seismic gap (e.g., Kao et

al., 2009; Gomberg et al., 2010). If active faults tend to rupture in areas that are not able to release stresses through slow slip, this observation would help identify the most potentially hazardous areas. Of course, lack of tremor in regions that have recently experienced large earthquakes could also be due to reduced crustal stress and/or lower fluid pore pressure that inhibits tremor.

Developing a comprehensive overview of where tremor occurs, and where it doesn't occur, is key to understanding the mechanics behind it. The study of tremor has thus far been confined to regions of dense instrumentation, and due to limited resources, these are normally located along active margins (i.e. subduction zones) that are both densely populated, and in developed countries. A method for detecting tremor that does not require a dense seismic array is a necessary first step in understanding this intriguing phenomenon.

## 5.2 Lessons Learned

Using a limited number of stations (i.e., less than three) to search for tremor is a limiting factor when considering the type of algorithm to develop. Additionally, we intend to use this algorithm to search for tremor globally. Accomplishing these goals requires a method that is both automated, robust, and conservative. The need for automation is obvious, by robust, we mean that the method must be sensitive to tremor with a range of characteristics. Finally, the need to check the results of a global study for false positives would be an overwhelming task. Therefore, a conservative method, one that underestimates tremor rather than producing false positives is preferable. During the development of our method we pursued several ideas that did not work, for various reasons. Before discussing the working method it is worth examining what we learned from the failures.

The power spectrum of tremor compared to earthquakes of various magnitudes, ambient noise, and other transient signals is distinct in several ways. It can be characterized in terms of total power, its apparent lack of higher frequencies relative to earthquakes of a similar magnitude, and its overall shape. These subtle differences can be quantified by calculating spectral kurtosis (SK), spectral skewness (SS), mean frequency, the sum of power, and a spectral ratio (these will be referred to as diagnostic variables). We define spectral ratio to be the ratio between the sum of power at high and low frequencies, with the values for high and low being tunable parameters.

These diagnostic variables were chosen for their ability to characterize a power spectrum, not only in terms of power and frequency content, but also its shape. Kurtosis and skewness provide measures of the "peakedness" and asymmetry of a probability distribution function (PDF), respectively. The sum of power, mean frequency, and spectral ratio were chosen as additional variables that might useful for eliminating noise and large magnitude earthquakes. The idea being, if we treat the power spectrum as a PDF, we should be able to use these variables to characterize periods of tremor.

Spectral kurtosis was originally introduced by Dwyer (1983) as a complement to power spectral density (PSD). Antoni (2006) used SK to characterize non-stationary transient signals, developed an algorithm to calculate a "kurtogram", and demonstrated its applications (Antoni, 2007). Since then SK has been used to monitor tooth cracks in wind turbine gears (Barszcz and Randall, 2009) and detect subterranean termites (de la Rosa and Munoz, 2008). These examples demonstrate that SK can be a robust method for detecting transient signals buried in noise. We did not follow any of the methods in these examples strictly, but our definition of SK is very similar. We define SK and SS as

$$SK = \frac{\frac{1}{n}\sum_{i=1}^{n} S_i(f_i - \bar{f})^4}{\frac{\sum_{i=1}^{n} S_i}{\frac{1}{n}(\sum_{i=1}^{n} S_i(f_i - \bar{f})^2)^2}}, \tag{1}$$

$$SS = \frac{\frac{1}{n}\sum_{i=1}^{n} S_i(f_i - \bar{f})^3}{\frac{\sum_{i=1}^{n} S_i}{\frac{1}{n}(\sum_{i=1}^{n} S_i(f_i - \bar{f})^2)^{\frac{3}{2}}}}, \tag{2}$$

where n is the number of positive fourier frequencies, f is frequency, and S is the amplitude of a discrete frequency. The algorithm is straightforward, requires very little preprocessing, and is computationally inexpensive. The preprocessing step involves nothing more than bandpass filtering to eliminate very low ($< .1$ Hz) and high ($> 10$

Hz) frequencies. The data are then separated into overlapping windows, the PSD for each window is estimated, and the diagnostic variables are calculated. The results are sensitive to window length, the frequency range of the bandpass filter, and the definition of high and low frequencies used for the spectral ratio. Slight changes in these parameters do not produce drastically different results. The last step is to examine the diagnostic variables for each window and determine whether or not tremor is present. The results are robust for brief periods of time (e.g., several months), but not consistent between stations. Variations in noise and other transient signals causes the values of the diagnostic variables to change through time. Differences in site response among stations make it necessary to re-tune the method for each station used in the study. This means that at a given station for a brief period of time the diagnostic variable are unique for tremor, however we can not predict what they will be. At this point we decided to use multivariate analysis techniques to separate the variables into clusters.

Canonical Variate Analysis (CVA) is a technique used to separate data into groups. For example, it is often used in biological research to separate organisms with similar morphology into distinct groups. In our case we would like to separate tremor, low-magnitude earthquakes, noise and other non-tremor signals into separate groups based on the values of their diagnostic variables. CVA was originally developed by Fisher (1936) and an excellent review of the method is provided by Campbell and Atchley (1981). I will give a brief overview of how the method works before discussing our results. Campbell and Atchley (1981) describe CVA as a two-stage process, with the first stage being a principal component analysis (PCA) of the original variables. This first stage rotates the axes of the original system to a new orthogonal system in which the new axes define the direction of maximum variation of the original variables. These new PCA variables are then scaled to have unit variance among the groups, making them orthonormal. The second stage involves a rotation of the new orthonormal axes. While the first-stage rotation reveals variance within groups, the second-stage rotation reveals patterns between groups. Reversing the scaling and rotation from the first-stage analysis provides the canonical vectors, which are not necessarily orthogonal. PCA finds linear combinations of variables that show the maximum overall variation. CVA differs by finding linear combinations of variables that show the maximum ratio of between- to within-group variation. It is the ability of CVA to find between-group variation that is of interest to us. In practice CVA uses

a training dataset to classify the results into preexisting groups. The requirement to have a priori knowledge of the group characteristics presents us with a problem similar to the one before; these characteristics change through time and among stations. At this point we chose to pursue an entirely different approach, which will be described in the method section below.

## 5.3 Data

We collected continuous waveform data from three seismic networks; High Resolution Seismic Network (HRSN), Pacific Northwest Seismic Network (PNSN), and Earthscope's USArray (Table 1). These data were selected to test the algorithm in a variety of tectonic settings during periods of known tremor activity, with the exception of the USArray data which were selected to test the algorithm during a seismically quiet period (Figures 2–4). These data were visually inspected and stations with high signal to noise ratios with minimal data loss during the periods of interest were selected. The resulting dataset includes 5 months of HRSN data surrounding the $M_w$ 6.0 Parkfield earthquake, 3 months of data from the PNSN during a period of known ETS, and 2 months of data from the USArray. Tremor catalogs are readily available for Parkfield, California (Nadeau and Guilhem, 2009) and the Pacific Northwest (Wech, 2010) making these data perfect for this study. Continuous waveform data were separated into 24-hour segments, decimated to 20 Hz, and the trend and mean were removed.

## 5.4 Method

Our method makes use of the fact that tremor has a relatively wide bandwidth (1 to 10 Hz) compared to other transient signals. We begin by creating a filter bank consisting of four waveforms that are bandpass filtered from 1–2 Hz, 2–3 Hz, 3–4 Hz, and 4–5 Hz using a 4 pole butterworth filter. The choice of these particular filer bands is based on trial and error testing using data during a time with exceptionally distinct tremor, a more quantitative analysis of the appropriate frequency bands will be completed in the future. These traces are then converted to envelop functions, decimated to 1 Hz, and are individually analyzed using a five minute sliding window

advanced by 1 second. For each 5 minute window we calculate the mean and standard deviation. Using an envelop function decimated to 1 Hz, rather than the actual seismogram, we achieve a smoothing that produces better estimates of the mean and standard deviation. Our initially choice of a 5 minute window advanced by 1 second was guided by the results from other workers (e.g., (Nadeau and Guilhem, 2009; Wech, 2010), However, additional testing using different window lengths and step sizes has shown this to be a better choice, at least qualitatively.

The purpose of this first pass is to remove earthquakes, calibration pulses, and other high-amplitude events. This is accomplished by checking the amplitude 1 second forward in time and setting that position equal to zero if it is larger than a specified threshold based on the mean and standard deviation. Next we calculate the mean of all the 5 minute window means, a multiple of this is used as the tremor detection threshold (a multiple of 2 in most cases). A search for tremor is performed using a 30 second sliding window advanced by 1 second. If the maximum amplitude of the 30 second window exceeds the tremor detection threshold it is counted as possible tremor. The choice of a 30 second window is also the result of trial and error testing using high quality data, a more quantitative analysis will be performed in the future. This is repeated for each waveform in the filter bank and signals that do not exceed the tremor detection threshold in all four frequency ranges are eliminated as possible tremor (Figures 5 and 6). The final step is to compare the results of two stations, possible tremor coherent among two stations is counted as tremor. The programs used to accomplish this can be found in Appendix A.

## 5.5 Results

To test the method we compared our results with the tremor catalogs available for Parkfield, California (Nadeau and Guilhem, 2009) and the Pacific northwest (Wech, 2010). For Parkfield, our results match the catalog very well with the exception of the VARB/GHIB station pair for the period beginning 2004, 361 (Julian date) (Figure 7). All of this activity is recorded for day 365, and is due to data preprocessing, the seismograms for VARB and GHIB were incomplete for this day and were padded with zeros. Zero padding substantially reduces the mean of the 5 minute window means, and subsequently the tremor detection threshold, which causes the non-zero portion of the seismogram to be erroneously counted as tremor. The large peak for the period

beginning 2004, 312 for the VARB/VCAB station pair was visually verified as tremor that is not present in the Parkfield catalog. This activity is not present at station GHIB so it is not present in the results using that station. This incoherence between stations is likely why it is not present in the Parkfield catalog. Overall the results for the Parkfield region are very good.

Wech (2010) separates Cascadia into 7 overlapping regions for the purposes of detecting and counting tremor activity. The three stations we chose straddle the northern Washington and Vancouver Island regions. Figure 8 shows the tremor activity for those two regions compared to the results of our stations. A comparison of tremor activity and onset times between northern Washington and Vancouver Island demonstrates the variability of tremor in this region. The results of our three 2-station comparisons are very consistent with one another, and they all follow the general trend of the tremor activity catalog. The periods of time when tremor occurs match very well, however the amount of tremor activity we detect is far less. The reason for this is likely due to differences between the two methods and will be explored in more detail in the discussion and conclusions section.

For the final test we analyzed 2 months of data from 3 stations in northern Minnesota, a region that is seismically quiet. The purpose of this analysis is to test how the method performs in a region with no tremor and/or large magnitude earthquakes. The first analysis was done with the same tremor detection threshold that was used for Parkfield and Cascadia (a multiple of 2) (Figure 9). Notice that vertical scale of Figure 9 is minutes per day as opposed to minutes per week, this was done to get a better idea of precisely where the false positives are located. For most of the record the false tremor is less than 30 minutes per day, however there are few notable exceptions (e.g., days 323, 356, and 361). A visual inspection of these data (Figure 10) show that this problem arises from a situation similar to zero padding. We reanalyzed these data using a higher tremor detection threshold (a multiple of 3) (Figure 11). This drastically improved the results but a few false positives remain, however most of the record is zero. Examples of these data are shown in Figure 12.

## 5.6 Discussion and Conclusions

The main purpose of developing this method, since there are many already in use, is to address the need for tremor detection in regions that are sparsely instrumented.

To that end, we chose to use single stations for the initial development, but finally had to concede that a simple comparison between two stations vastly improved the results. The method was developed and tuned using data from Parkfield, California, and was tested in different regions without re-tuning. This is evident when considering the results of all three regions, Parkfield being the most consistent with the tremor catalog. However, it was never our intention to be able to find all tremor, only most (or some) of it. Being able to quickly and easily detect tremor at a global scale, regardless of array density for the purposes of documenting where tremor occurs, remains the primary objective. Locating tremor epicenters is the first step in a more rigorous analysis of tremor, which requires more than 2 stations. This implies that for a more detailed study additional station coverage will be available, or will have to be installed.

Another thing to consider when interpreting the results is the method used for creating the various tremor catalogs. For Parkfield, Nadeau and Guilhem (2009) use a 30 second window advanced by 1 second to find tremor, and they require the tremor duration to be at least 3 minutes. This is very similar to our method of tremor detection, and is perhaps another reason our results are so consistent with theirs. The WECC method (Wech, 2010) locates tremor first using 5 minute windows with a 50 percent overlap. Tremor locations with epicentral error estimates less than 5 km (bootstrap estimated error) and coherent between at least two stations in a predefined area are considered tremor. Their method is based on spatial coherency and relaxes the temporal constraint to a 5 minute period of time. This makes sense when considering the spatial distribution of the stations, however it likely results in our underestimation of tremor activity when compared to there results. In other words, we do not allow for time lags in the arrival of tremor between stations. This means that when we compare the results of 2 stations there will be tremor that is eliminated. We have attempted to be more consistent when comparing our results to those of Wech (2010) by counting any 5 minute window containing tremor as 5 minutes of tremor.

Another feature seen in the Cascadia data is the abrupt stop in tremor activity near day 250 (northern Washington) and day 260 (Vancouver Island), while our method records moderate activity until day 275 (the end of our analysis). It might be that as the ETS event comes to an end the WECC method can no longer locate tremor within the error required, while our method is still able to discern tremor based on its amplitude and duration. It is a reasonable assumption that tremor would slowly

stop rather than terminating abruptly.

Tremor can also migrate along the strike of the subducting slab. This is seen by observing the delay in the onset of tremor between northern Washington and Vancouver Island, which show a migration path of southeast to northwest (this can be seen in detail at http://www.pnsn.org/tremor). The stations we used straddle these two regions. This would explain why the peak activity for our tremor lies between the peaks for the Cascadia regions.

The results of the USArray test are reasonable, but they do demonstrate the need for a different way of handling quiet data. We would like to avoid the need for regional tuning, which is what these data required to obtain good results (i.e. setting the threshold higher). It might be possible to monitor the background amplitude and adjust the threshold multiplier accordingly. Additionally, zero padding is not the best method for handling incomplete data, as shown by the Parkfield results. Some of these shortcomings might originate from our parameter choices, many of which were determined by trial and error. At this point we have no quantitative error analysis regarding our parameter choices. A bootstrap error analysis of our frequency bands might reveal that one particular frequency band is biasing our results. It might also show that we have excluded a frequency band that contains useful information. From here additional error analysis of the mean and standard deviation could provide a more robust method for setting the tremor detection threshold. Given that noise levels change over time it is unreasonable to expect that a constant threshold, set daily, is the best method. A variable threshold, perhaps set by the noise level over longer durations of time, might yield better results.

Overall these results demonstrate that it is possible to detect tremor using only two stations. Even without regional tuning it is capable of detecting tremor in distinctly different tectonic settings. There is no doubt that the detection methods currently being used are robust methods for detecting tremor, however they all require the presence of a dense seismic array. A global catalog of where tremor occurs, and where it does not occur, would be extremely valuable in understand the processes involved. For that purpose this method should prove valuable.

## 5.7 References


Abers, G. A., MacKenzie, L. S., Rondenay, S., Zhang, Z., Wech, A. G., Creager, K. C., 2009. Imaging the source region of Cascadia tremor and intermediate-depth earthquakes. Geology 37 (12), 1119–1122.

Antoni, J., 2006. The spectral kurtosis: a useful tool for characterising non-stationary signals. Mechanical Systems and Signal Processing 20 (2), 282–307.

Antoni, J., 2007. Fast computation of the kurtogram for the detection of transient faults. Mechanical Systems and Signal Processing 21 (1), 108–124.

Audet, P., Bostock, M. G., Boyarko, D. C., Brudzinski, M. R., Allen, R. M., 2010. Slab morphology in the Cascadia fore arc and its relation to episodic tremor and slip. Journal of Geophysical Research 115, 1–15.

Audet, P., Bostock, M. G., Christensen, N. I., Peacock, S. M., 2009. Seismic evidence for overpressured subducted oceanic crust and megathrust fault sealing. Nature 457 (7225), 76–8.

Barszcz, T., Randall, R. B., 2009. Application of spectral kurtosis for detection of a tooth crack in the planetary gear of a wind turbine. Mechanical Systems and Signal Processing 23 (4), 1352–1365.

Brown, J. R., Beroza, G. C., Ide, S., Ohta, K., Shelly, D. R., Schwartz, S. Y., Rabbel, W., Thorwart, M., Kao, H., 2009. Deep low-frequency earthquakes in tremor localize to the plate interface in multiple subduction zones. Geophysical Research Letters 36 (19), 1–5.

Brudzinski, M., Allen, R., 2007. Segmentation in episodic tremor and slip all along Cascadia. Geology 35 (10), 907–910.

Campbell, N., Atchley, W., 1981. The geometry of canonical variate analysis. Systematic Zoology 30 (3), 268–280.

Chapman, J. S., Melbourne, T. I., 2009. Future Cascadia megathrust rupture delineated by episodic tremor and slip. Geophysical Research Letters 36 (22), 1–5.

de la Rosa, J., Moreno Muñoz, A., 2008. Higher-order cumulants and spectral kurtosis for early detection of subterranean termites. Mechanical Systems and Signal Processing 22 (2), 279–294.

Delahaye, E., Townend, J., Reyners, M., Rogers, G., 2009. Microseismicity but no tremor accompanying slow slip in the Hikurangi subduction zone, New Zealand. Earth and Planetary Science Letters 277 (1-2), 21–28.

Dragert, G., Wang, K., James, T. S., 2001. A silent slip event on the deeper Cascadia subduction interface. Science (New York, N.Y.) 292 (5521), 1525–8.

Dwyer, R., 1983. Detection of non-gaussian signals by frequency domain kurtosis estimation. In: Acoustics, Speech, and Signal Processing, IEEE International Conference on ICASSP'83. Vol. 8. IEEE, pp. 607–610.

Fisher, R., 1936. The use of multiple measurements in taxonomic problems. Annals of Human Genetics 7 (2), 179–188.

Fry, B., Chao, K., Bannister, S., Peng, Z., 2010. Triggered non-volcanic tremor in the hikurangi subduction zone, new zealand. Abstract S23A-2109 presented at Fall Meeting, AGU, San Fransisco, Calif., 13-17 Dec., 2109.

Ghosh, A., Vidale, J. E., Sweet, J. R., Creager, K. C., Wech, A. G., 2009. Tremor patches in Cascadia revealed by seismic array analysis. Geophysical Research Letters 36 (17), 1–5.

Ghosh, A., Vidale, J. E., Sweet, J. R., Creager, K. C., Wech, A. G., Houston, H., 2010. Tremor bands sweep Cascadia. Geophysical Research Letters 37 (8), 1–5.

Goldstein, P., Dodge, D., Firpo, M., Miner, L., 2003. International Handbook of Earthquake and Engineering Seismology, volume 81B, chapter SAC2000: Signal processing and analysis tools for seismologists and engineers. International Association of Seismology and Physics of the Earths Interior, 1613–1614.

Goldstein, P., Snoke, A., 2005. Sac availability for the iris community. Incorporated Research Institutions for Seismology Newsletter 7 (UCRL-JRNL-211140).

Gomberg, J., 2010. Slow-slip phenomena in Cascadia from 2007 and beyond: A review. Geological Society of America Bulletin 122 (7-8), 963–978.

Gomberg, J., Rubinstein, J. L., Peng, Z., Creager, K. C., Vidale, J. E., Bodin, P., 2008. Widespread triggering of nonvolcanic tremor in California. Science (New York, N.Y.) 319 (5860), 173.

Hyndman, R., Wang, K., 1993. Thermal constraints on the zone of major thrust earthquake failure: The cascadia subduction zone. Journal of Geophysical Research 98 (B2), 2039–2060.

Hyndman, R., Wang, K., 1995. The rupture zone of cascadia great earthquakes from current deformation and the thermal regime. Journal of Geophysical Research 100 (B11), 22133–22.

Ide, S., Shelly, D. R., Beroza, G. C., 2007. Mechanism of deep low frequency earthquakes: Further evidence that deep non-volcanic tremor is generated by shear slip on the plate interface. Geophysical Research Letters 34 (3).

Julian, B., 2002. Seismological detection of slab metamorphism. Science 296 (5573), 1625.

Kao, H., Philip, J., Rogers, G., Dragert, H., Spence, G., 2007. Automatic detection and characterization of seismic tremors in northern Cascadia. Geophysical Research Letters 34 (16), 1–6.

Kao, H., Shan, S., Dragert, H., Rogers, G., 2009. Northern Cascadia episodic tremor and slip: A decade of tremor observations from 1997 to 2007. Journal of Geophysical Research 114, 1–20.

Kao, H., Shan, S., Dragert, H., Rogers, G., Cassidy, J., Ramachandran, K., 2005. A wide depth distribution of seismic tremors along the northern Cascadia margin. Nature 436 (7052), 841–4.

Kao, H., Thompson, P., Shan, S., Rogers, G., Dragert, H., Spence, G., 2008. Tremor Activity Monitoring System (TAMS) Operating in Northern Cascadia. Eos Trans. AGU 89 (42), 405–406.

Kodaira, S., Iidaka, T., Kato, A., Park, J., Iwasaki, T., Kaneda, Y., 2004. High pore fluid pressure may cause silent slip in the nankai trough. Science 304 (5675), 1295.

Lambert, A., Kao, H., Rogers, G., Courtier, N., 2009. Correlation of tremor activity with tidal stress in the northern Cascadia subduction zone. Journal of Geophysical Research 114, 1–10.

Liu, Y., Rice, J. R., 2007. Spontaneous and triggered aseismic deformation transients in a subduction fault model. Journal of Geophysical Research 112 (B9), 1–23.

Maceira, M., Rowe, C., Beroza, G., Anderson, D., 2010. Identification of low-frequency earthquakes in non-volcanic tremor using the subspace detector method. Geophysical Research Letters 37 (6), L06303.

Maeda, T., Obara, K., 2009. Spatiotemporal distribution of seismic energy radiation from low-frequency tremor in western Shikoku, Japan. Journal of Geophysical Research 114.

Matsubara, M., Obara, K., Kasahara, K., 2009. High-VP/VS zone accompanying non-volcanic tremors and slow-slip events beneath southwestern Japan. Tectonophysics 472 (1-4), 6–17.

Nadeau, R., Guilhem, A., 2009. Nonvolcanic tremor evolution and the San Simeon and Parkfield, California, earthquakes. Science 325 (5937), 191.

Nadeau, R. M., Dolenc, D., 2005. Nonvolcanic Tremors Deep Beneath the San Andreas Fault. Science (January), 94720–94720.

Nakata, R., Suda, N., Tsuruoka, H., 2008. Non-volcanic tremor resulting from the combined effect of Earth tides and slow slip events. Nature Geoscience 1 (10), 676–678.

Obara, K., 2002. Nonvolcanic deep tremor associated with subduction in southwest japan. Science 296 (5573), 1679.

Obara, K., Hirose, H., 2006. Non-volcanic deep low-frequency tremors accompanying slow slips in the southwest Japan subduction zone. Earth Science 417, 33 – 51.

Payero, J., Kostoglodov, V., Shapiro, N., Mikumo, T., Iglesias, A., Pérez-Campos, X., Clayton, R., 2008. Nonvolcanic tremor observed in the Mexican subduction zone. Geophysical Research Letters 35 (7), 1–6.

Peng, Z., Vidale, J., Creager, K., Rubinstein, J., Gomberg, J., Bodin, P., 2008. Strong tremor near Parkfield, CA, excited by the 2002 Denali Fault earthquake. Geophysical Research Letters 35 (23), 1–5.

Peterson, C., Christensen, D., 2009. Possible relationship between nonvolcanic tremor and the 1998–2001 slow slip event, south central Alaska. Journal of Geophysical Research 114 (B6), 1–13.

Rogers, G., Dragert, H., 2003. Episodic tremor and slip on the Cascadia subduction zone: the chatter of silent slip. Science (New York, N.Y.) 300 (5627), 1942–1943.

Rubinstein, J. L., La Rocca, M., Vidale, J. E., Creager, K. C., Wech, A. G., 2008. Tidal modulation of nonvolcanic tremor. Science (New York, N.Y.) 319 (5860), 186–189.

Rubinstein, J. L., Vidale, J. E., Gomberg, J., Bodin, P., Creager, K. C., Malone, S. D., 2007. Non-volcanic tremor driven by large transient shear stresses. Nature 448 (August), 579–582.

Schwartz, S., Rokosky, J., 2007. Slow slip events and seismic tremor at circum-Pacific subduction zones. Rev. Geophys 45 (3).

Shelly, D., 2009. Possible deep fault slip preceding the 2004 Parkfield earthquake, inferred from detailed observations of tectonic tremor. Geophysical Research Letters 36 (17), 1–6.

Shelly, D., 2010. Periodic, chaotic, and doubled earthquake recurrence intervals on the deep San Andreas fault. Science (New York, N.Y.) 328 (5984), 1385–1388.

Shelly, D., Beroza, G. C., Ide, S., 2007a. Complex evolution of transient slip derived from precise tremor locations in western Shikoku, Japan. Geochemistry Geophysics Geosystems 8 (10).

Shelly, D., Beroza, G. C., Ide, S., 2007b. Non-volcanic tremor and low-frequency earthquake swarms. Nature 446 (7133), 305–307.

Shelly, D., Beroza, G. C., Ide, S., Nakamula, S., 2006. Low-frequency earthquakes in Shikoku, Japan, and their relationship to episodic tremor and slip. Nature (London) 442 (7099), 188–191.

Suda, N., Nakata, R., Kusumi, T., 2009. An automatic monitoring system for non-volcanic tremors in southwest Japan. Journal of Geophysical Research 114 (B), 1–15.

Thomas, A. M., Nadeau, R. M., Bu, R., 2009. Tremor-tide correlations and near-lithostatic pore pressure on the deep San Andreas fault. Nature 462 (December), 1048–1052.

Wech, A., 2010. Interactive Tremor Monitoring. Seismological Research Letters 81 (4), 664–669.

Wech, A., Creager, K., 2008. Automated detection and location of Cascadia tremor. Geophys. Res. Lett 35, 1–5.

Wech, A., Creager, K., Melbourne, T., 2009. Seismic and geodetic constraints on cascadia slow slip. Journal of Geophysical Research 114 (B10), 1–9.

Wessel, P., Smith, W. H. F., 1998. New, improved version of the generic mapping tools released. EOS Transactions of the American Geophysical Union 79, 579.

## 5.8 Figures

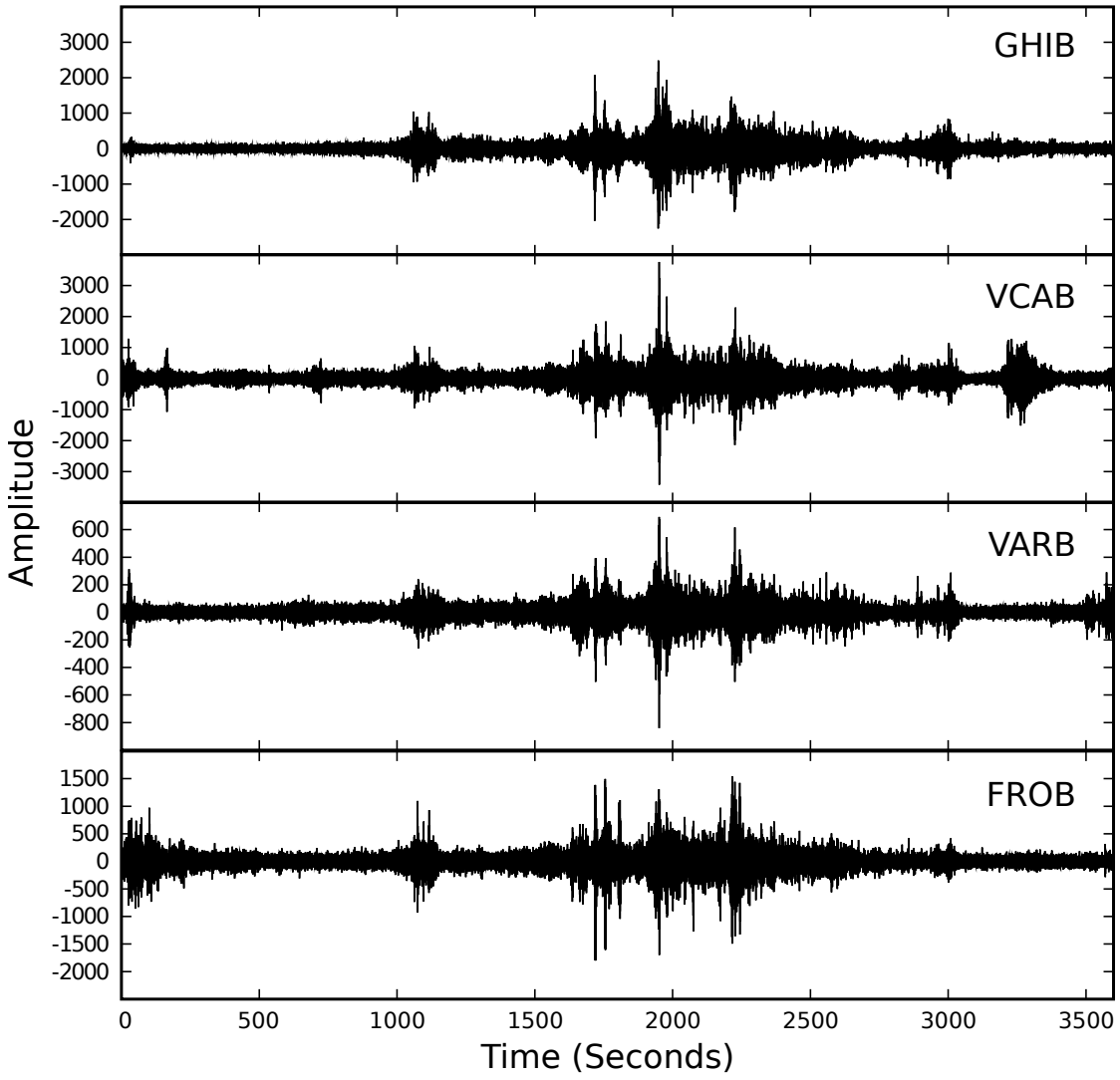


Figure 5.1: Example seismograms showing 1 hour of tremor, recorded near Parkfield, California on September 26, 2004 at stations GHIB, VCAB, VARB, and FROB. These data have been bandpass filtered from 2 to 8 Hz, the characteristic frequency band for tremor.

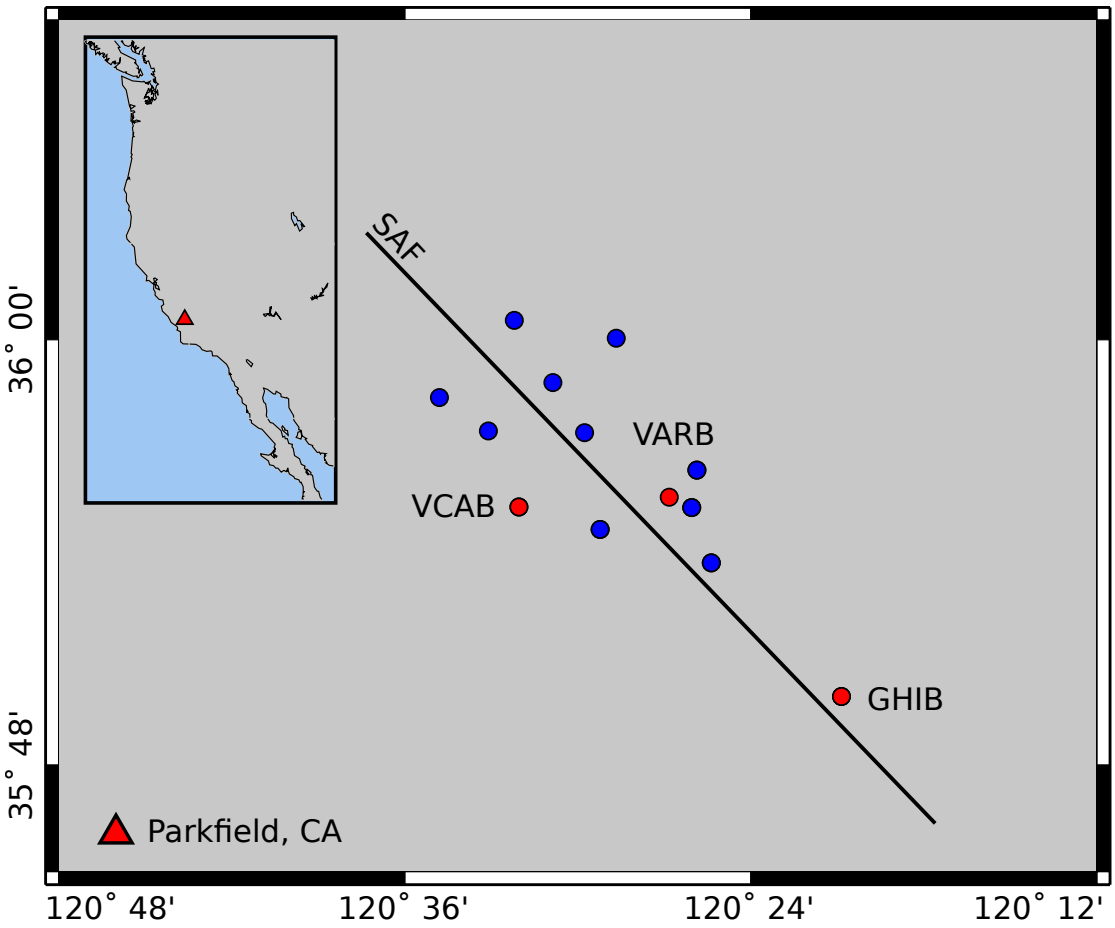


Figure 5.2: Map showing station locations (blue and red circles) for the High Resolution Seismic Network (HRSN) located near Parkfield, California. The red circles are the three stations used in this study. The San Andreas Fault is represented schematically by the bold black line.

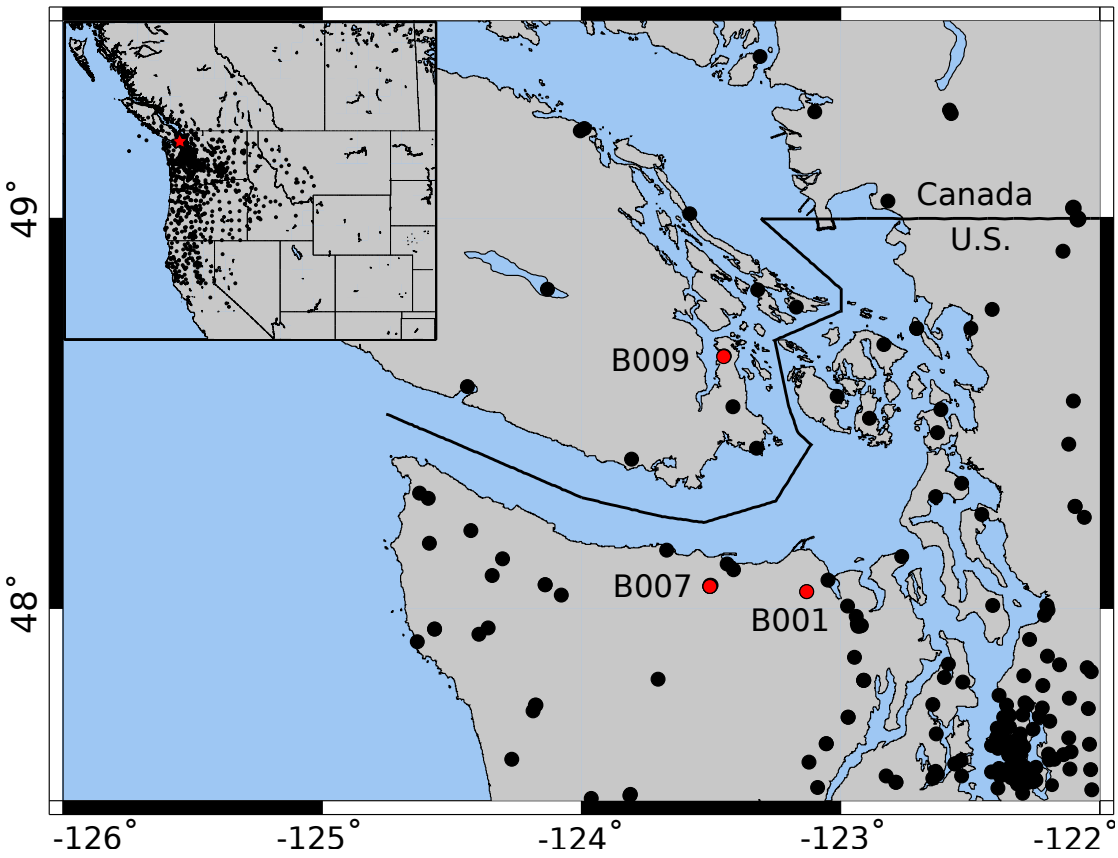


Figure 5.3: Map showing station locations (black and red circles) of the Pacific Northwest Seismic Network (PNSN). The red circles are the stations used in this study.

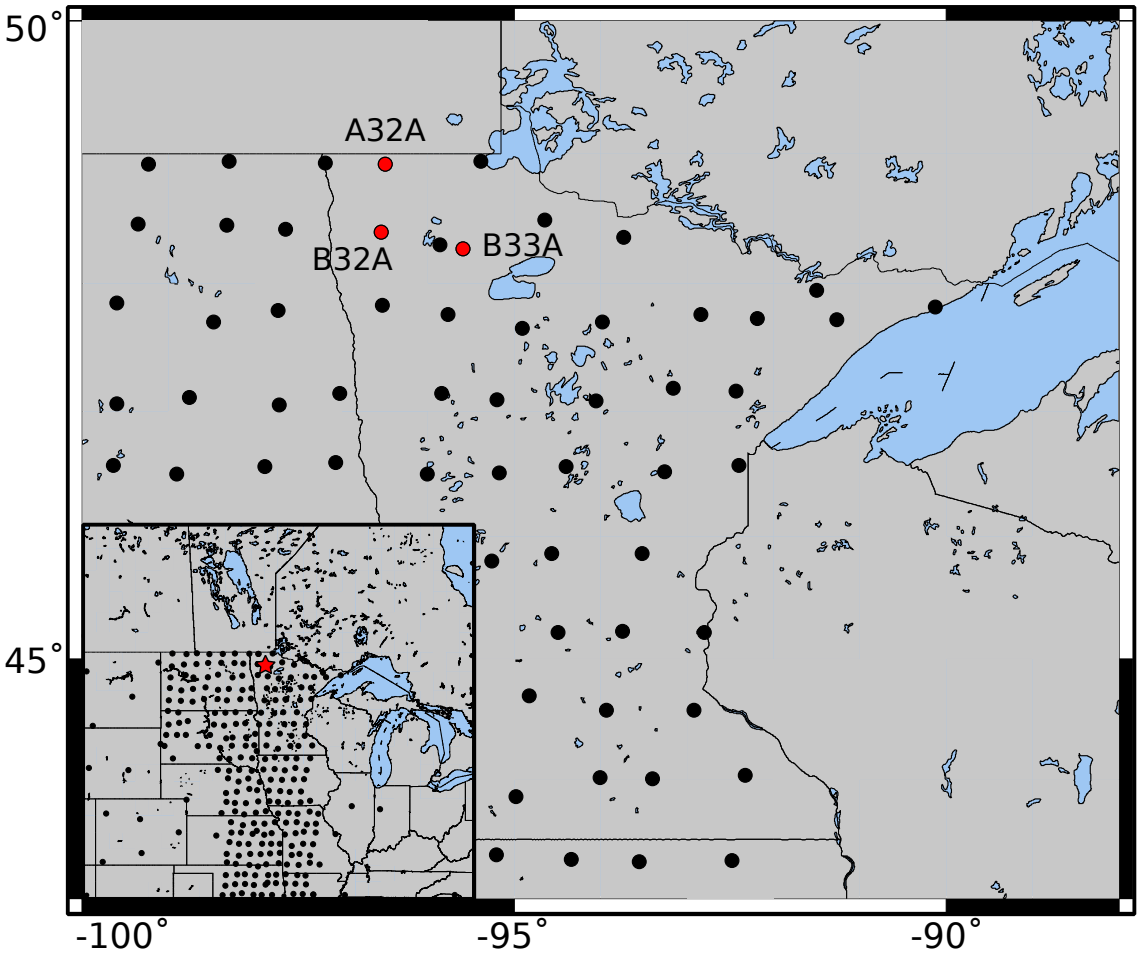


Figure 5.4: Map showing current locations of the USArray stations (black and red circles). The three red circles are the stations used in this study.

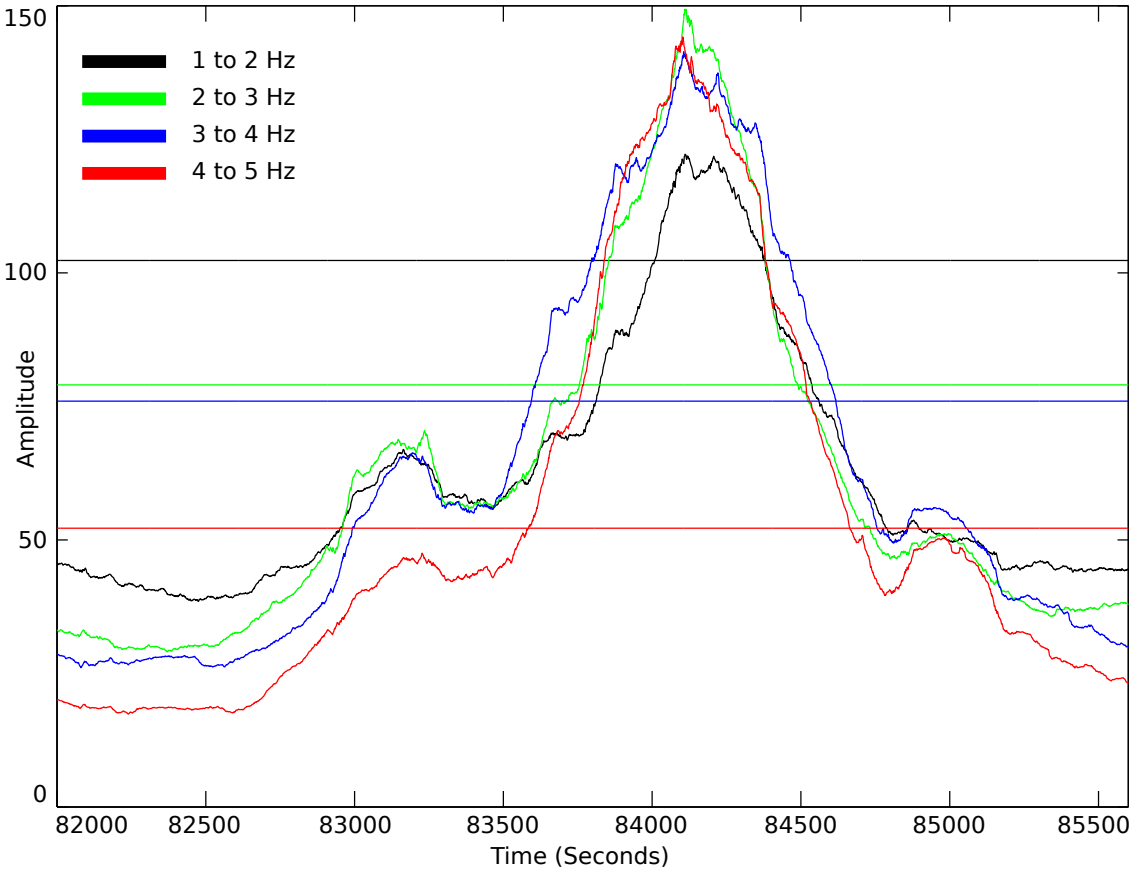


Figure 5.5: Example of approximately 30 minutes of possible tremor that is coherent across the filter bank. These waveforms are the result of converting individual seismograms into envelop functions, and then finding the mean of 5 minute windows advanced by 1 second. The corresponding (in color) horizontal lines are the tremor detection thresholds for each filter (see Method section for details). When all four waveforms exceed their respective thresholds that time period is counted as possible tremor (see legend for color explanation). It will not be counted as tremor until a comparison has been made between 2 stations.

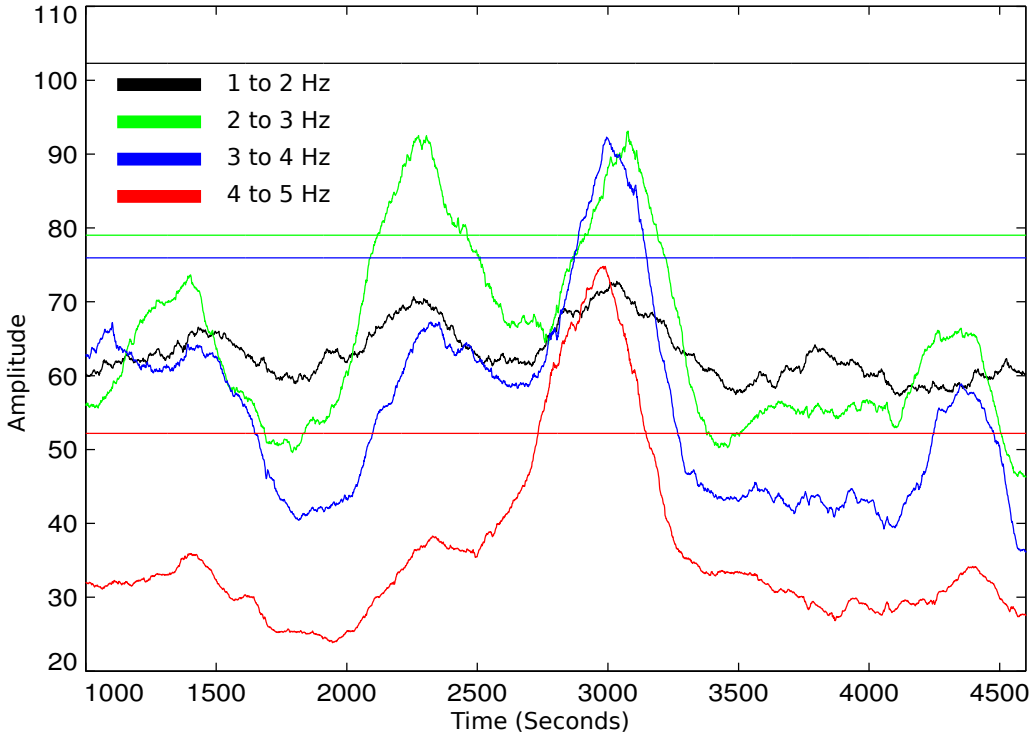


Figure 5.6: One hour period showing non-coherent tremor. The waveforms and horizontal lines have been calculated in the same manner described in Figure 5 (See legend for color explanation). There is no period when all four waveforms exceed the threshold at the same time, so no tremor is counted.

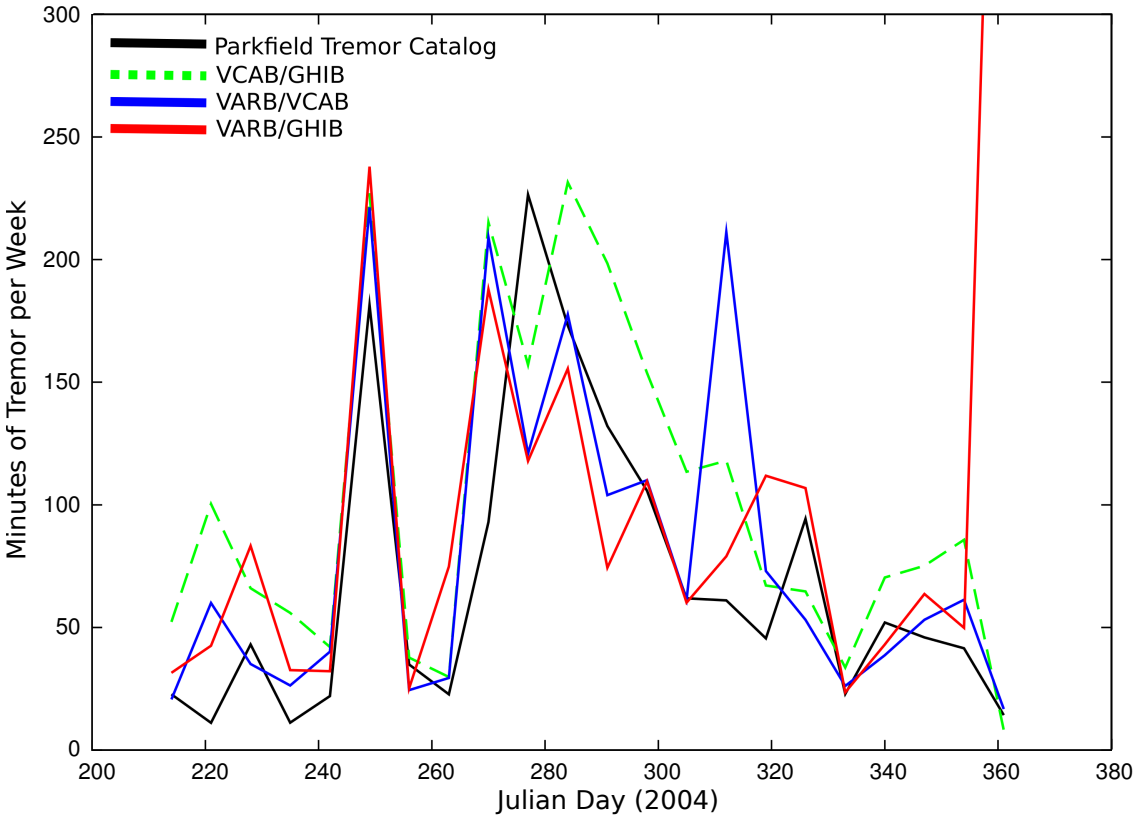


Figure 5.7: Results of our method (colored lines and dashed lines) compared to the tremor activity catalog created by Nadeau and Guilhem (2009) for Parkfield, California (black line) (see legend for station detail). Our results are consistent with the tremor activity catalog with the exception of the activity beginning on day 312 (VARB/VCAB) and the activity for the week beginning on day 361 (VARB/GHIB). The activity for the week beginning on day 312 is tremor not present in the catalog. The activity for the week beginning on day 361 is erroneous and due to zero padding an incomplete seismogram on day 365 (see text for details).

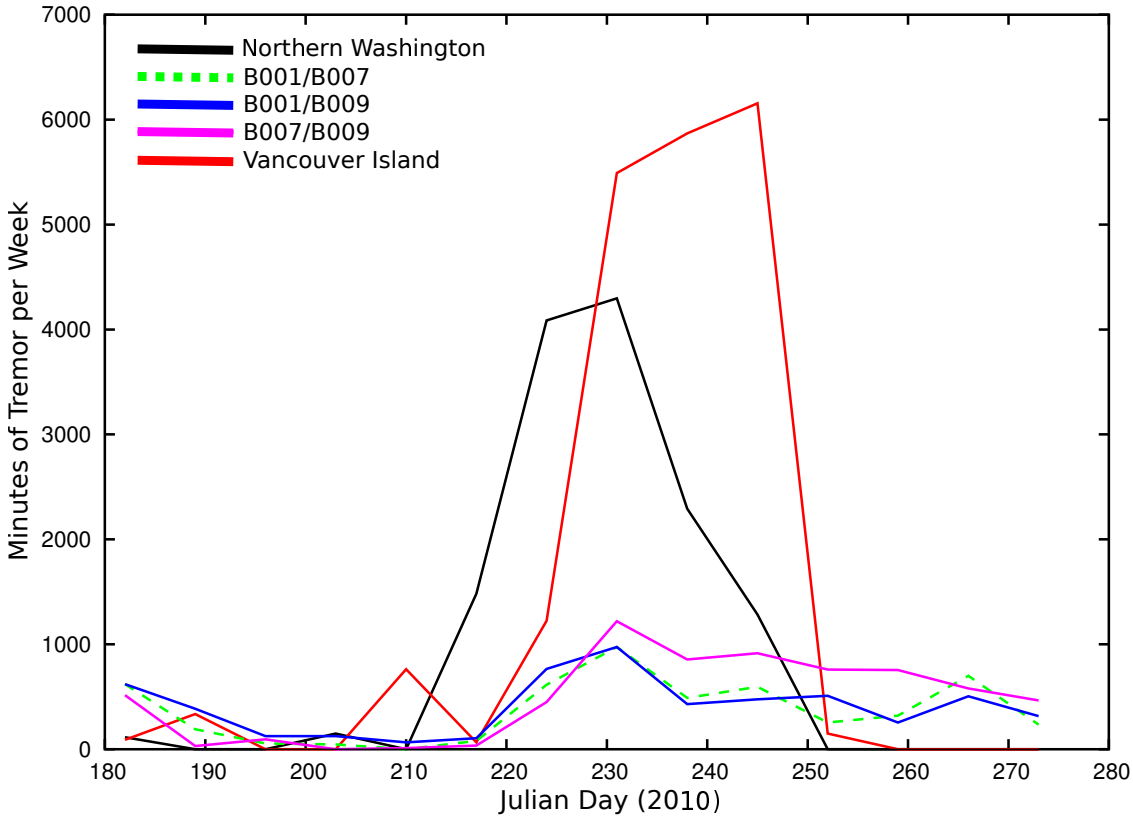


Figure 5.8: Results of our method (colored lines and dashed lines) compared to the tremor activity catalog created by Wech (2010) for the Pacific northwest (red and black lines) (see legend for station detail). Our results are consistent with the tremor catalog, although we underestimate the total amount of tremor each week. The offset in time visible between northern Washington and Vancouver Island is due to migration of tremor along the strike of the subducting slab from southeast to northwest.

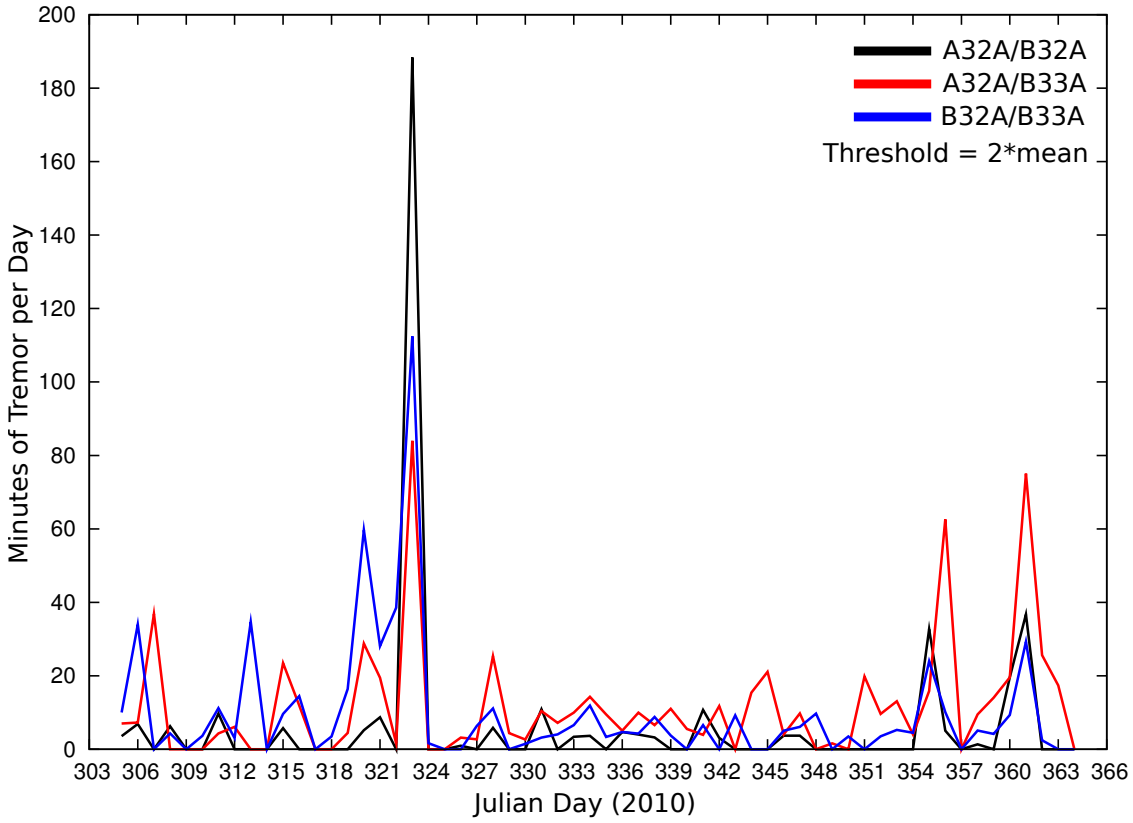


Figure 5.9: Results of the USArray analysis using a multiple of 2 for the tremor detection threshold (see legend for station detail). This region is seismically quiet and experiences no tremor. The extremely quiet background results in a low mean value which causes the tremor detection threshold (a product of the mean) to become low, resulting in false identification of tremor. Notice the amplitude scale has changed from minutes per week to minutes per day.

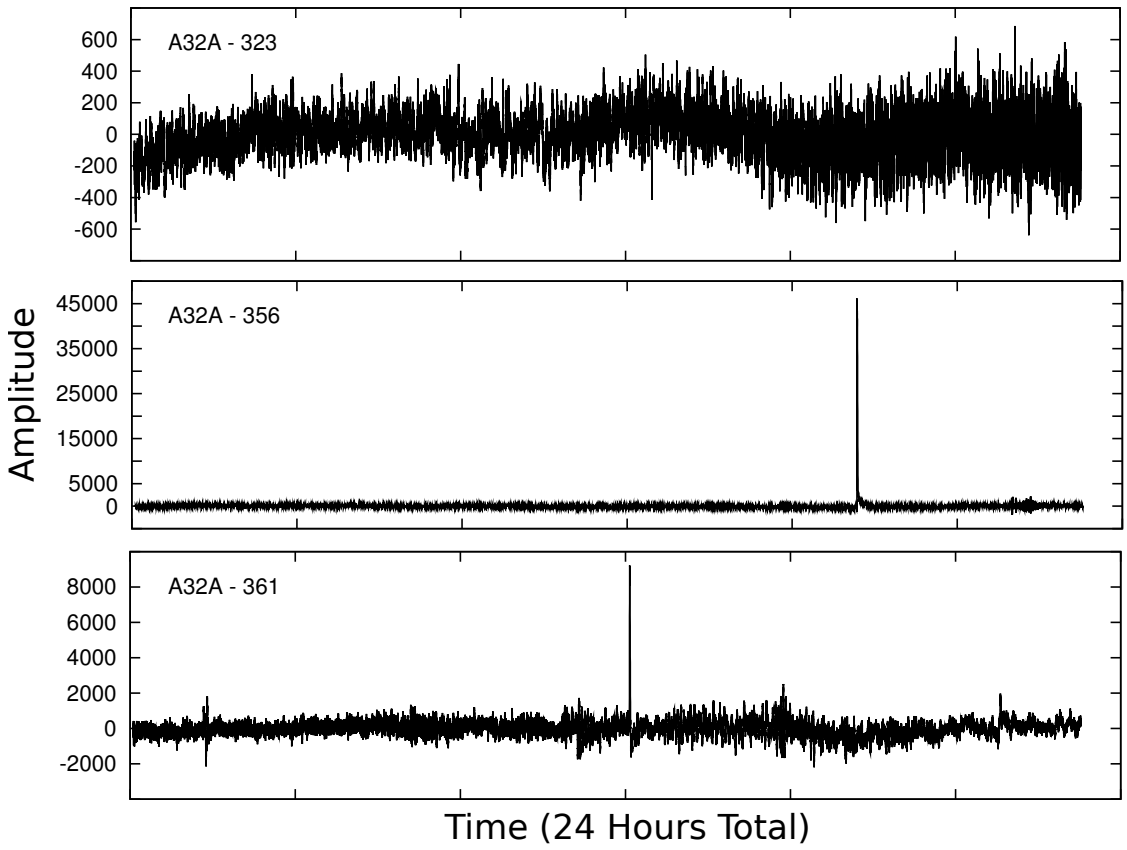


Figure 5.10: Example seismograms (24 hours in duration) for days containing falsely identified tremor (see Figure 9) using a multiple of 2 for the tremor detection threshold. These are from TA station A32A for the days 323, 356, and 361 (Julian day).

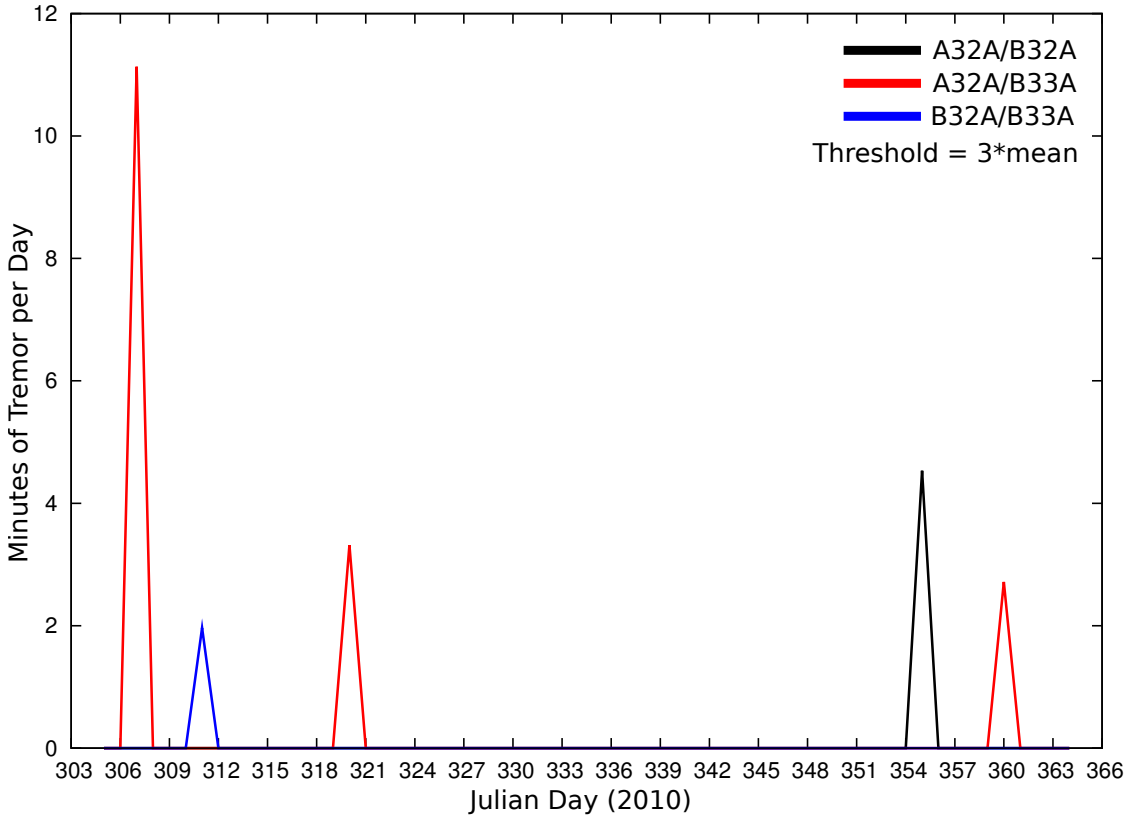


Figure 5.11: Results of the USArray analysis using a multiple of 3 for the tremor detection threshold (see legend for station detail). After increasing the increasing the tremor detection threshold the results are much better (compare to Figure 9). Although there are still some false detections, there are very few.

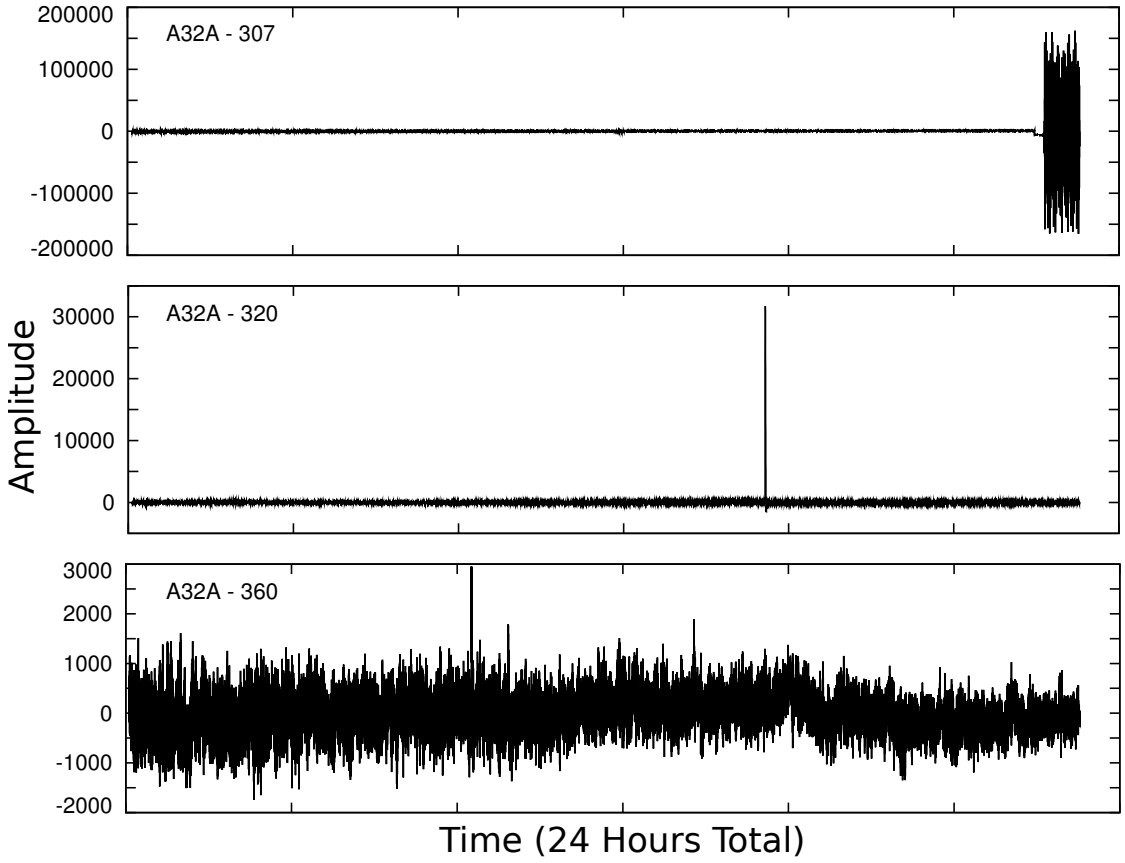


Figure 5.12: Example seismograms (24 hours in duration) for days containing falsely identified tremor (see Figure 11) using a multiple of 3 for the tremor detection threshold. These are from TA station A32A for the days 307, 320, and 360 (Julian day).

## 5.9 Tables

Table 5.1: Stations, networks, and date ranges of the continuous waveform data used in this study.

| **Region** | **Network** | **Stations** | **Date Range** |
|---|---|---|---|
| Parkfield,CA | HRSN | VARB, VCAB, GHIB | August 1, 2004–December 30, 2004 |
| Cascadia / Northern Washington | PNSN | B001, B007, B009 | July 1, 2010–October 1, 2010 |
| Midwest United States | USArray | A32A, B32A, B33A | November 1, 2010–December 31, 2010 |

# Chapter 6

# Conclusion to the thesis

The goals of this study were to gain a better understanding of the composition, temperature variability, and distributions of water and melt within the Earth's mantle. We sought to do this by examining seismic structure of the Pacific hemisphere. Our results allow us to address issues concerning the nature of the Lithosphere-Asthenosphere boundary (by mapping the depth to the Gutenberg discontinuity), melting atop the 410-km discontinuity, transition zone conditions, and the possibility of a chemical boundary layer in the mid- to lower-mantle. We sample a large portion of the mantle beneath the Pacific plate, and find mantle structure that becomes increasingly complex as we move from the central Pacific to the Japanese island arcs.

The Gutenberg discontinuity is usually more pronounced under oceans, especially beneath young ocean lithosphere. Explanations for the low velocities include partial melt, water, temperature, and grain size. Some of these suggestions do a reasonable job predicting the velocity changes that occur across the transition, however they do not explain the sharp contrast we observe at the upper boundary. We find a relatively sharp impedance contrast ($\sim$10%) at a mean depth of $\sim$90 km throughout the central Pacific, which seems to vanish in many areas near the subduction zone, and then reappear much deeper beneath the northeast China craton at a mean depth of 153 km ($\sim$4% impedance contrast).

Near subduction, we find low velocity layers in the upper mantle above the 410-km discontinuity on both sides of the subducting Honshu slab. We infer that the low-velocity layers on the backarc side of the slab are regions of partial melting, possible induced by an increase of water content in the transition zone. Subducting slabs are potential sources of water in the upper mantle and transition zone, providing a

reasonable mechanism for introducing large amounts of water on the backarc side of subduction. However, the low-velocity layers observed on the oceanward side of the Honshu slab are not consistent with this explanation. For low-velocity layers on the oceanward side of the slab it is possible that melt from other sources (i.e., plumes) is entrained by the slab and brought down to the depth we observe it. Another possibility is that slab rollback, due to trench migration, is flushing water-rich material from the transition zone. This material would melt as it crossed the 410-km discontinuity due to the lower water storage capacity of the upper mantle. Tomographic images, and P-wave velocities, suggest that melt on the oceanward side of the slab is due to a combination of increased water and temperature.

The 410-km discontinuity migrates to shallower depths in response to decreases in temperature or water, and its transition broadens. The 520-km discontinuity has the same response in terms of temperature, however increases in water content cause the 520-km discontinuity to sharpen. The 660-km discontinuity migrates to deeper depths in response to an decrease in temperature. In the open ocean mantle the mean depth to the 410-km discontinuity is 423 km, 5 km greater than the global mean. The mean depth to the 660-km discontinuity is 661 km, indistinguishable from the global mean (660 km). The 520-km discontinuity is not found in much of this region, possibly due to broadening of the transition. Additionally, we find no evidence for melting above the transition zone in the open ocean mantle. Based on these observations, we conclude that the mantle in this region is relatively dry and/or warmer.

Tomographic images of subduction zones show that slabs sometimes stall in the transition zone, accumulating at its base. In other cases the 660-km discontinuity seems to offer little resistance and the slab penetrates the transition zone, descending into the lower mantle. The western Pacific is thought to be a graveyard for fallen slabs. It has been suggested that exsolution of Ca-perovskite in stagnant slabs is responsible for the observed splitting of the 520-km discontinuity. Our observations of a split 520-km discontinuity are confined to regions of subduction, and stagnant slabs in the region are clearly seen in tomographic images. While our observations are consistent with the exsolution of Ca-perovskite, there could be other factors that contribute to the apparent splitting.

Stagnant slabs are a temporary feature, and after a period of time, they are likely to avalanche into the lower mantle. There are many observations of heterogeneity at mid-mantle depths ($\sim$750–1600 km) using a variety of seismic techniques, and our

observations add to this growing catalog. It is often suggested that these features are slab related. The obvious question is: What causes these slabs to stall at mid-mantle depths? One possible mechanism that has been suggested is the presence of a chemical boundary layer. This was first suggested on the basis of a geoid inversion that placed the layer near a depth of 920 km. Recent experimental results show that a spin transition of $Fe^{2+}$ occurring in ferropericlase could cause for a chemical boundary layer, at depths near 1200–1600 km. Numerical modeling suggests that such a layer would cause slabs to not only stall, but possible tear and/or fragment due to opposing buoyancy forces. The reflectors we observe are consistent with this, however, given the uncertainty associated with their depths and reflection coefficients, additional studies are needed before drawing any conclusions about their origin(s).

Our observations paint the picture of a relatively dry mantle beneath the open ocean, rich with upper mantle features and a distinct transition from the lithosphere to the asthenosphere. While in regions of subduction, the transition zone appears to contain more water, and the upper mantle discontinuities seem more complex. The mid-mantle in these regions contains scattered reflectors over a wide depth range that are possibly slab-related. Future studies that not only measure the sharpness of discontinuities, but also constrain their velocity changes, could help interpret the region near subduction.

The chapter on tremor was part of a separate research project, so we offer separate conclusions regarding tremor. The study of tremor has thus far been confined to regions of dense instrumentation, and due to limited resources, these are normally located along active margins (i.e., subduction zones) that are both densely populated, and in developed countries. There is a vast part of the world where fault slip occurs that we have not investigated. A method for detecting tremor that does not require a dense seismic array is a necessary first step in understanding this intriguing phenomenon. Our initial results are favorable in regions of known tremor activity. However, we discovered that in regions that are seismically quiet, the method in its current form is not as robust as it needs to be. We believe that quantitative error analysis will allow us to determine if the frequency bands we have chosen are the most appropriate, and develop a better way to set the thresholds, leading to more robust results. After completing those steps we anticipate that a global search will be possible.

# Chapter 7

# Complete Bibliography


Abers, G. A., MacKenzie, L. S., Rondenay, S., Zhang, Z., Wech, A. G., Creager, K. C., 2009. Imaging the source region of Cascadia tremor and intermediate-depth earthquakes. Geology 37 (12), 1119–1122.

Agee, C. B., Walker, D., 1993. Olivine flotation in mantle melt. Earth and Planetary Science Letters 114 (2-3), 315–324.

Akaogi, M., Ito, E., Navrotsky, A., 1989. Olivine-modified spinel-spinel transitions in the system $Mg_2SiO_4$- $Fe_2SiO_4$: Calorimetric measurements, thermochemical calculation, and geophysical application. Journal of Geophysical Research 94 (B11), 15671.

An, Y., Gu, Y. J., Sacchi, M. D., 2007. Imaging mantle discontinuities using least squares Radon transform. Journal of Geophysical Research-Solid Earth 112 (B10), B10303.

Anderson, D. L., Sammis, C., 1970. Partial melting in the upper mantle, journal=Physics of The Earth and Planetary Interiors 3, 41–50.

Angel, R. J., Chopelas, A., Ross, N. L., 1992. Stability of high-density clinoenstatite at upper-mantle pressures. Nature (London) 358 (6384), 322–324.

Antoni, J., 2006. The spectral kurtosis: a useful tool for characterising non-stationary signals. Mechanical Systems and Signal Processing 20 (2), 282–307.

Antoni, J., 2007. Fast computation of the kurtogram for the detection of transient faults. Mechanical Systems and Signal Processing 21 (1), 108–124.

Aoki, I., Takahashi, E., 2004. Density of MORB eclogite in the upper mantle; New developments in high-pressure mineral physics and applications to the Earth's interior. Physics of the Earth and Planetary Interiors 143-144, 129–143.

Audet, P., Bostock, M. G., Boyarko, D. C., Brudzinski, M. R., Allen, R. M., 2010. Slab morphology in the Cascadia fore arc and its relation to episodic tremor and slip. Journal of Geophysical Research 115, 1–15.

Audet, P., Bostock, M. G., Christensen, N. I., Peacock, S. M., 2009. Seismic evidence for overpressured subducted oceanic crust and megathrust fault sealing. Nature 457 (7225), 76–8.

Bagley, B., Courtier, A. M., Revenaugh, J., 2009. Melting in the deep upper mantle oceanward of the Honshu slab. Physics of the Earth and Planetary Interiors 175 (3-4), 137.

Bagley, B., Courtier, A. M., Revenaugh, J., In Review. Melting in the Deep Upper Mantle Oceanward of the Honshu Slab Submitted to Earth and Planetary Science Letters, February 2008.

Bagley, B., Revenaugh, J., 2008. Upper mantle seismic shear discontinuities of the Pacific. Journal of Geophysical Research 113 (B12), B12301.

Barszcz, T., Randall, R. B., 2009. Application of spectral kurtosis for detection of a tooth crack in the planetary gear of a wind turbine. Mechanical Systems and Signal Processing 23 (4), 1352–1365.

Bercovici, D., Karato, S., 2003. Whole-mantle convection and the transition-zone water filter. Nature (London) 425 (6953), 39–44.

Berryman, J. G., 2000. Seismic velocity decrement ratios for regions of partial melt in the lower mantle. Geophysical Research Letters 27 (3), 421–424.

Bijwaard, H., Spakman, W., Engdahl, E. R., 1998. Closing the gap between regional and global travel time tomography. Journal of Geophysical Research 103 (B12), 30–30,078.

Bina, C., Helffrich, G., 1994. Phase transition Clapeyron slopes and transition zone seismic discontinuity topography. Journal of Geophysical Research 99 (B8), 15,853–15,860.

Bolfan-Casanova, N., Keppler, H., Rubie, D. C., 2000. Water partitioning between nominally anhydrous minerals in the MgO-$SiO_2$-$H_2O$ system up to 24 GPa; implications for the distribution of water in the Earth's mantle. Earth and Planetary Science Letters 182 (3-4), 209–221.

Bolfan-Casanova, N., Keppler, H., Rubie, D. C., 2003. Water partitioning at 660 km depth and evidence for very low water solubility in magnesium silicate perovskite. Geophysical Research Letters 30 (17), 4.

Bolfan-Casanova, N., Kleppe, A. K., Welch, M. D., Wright, K., 2005. Water in the Earth's mantle; Protons in minerals. Mineralogical Magazine 69 (3), 229–257.

Bostock, M. G., 1996. Ps conversions from the upper mantle transition zone beneath the Canadian landmass. Journal of Geophysical Research 101 (B4), 8383–8402.

Brown, J. R., Beroza, G. C., Ide, S., Ohta, K., Shelly, D. R., Schwartz, S. Y., Rabbel, W., Thorwart, M., Kao, H., 2009. Deep low-frequency earthquakes in tremor localize to the plate interface in multiple subduction zones. Geophysical Research Letters 36 (19), 1–5.

Brudzinski, M., Allen, R., 2007. Segmentation in episodic tremor and slip all along Cascadia. Geology 35 (10), 907–910.

Cammarano, F., Goes, S., Vacher, P., Giardini, D., 2003. Inferring upper-mantle temperatures from seismic velocities. Physics of the Earth and Planetary Interiors 138 (3-4), 197–222.

Cammarano, F., Marquardt, H., Speziale, S., Tackley, P. J., 2010. Role of iron-spin transition in ferropericlase on seismic interpretation: A broad thermochemical transition in the mid mantle? Geophysical Research Letters 37 (3).

Campbell, N., Atchley, W., 1981. The geometry of canonical variate analysis. Systematic Zoology 30 (3), 268–280.

Castle, J. C., 2003. Searching for seismic scattering off mantle interfaces between 800 km and 2000 km depth. Journal of Geophysical Research 108 (B2).

Chambers, K., Deuss, A., Woodhouse, J. H., 2005. Reflectivity of the 410-km discontinuity from PP and SS precursors. Journal of Geophysical Research 110 (B2), 13.

Chapman, J. S., Melbourne, T. I., 2009. Future Cascadia megathrust rupture delineated by episodic tremor and slip. Geophysical Research Letters 36 (22), 1–5.

Chen, J., Inoue, T., Yurimoto, H., Weidner, D. J., 2002. Effect of water on olivine-wadsleyite phase boundary in the (Mg, Fe)$_2$SiO$_4$ system. Geophysical Research Letters 29 (18), 4.

Chen, L., Tao, W., Zhao, L., Zheng, T., 2008. Distinct lateral variation of lithospheric thickness in the Northeastern North China Craton. Earth and Planetary Science Letters 267 (1-2), 56.

Chevrot, S., Vinnik, L., Montagner, J.-P., 1999. Global-scale analysis of the mantle Pds phases. Journal of Geophysical Research 104 (B9), 20–20,219.

Christensen, U., 1996. The influence of trench migration on slab penetration into the lower mantle. Earth and Planetary Science Letters 140 (1-4), 27–39.

Christensen, U., 2001. Geodynamic models of deep subduction. Physics of the Earth and Planetary Interiors 127 (1-4), 25–34.

Cmiral, M., Gerald, J. D. F., Faul, U. H., Green, D. H., 1998. A close look at dihedral angles and melt geometry in olivine-basalt aggregates; a TEM study. Contributions to Mineralogy and Petrology 130 (3-4), 336–345.

Courtier, A., Revenaugh, J., 2006. A water-rich transition zone beneath the eastern United States and Gulf of Mexico from multiple ScS reverberations. Vol. 168 of Earth's Deep Water Cycle. AGU, Washington, D. C., pp. 181–193.

Courtier, A. M., Bagley, B., Revenaugh, J., 2007. Whole mantle discontinuity structure beneath Hawaii. Geophysical Research Letters 34 (17), L17304.

Courtier, A. M., Revenaugh, J., 2007. Deep upper-mantle melting beneath the Tasman and Coral Seas detected with multiple ScS reverberations. Earth and Planetary Science Letters, 259 (1-2), 66–76.

Courtier, A. M., Revenaugh, J., 2008. Slabs and shear wave reflectors in the midmantle. Journal of Geophysical Research 113 (B8).

de la Rosa, J., Moreno Muñoz, A., 2008. Higher-order cumulants and spectral kurtosis for early detection of subterranean termites. Mechanical Systems and Signal Processing 22 (2), 279–294.

Delahaye, E., Townend, J., Reyners, M., Rogers, G., 2009. Microseismicity but no tremor accompanying slow slip in the Hikurangi subduction zone, New Zealand. Earth and Planetary Science Letters 277 (1-2), 21–28.

Demouchy, S., 2005. Pressure and temperature-dependence of water solubility in Fe-free wadsleyite. American Mineralogist 90 (7), 1084.

Deuss, A., Redfern, S. A. T., Chambers, K., Woodhouse, J. H., 2006. The Nature of the 660-Kilometer Discontinuity in Earth's Mantle from Global Seismic Observations of PP Precursors. Science 311 (5758), 198–201.

Deuss, A., Woodhouse, J., 2001. Seismic observations of splitting of the mid-transition zone discontinuity in Earth's mantle. Science 294 (5541), 354–357.

Deuss, A., Woodhouse, J. H., 2002. A systematic search for mantle discontinuities using SS-precursors. Geophysical Research Letters 29 (8), 4.

Deuss, A., Woodhouse, J. H., 2004. The nature of the Lehmann discontinuity from its seismological Clapeyron slopes. Earth and Planetary Science Letters 225 (3-4), 295–304.

Dragert, G., Wang, K., James, T. S., 2001. A silent slip event on the deeper Cascadia subduction interface. Science (New York, N.Y.) 292 (5521), 1525–8.

Dwyer, R., 1983. Detection of non-gaussian signals by frequency domain kurtosis estimation. In: Acoustics, Speech, and Signal Processing, IEEE International Conference on ICASSP'83. Vol. 8. IEEE, pp. 607–610.

Dziewonski, A. M., Anderson, D. L., 1981. Preliminary reference Earth model. Physics of the Earth and Planetary Interiors 25 (4), 297–356.

Faul, U. H., Jackson, I., 2005. The seismological signature of temperature and grain size variations in the upper mantle. Earth and Planetary Science Letters 234 (1-2), 119–134.

Feng, M., van der Lee, S., An, M., Zhao, Y., 2010. Lithospheric thickness, thinning, subduction, and interaction with the asthenosphere beneath China from the joint inversion of seismic S-wave train fits and Rayleigh-wave dispersion curves. Lithos 120 (1-2), 116.

Fischer, K. M., Ford, H. A., Abt, D. L., Rychert, C. A., 2010. The Lithosphere-Asthenosphere Boundary. Annual Review of Earth and Planetary Sciences 38 (1), 551.

Fisher, R., 1936. The use of multiple measurements in taxonomic problems. Annals of Human Genetics 7 (2), 179–188.

Flanagan, M. P., Shearer, P. M., 1998. Global mapping of topography on transition zone velocity discontinuities by stacking SS precursors. Journal of Geophysical Research, B, Solid Earth and Planets 103 (2), 2673–2692.

Flanagan, M. P., Shearer, P. M., 1999. A map of topography on the 410-km discontinuity from PP precursors. Geophysical Research Letters 26 (5), 549–552.

Forte, A. M., Dziewonski, A. M., O'Connell, R. J., 1995. Thermal and chemical heterogeneity in the mantle; a seismic and geodynamic study of continental roots; Structure, composition and evolution of the Earth's interior. Physics of the Earth and Planetary Interiors 92 (1-2), 45–55.

Fry, B., Chao, K., Bannister, S., Peng, Z., 2010. Triggered non-volcanic tremor in the hikurangi subduction zone, new zealand. Abstract S23A-2109 presented at Fall Meeting, AGU, San Fransisco, Calif., 13-17 Dec., 2109.

Fujiwara, T., Hirano, N., Abe, N., Takizawa, K., 2007. Subsurface structure of the "petit-spot" volcanoes on the northwestern Pacific Plate. Geophysical Research Letters 34 (13), L13305.

Fukao, Y., Obayashi, M., Nakakuki, T., 2009. Stagnant Slab: A Review. Annual Review of Earth and Planetary Sciences 37 (1), 19.

Fukao, Y., Widiyantoro, S., Obayashi, M., 2001. Stagnant slabs in the upper and lower mantle transition region. Reviews of Geophysics 39 (3), 291–323.

Gaherty, J. B., Jordan, T. H., Gee, L. S., 1996. Seismic structure of the upper mantle in a Central Pacific corridor. Journal of Geophysical Research 101 (B10), 22–22,309.

Gaherty, J. B., Wang, Y., Jordan, T. H., Weidner, D. J., 1999. Testing plausible upper-mantle compositions using fine-scale models of the 410-km discontinuity. Geophysical Research Letters 26 (11), 1641–1644.

Ganguly, J., Frost, D. J., 2006. Stability of anhydrous phase B; experimental studies and implications for phase relations in subducting slab and the X discontinuity in the mantle. Journal of Geophysical Research 111 (B6), 8.

Gao, W., Matzel, E., Grand, S. P., 2006. Upper mantle seismic structure beneath eastern Mexico determined from P and S waveform inversion and its implications. Journal of Geophysical Research 111 (B8).

Gao, Y., Suetsugu, D., Fukao, Y., Obayashi, M., Shi, Y., Liu, R., 2010. Seismic discontinuities in the mantle transition zone and at the top of the lower mantle beneath eastern China and Korea: Influence of the stagnant Pacific slab. Physics of the Earth and Planetary Interiors 183 (1-2), 288.

Ghosh, A., Vidale, J. E., Sweet, J. R., Creager, K. C., Wech, A. G., 2009. Tremor patches in Cascadia revealed by seismic array analysis. Geophysical Research Letters 36 (17), 1–5.

Ghosh, A., Vidale, J. E., Sweet, J. R., Creager, K. C., Wech, A. G., Houston, H., 2010. Tremor bands sweep Cascadia. Geophysical Research Letters 37 (8), 1–5.

Goldstein, P., Dodge, D., Firpo, M., Miner, L., 2003. International Handbook of Earthquake and Engineering Seismology, volume 81B, chapter SAC2000: Signal processing and analysis tools for seismologists and engineers. International Association of Seismology and Physics of the Earths Interior, 1613–1614.

Goldstein, P., Snoke, A., 2005. Sac availability for the iris community. Incorporated Research Institutions for Seismology Newsletter 7 (UCRL-JRNL-211140).

Gomberg, J., 2010. Slow-slip phenomena in Cascadia from 2007 and beyond: A review. Geological Society of America Bulletin 122 (7-8), 963–978.

Gomberg, J., Rubinstein, J. L., Peng, Z., Creager, K. C., Vidale, J. E., Bodin, P., 2008. Widespread triggering of nonvolcanic tremor in California. Science (New York, N.Y.) 319 (5860), 173.

Gorbatov, A., Kennett, B., 2003. Joint bulk-sound and shear tomography for Western Pacific subduction zones. Earth and Planetary Science Letters 210 (3-4), 527.

Gossler, J., Kind, R., 1996. Seismic evidence for very deep roots of continents. Earth and Planetary Science Letters, 138 (1-4), 1–13.

Graves, R. W., Helmberger, D. V., 1988. Upper mantle cross section from Tonga to Newfoundland. Journal of Geophysical Research 93 (B5), 4701–4711.

Gu, Y., Dziewonski, A. M., Agee, C. B., 1998. Global de-correlation of the topography of transition zone discontinuities. Earth and Planetary Science Letters, 157 (1-2), 57–67.

Gu, Y. J., Dziewonski, A. M., 2002. Global variability of transition zone thickness. Journal of Geophysical Research 107 (B7), 17.

Gu, Y. J., Dziewonski, A. M., Ekstrom, G., 2001. Preferential detection of the Lehmann discontinuity beneath continents. Geophysical Research Letters 28 (24), 4655–4658.

Gudmundsson, Ó., Sambridge, M., 1998. A regionalized upper mantle (RUM) seismic model. Journal of Geophysical Research 103 (B4), 7121.

Gung, Y., Panning, M., Romanowicz, B., 2003. Global anisotropy and the thickness of continents. Nature (London) 422 (6933), 707–711.

Gutenberg, B., 1959. Wave velocities below the Mohorovicic discontinuity. Geophys.J., London 2 (4), 348–352.

Hales, A., 1969. A seismic discontinuity in the lithosphere. Earth and Planetary Science Letters 7 (1), 44.

Helffrich, G., 2000. Topography of the transition zone seismic discontinuities. Reviews of Geophysics 38 (1), 141–158.

Helffrich, G. R., Wood, B. J., 1996. 410 km Discontinuity Sharpness and the Form of the Olivine Alpha-Beta Phase Diagram; Resolution of Apparent Seismic Contradictions. Geophysical Journal International 126 (2), F7–F12.

Hier-Majumder, S., Ricard, Y., Bercovici, D., 2006. Role of grain boundaries in magma migration and storage. Earth and Planetary Science Letters 248 (3-4), 735–749.

Higo, Y., Inoue, T., Irifune, T., Yurimoto, H., 2001. Effect of water on the spinel-postspinel transformation in $Mg_2SiO_4$. Geophysical Research Letters 28 (18), 3505–3508.

Hirano, N., Kawamura, K., Hattori, M., Saito, K., Ogawa, Y., 2001. A new type of intra-plate volcanism; young alkali-basalts discovered from the subducting Pacific Plate, northern Japan Trench. Geophysical Research Letters 28 (14), 2719–2722.

Hirschmann, M. M., 2006. Water, melting, and the deep Earth $H_2O$ cycle. Annual Review of Earth and Planetary Sciences 34, 629–653.

Hirschmann, M. M., Aubaud, C., Withers, A. C., 2005. Storage capacity of $H_2O$ in nominally anhydrous minerals in the upper mantle. Earth and Planetary Science Letters 236 (1-2), 167–181.

Hirschmann, M. M., Withers, A. C., Aubaud, C., 2006. Petrologic structure of a hydrous 410 km discontinuity; Earth's deep water cycle. Geophysical Monograph 168, 277–287.

Honda, S., Morishige, M., Orihashi, Y., 2007. Sinking hot anomaly trapped at the 410km discontinuity near the Honshu subduction zone, Japan. Earth and Planetary Science Letters, 261 (3-4), 565–577.

Hyndman, R., Wang, K., 1993. Thermal constraints on the zone of major thrust earthquake failure: The cascadia subduction zone. Journal of Geophysical Research 98 (B2), 2039–2060.

Hyndman, R., Wang, K., 1995. The rupture zone of cascadia great earthquakes from current deformation and the thermal regime. Journal of Geophysical Research 100 (B11), 22133–22.

Ide, S., Shelly, D. R., Beroza, G. C., 2007. Mechanism of deep low frequency earthquakes: Further evidence that deep non-volcanic tremor is generated by shear slip on the plate interface. Geophysical Research Letters 34 (3).

Inoue, T., Weidner, D. J., Northrup, P. A., Parise, J. B., 1998. Elastic properties of hydrous ringwoodite ($\gamma$-phase) in $Mg_2SiO_4$. Earth and Planetary Science Letters 160 (1-2), 107.

Ita, J., Stixrude, L., 1992. Petrology, elasticity, and composition of the mantle transition zone. Journal of Geophysical Research 97 (B5), 6849–6866.

Jacobsen, S. D., Smyth, J. R., 2006. Effect of water on the sound velocities of ringwoodite in the transition zone; Earth's deep water cycle. Geophysical Monograph 168, 131–145.

Jacobsen, S. D., Smyth, J. R., Spetzler, H., Holl, C. M., Frost, D. J., 2004. Sound velocities and elastic constants of iron-bearing hydrous ringwoodite. Physics of The Earth and Planetary Interiors, 143-144, 47–56.

Jasbinsek, J., Dueker, K., 2007. Ubiquitous low-velocity layer atop the 410-km discontinuity in the northern Rocky Mountains. Geochemistry Geophysics Geosystems 8, Q10004.

Jordan, T. H., 1979. The Deep Structure of the Continents. Scientific American 240, 92–107.

Julian, B., 2002. Seismological detection of slab metamorphism. Science 296 (5573), 1625.

Kaneshima, S., 2003. Subparallel dipping heterogeneities in the mid-lower mantle. Journal of Geophysical Research 108 (B5).

Kao, H., Philip, J., Rogers, G., Dragert, H., Spence, G., 2007. Automatic detection and characterization of seismic tremors in northern Cascadia. Geophysical Research Letters 34 (16), 1–6.

Kao, H., Shan, S., Dragert, H., Rogers, G., 2009. Northern Cascadia episodic tremor and slip: A decade of tremor observations from 1997 to 2007. Journal of Geophysical Research 114, 1–20.

Kao, H., Shan, S., Dragert, H., Rogers, G., Cassidy, J., Ramachandran, K., 2005. A wide depth distribution of seismic tremors along the northern Cascadia margin. Nature 436 (7052), 841–4.

Kao, H., Thompson, P., Shan, S., Rogers, G., Dragert, H., Spence, G., 2008. Tremor Activity Monitoring System (TAMS) Operating in Northern Cascadia. Eos Trans. AGU 89 (42), 405–406.

Kárason, H., van der Hilst, R., 2000. Constraints on mantle convection from seismic tomography. Vol. 121 of Geophysical Monograph, The History and Dynamics of Global Plate Motions. American Geophysical Union, Washington, DC.

Karato, S., Bercovici, D., Leahy, G., Richard, G., Jing, Z., 2006. The transition-zone water filter model for global material circulation; where do we stand?; Earth's deep water cycle. Geophysical Monograph 168, 289–313.

Karato, S., Jung, H., 1998. Water, partial melting and the origin of the seismic low velocity and high attenuation zone in the upper mantle. Earth and Planetary Science Letters 157 (3-4), 193–207.

Katayama, I., Nakashima, S., 2003. Hydroxyl in clinopyroxene from the deep subducted crust; evidence for $H_2O$ transport into the mantle. American Mineralogist 88 (1), 229–234.

Katsumata, M., Sykes, L. R., 1969. Seismicity and Tectonics of the Western Pacific: Izu-Mariana-Caroline and Ryukyu-Taiwan Regions. Journal of Geophysical Research 74 (25), 5923.

Katsura, T., Ito, E., 1989. The System $Mg_2SiO_4$-$Fe_2SiO_4$ at High Pressures and Temperatures: Precise Determination of Stabilities of Olivine, Modified Spinel, and Spinel. Journal of Geophysical Research 94 (B11), 15663.

Katsura, T., Yamada, H., Nishikawa, O., Song, M., Kubo, A., Shinmei, T., Yokoshi, S., Aizawa, Y., Yoshino, T., Walter, M. J., Ito, E., ichi Funakoshi, K., 2004a. Olivine-wadsleyite transition in the system $(Mg,Fe)_2SiO_4$. Journal of Geophysical Research 109 (B2), 12.

Katsura, T., Yamada, H., Shinmei, T., Kubo, A., Ono, S., Kanzaki, M., Yoneda, A., Walter, M. J., Ito, E., Urakawa, S., Funakoshi, K., Utsumi, W., 2003. Post-spinel transition in $Mg_2SiO_4$ determined by high P-T in situ X-ray diffractometry; Phase transitions and mantle discontinuities. Physics of the Earth and Planetary Interiors 136 (1-2), 11–24.

Katsura, T., Yokoshi, S., Song, M., Kawabe, K., Tsujimura, T., Kubo, A., Ito, E., Tange, Y., Tomioka, N., Saito, K., Nozawa, A., ichi Funakoshi, K., 2004b. Thermal expansion of $Mg_2SiO_4$ ringwoodite at high pressure. Journal of Geophysical Research 109 (B12), 10.

Katzman, R., Li, Z., Jordan, T. H., 1998. High-resolution, two-dimensional vertical tomography of the Central Pacific mantle using ScS reverberations and frequency-dependent travel times. Journal of Geophysical Research 103 (B8), 17–17,971.

Kawakatsu, H., Niu, F., 1994. Seismic evidence for a 920-km discontinuity in the mantle. Nature 371 (6495), 301.

Kodaira, S., Iidaka, T., Kato, A., Park, J., Iwasaki, T., Kaneda, Y., 2004. High pore fluid pressure may cause silent slip in the nankai trough. Science 304 (5675), 1295.

Kohlstedt, D. L., Keppler, H., Rubie, D. C., 1996. Solubility of water in the alpha , beta and gamma phases of $(Mg,Fe)_2SiO_4$. Contributions to Mineralogy and Petrology 123 (4), 345–357.

Krüger, F., Baumann, M., Scherbaum, F., Weber, M., 2001. Mid mantle scatterers near the Mariana Slab detected with a double array method. Geophysical Research Letters 28 (4), 667.

Kumar, P., Kawakatsu, H., 2011. Imaging the seismic lithosphere-asthenosphere boundary of the oceanic plate. Geochemistry Geophysics Geosystems 12 (1).

Lambert, A., Kao, H., Rogers, G., Courtier, N., 2009. Correlation of tremor activity with tidal stress in the northern Cascadia subduction zone. Journal of Geophysical Research 114, 1–10.

Lawrence, J. F., Shearer, P. M., 2006. A global study of transition zone thickness using receiver functions. Journal of Geophysical Research 111 (B6), 10.

Leahy, G., Bercovici, D., 2007. On the dynamics of a hydrous melt layer above the transition zone. J. Geophys. Res 112.

Lerner-Lam, A. L., Jordan, T. H., 1987. How thick are the continents? Journal of Geophysical Research 92 (B13), 14–14,026.

Levin, V., 2000. Shear zones in the Proterozoic lithosphere of the Arabian Shield and the nature of the Hales discontinuity. Tectonophysics 323 (3-4), 131.

Li, A., Fischer, K. M., Wysession, M. E., Clarke, T. J., 1998. Mantle discontinuities and temperature under the North American continental keel. Nature 395 (6698), 160–163.

Litasov, K., Ohtani, E., Kagi, H., Jacobsen, S., Ghosh, S., 2007. Temperature dependence and mechanism of hydrogen incorporation in olivine at 12.5–14.0 GPa. Geophysical Research Letters 34 (16), L16314.

Liu, Y., Rice, J. R., 2007. Spontaneous and triggered aseismic deformation transients in a subduction fault model. Journal of Geophysical Research 112 (B9), 1–23.

Maceira, M., Rowe, C., Beroza, G., Anderson, D., 2010. Identification of low-frequency earthquakes in non-volcanic tremor using the subspace detector method. Geophysical Research Letters 37 (6), L06303.

Maeda, T., Obara, K., 2009. Spatiotemporal distribution of seismic energy radiation from low-frequency tremor in western Shikoku, Japan. Journal of Geophysical Research 114.

Mao, Z., Jacobsen, S. D., Jiang, F., Smyth, J. R., Holl, C. M., Frost, D. J., Duffy, T. S., 2008. Single-crystal elasticity of wadsleyites, (beta)-$Mg_2SiO_4$, containing 0.37-1.66 wt.% $H_2O$. Earth and Planetary Science Letters 266, 78–89.

Matsubara, M., Obara, K., Kasahara, K., 2009. High-VP/VS zone accompanying non-volcanic tremors and slow-slip events beneath southwestern Japan. Tectonophysics 472 (1-4), 6–17.

Matsukage, K. N., Jing, Z., ichiro Karato, S., 2005. Density of hydrous silicate melt at the conditions of Earth's deep upper mantle. Nature (London) 438 (7067), 488–491.

Morra, G., Yuen, D., Boschi, L., Chatelain, P., Koumoutsakos, P., Tackley, P., 2010. The fate of the slabs interacting with a density/viscosity hill in the mid-mantle. Physics of the Earth and Planetary Interiors 180 (3-4), 271.

Morris, P. A., 1995. Slab melting as an explanation of Quaternary volcanism and aseismicity in southwest Japan. Geology 23 (5), 395.

Müller, R. D., Sdrolias, M., Gaina, C., Roest, W. R., 2008. Age, spreading rates, and spreading asymmetry of the world's ocean crust. Geochemistry Geophysics Geosystems 9 (4).

Murakami, M., Hirose, K., Yurimoto, H., Nakashima, S., Takafuji, N., 2002. Water in Earth's lower mantle. Science 295 (5561), 1885–1887.

Nadeau, R., Guilhem, A., 2009. Nonvolcanic tremor evolution and the San Simeon and Parkfield, California, earthquakes. Science 325 (5937), 191.

Nadeau, R. M., Dolenc, D., 2005. Nonvolcanic Tremors Deep Beneath the San Andreas Fault. Science (January), 94720–94720.

Nakajima, J., Hasegawa, A., 2007. Tomographic evidence for the mantle upwelling beneath southwestern Japan and its implications for arc magmatism. Earth and Planetary Science Letters 254 (1-2), 90.

Nakata, R., Suda, N., Tsuruoka, H., 2008. Non-volcanic tremor resulting from the combined effect of Earth tides and slow slip events. Nature Geoscience 1 (10), 676–678.

Nishimura, C. E., Forsyth, D. W., 1989. The anisotropic structure of the upper mantle in the Pacific. Geophysical Journal International 96 (2), 203–229.

Niu, F., 2003. Seismic evidence for a chemical heterogeneity in the midmantle: A strong and slightly dipping seismic reflector beneath the Mariana subduction zone. Journal of Geophysical Research 108 (B9).

Niu, F., Kawakatsu, H., 1997. Depth variation of the mid-mantle seismic discontinuity. Geophysical Research Letters 24 (4), 429.

Niu, F., Levander, A., Ham, S., Obayashi, M., 2005. Mapping the subducting Pacific slab beneath southwest Japan with Hi-net receiver functions. Earth and Planetary Science Letters 239 (1-2), 9–17.

Nolet, G., Zielhuis, A., 1994. Low S velocities under the Tornquist-Teisseyre zone; evidence for water injection into the transition zone by subduction. Journal of Geophysical Research 99 (B8), 15–15,820.

Obara, K., 2002. Nonvolcanic deep tremor associated with subduction in southwest japan. Science 296 (5573), 1679.

Obara, K., Hirose, H., 2006. Non-volcanic deep low-frequency tremors accompanying slow slips in the southwest Japan subduction zone. Earth Science 417, 33 – 51.

Obayashi, M., Sugioka, H., Yoshimitsu, J., Fukao, Y., 2006. High temperature anomalies oceanward of subducting slabs at the 410-km discontinuity. Earth and Planetary Science Letters 243 (1-2), 149–158.

Ohtani, E., Nagata, Y., Suzuki, A., Kato, T., 1995. Melting relations of peridotite and the density crossover in planetary mantles; Chemical evolution of the mantle. Chemical Geology 120 (3-4), 207–221.

Olbertz, D., Wortel, M., Hansen, U., 1997. Trench migration and subduction zone geometry. Geophysical Research Letters 24 (3), 221–224.

Payero, J., Kostoglodov, V., Shapiro, N., Mikumo, T., Iglesias, A., Pérez-Campos, X., Clayton, R., 2008. Nonvolcanic tremor observed in the Mexican subduction zone. Geophysical Research Letters 35 (7), 1–6.

Peacock, S. M., 1999. Seismic Consequences of Warm Versus Cool Subduction Metamorphism: Examples from Southwest and Northeast Japan. Science 286 (5441), 937.

Peng, Z., Vidale, J., Creager, K., Rubinstein, J., Gomberg, J., Bodin, P., 2008. Strong tremor near Parkfield, CA, excited by the 2002 Denali Fault earthquake. Geophysical Research Letters 35 (23), 1–5.

Peterson, C., Christensen, D., 2009. Possible relationship between nonvolcanic tremor and the 1998–2001 slow slip event, south central Alaska. Journal of Geophysical Research 114 (B6), 1–13.

Pino, N. A., Helmberger, D. V., 1997. Upper mantle compressional velocity structure beneath the West Mediterranean Basin. Journal of Geophysical Research, B, Solid Earth and Planets 102 (2), 2953–2967.

Revenaugh, J., Jordan, T. H., 1989. A study of mantle layering beneath the western Pacific. Journal of Geophysical Research 94 (B5), 5787–5813.

Revenaugh, J., Jordan, T. H., 1991a. Mantle layering from ScS reverberations; 1, Waveform inversion of zeroth-order reverberations. Journal of Geophysical Research, Solid Earth and Planets 96 (B12), 19,749–19,762.

Revenaugh, J., Jordan, T. H., 1991b. Mantle layering from ScS reverberations; 2, The transition zone. Journal of Geophysical Research, Solid Earth and Planets 96 (B12), 19,763–19,780.

Revenaugh, J., Jordan, T. H., 1991c. Mantle layering from ScS reverberations; 3, The upper mantle. Journal of Geophysical Research, Solid Earth and Planets 96 (B12), 19,781–19,810.

Revenaugh, J., Jordan, T. H., 1991d. Mantle Layering From ScS Reverberations; 4, The Lower Mantle and Core-Mantle Boundary. Journal of Geophysical Research, Solid Earth and Planets 96 (B12), 19811.

Revenaugh, J., Sipkin, S. A., 1994. Mantle discontinuity structure beneath China. Journal of Geophysical Research 99 (B11), 21911.

Revenaugh, J., Sipkin, S. A., 1994. Seismic evidence for silicate melt atop the 410-km mantle discontinuity. Nature (London) 369 (6480), 474–476.

Richard, G., Monnereau, M., Rabinowicz, M., 2007. Slab dehydration and fluid migration at the base of the upper mantle; implications for deep earthquake mechanisms. Geophysical Journal International 168 (3), 1291–1304.

Ringwood, A. E., 1975. Composition and petrology of the Earth's mantle. McGraw-Hill Book Co., New York, N.Y., United States (USA), United States (USA).

Rogers, G., Dragert, H., 2003. Episodic tremor and slip on the Cascadia subduction zone: the chatter of silent slip. Science (New York, N.Y.) 300 (5627), 1942–1943.

Rubinstein, J. L., La Rocca, M., Vidale, J. E., Creager, K. C., Wech, A. G., 2008. Tidal modulation of nonvolcanic tremor. Science (New York, N.Y.) 319 (5860), 186–189.

Rubinstein, J. L., Vidale, J. E., Gomberg, J., Bodin, P., Creager, K. C., Malone, S. D., 2007. Non-volcanic tremor driven by large transient shear stresses. Nature 448 (August), 579–582.

Rychert, C. A., Shearer, P. M., 2009. A global view of the lithosphere-asthenosphere boundary. Science 324 (5926), 495–8.

Rychert, C. A., Shearer, P. M., Fischer, K. M., 2010. Scattered wave imaging of the lithosphere–asthenosphere boundary. Lithos 120 (1-2), 173.

Saikia, A., Frost, D. J., Rubie, D. C., 2008. Splitting of the 520-kilometer seismic discontinuity and chemical heterogeneity in the mantle. Science 319 (5869), 1515–8.

Sakamaki, T., Suzuki, A., Ohtani, E., 2006. Stability of hydrous melt at the base of the Earth's upper mantle. Nature 439 (7073), 192–194.

Schmerr, N., Garnero, E., 2006. Investigation of upper mantle discontinuity structure beneath the Central Pacific using SS precursors. Journal of Geophysical Research 111 (B8).

Schmid, C., Goes, S., van der Lee, S., Giardini, D., 2002. Fate of the Cenozoic Farallon slab from a comparison of kinematic thermal modeling with tomographic images. Earth and Planetary Science Letters 204 (1-2), 17.

Schwartz, S., Rokosky, J., 2007. Slow slip events and seismic tremor at circum-Pacific subduction zones. Rev. Geophys 45 (3).

Seno, T., Takano, T., 1989. Seismotectonics at the Trench-Trench-Trench triple junction off central Honshu. Pure and Applied Geophysics PAGEOPH 129 (1-2), 27.

Shearer, P. M., 1990. Seismic imaging of upper-mantle structure with new evidence for a 520-km discontinuity. Nature 344 (6262), 121.

Shearer, P. M., 1991. Constraints on upper mantle discontinuities from observations of long-period reflected and converted phases. Journal of Geophysical Research 96 (B11), 18–18,182.

Shearer, P. M., 1996. Transition zone velocity gradients and the 520-km discontinuity. Journal of Geophysical Research 101 (B2), 3053–3066.

Shearer, P. M., Masters, T. G., 1992. Global mapping of topography on the 660-km discontinuity. Nature 355 (6363), 791.

Shelly, D., 2009. Possible deep fault slip preceding the 2004 Parkfield earthquake, inferred from detailed observations of tectonic tremor. Geophysical Research Letters 36 (17), 1–6.

Shelly, D., 2010. Periodic, chaotic, and doubled earthquake recurrence intervals on the deep San Andreas fault. Science (New York, N.Y.) 328 (5984), 1385–1388.

Shelly, D., Beroza, G. C., Ide, S., 2007a. Complex evolution of transient slip derived from precise tremor locations in western Shikoku, Japan. Geochemistry Geophysics Geosystems 8 (10).

Shelly, D., Beroza, G. C., Ide, S., 2007b. Non-volcanic tremor and low-frequency earthquake swarms. Nature 446 (7133), 305–307.

Shelly, D., Beroza, G. C., Ide, S., Nakamula, S., 2006. Low-frequency earthquakes in Shikoku, Japan, and their relationship to episodic tremor and slip. Nature (London) 442 (7099), 188–191.

Shen, Y., 2003. Seismic evidence for accumulated oceanic crust above the 660-km discontinuity beneath southern Africa. Geophysical Research Letters 30 (18).

Shieh, S. R., Mao, H.-K., Hemley, R. J., Ming, L. C., 1998. Decomposition of phase D in the lower mantle and the fate of dense hydrous silicates in subducting slabs. Earth and Planetary Science Letters 159 (1-2), 13–23.

Smyth, J., Frost, D., Nestola, F., Holl, C., Bromiley, G., 2006. Olivine hydration in the deep upper mantle: Effects of temperature and silica activity. Geophys. Res. Lett 33, 12–5.

Smyth, J. R., Frost, D., 2002. The effect of water on the 410-km discontinuity; an experimental study. Geophysical Research Letters 29 (10), 4.

Song, T.-R. A., Helmberger, D. V., Brudzinski, M. R., Clayton, R. W., Davis, P., Pérez-Campos, X., Singh, S. K., 2009. Subducting slab ultra-slow velocity layer coincident with silent earthquakes in southern Mexico. Science 324 (5926), 502–6.

Song, T. R. A., Helmberger, D. V., Grand, S. P., 2004. Low-velocity zone atop the 410-km seismic discontinuity in the northwestern United States. Nature 427 (6974), 530–533.

Stixrude, L., Lithgow-Bertelloni, C., 2005. Mineralogy and elasticity of the oceanic upper mantle; origin of the low-velocity zone. Journal of Geophysical Research 110 (B3), 16.

Suda, N., Nakata, R., Kusumi, T., 2009. An automatic monitoring system for non-volcanic tremors in southwest Japan. Journal of Geophysical Research 114 (B), 1–15.

Thomas, A. M., Nadeau, R. M., Bu, R., 2009. Tremor-tide correlations and near-lithostatic pore pressure on the deep San Andreas fault. Nature 462 (December), 1048–1052.

Thybo, H., Perchuc, E., 1997. The seismic 8 degrees discontinuity and partial melting in continental mantle. Science 275 (5306), 1626–1629.

van der Hilst, R. D., Engdahl, R., Spakman, W., Nolet, G., 1991. Tomographic imaging of subducted lithosphere below Northwest Pacific island arcs. Nature (London) 353 (6339), 37–43.

van der Lee, S., Nolet, G., 1997. Upper mantle velocity S structure of North America. Journal of Geophysical Research 102 (B10), 22,815–22838.

van der Meijde, M., van der Lee, S., Giardini, D., 2005. Seismic discontinuities in the Mediterranean mantle. Physics of the Earth and Planetary Interiors 148 (2-4), 233–250.

Vanacore, E., Niu, F., Kawakatsu, H., 2006. Observations of the mid-mantle discontinuity beneath Indonesia from S to P converted waveforms. Geophysical Research Letters 33 (4).

Vinnik, L., 2002. Subcratonic low-velocity layer and flood basalts. Geophysical Research Letters 29 (4).

Vinnik, L., 2003. Super-deep low-velocity layer beneath the Arabian plate. Geophysical Research Letters 30 (7).

Vinnik, L., Farra, V., 2007. Low S velocity atop the 410-km discontinuity and mantle plumes. Earth and Planetary Science Letters 262 (3-4), 398–412.

Walsh, J., 1969. New analysis of attenuation in partially melted rock. Journal of Geophysical Research 74 (17), 4333–4337.

Wang, J., Sinogeikin, S., Inoue, T., Bass, J. D., 2003. Elastic properties of hydrous ringwoodite. American Mineralogist 88 (10), 1608–1611.

Wech, A., 2010. Interactive Tremor Monitoring. Seismological Research Letters 81 (4), 664–669.

Wech, A., Creager, K., 2008. Automated detection and location of Cascadia tremor. Geophys. Res. Lett 35, 1–5.

Wech, A., Creager, K., Melbourne, T., 2009. Seismic and geodetic constraints on cascadia slow slip. Journal of Geophysical Research 114 (B10), 1–9.

Wen, L., Anderson, D., 1997. Layered mantle convection: A model for geoid and topography. Earth and Planetary Science Letters 146 (3-4), 367.

Wessel, P., Smith, W. H. F., 1998. New, improved version of generic mapping tools released. Eos, Transactions American Geophysical Union 79 (47), 579.

Williams, Q., Revenaugh, J., 2005. Ancient subduction, mantle eclogite, and the 300 km seismic discontinuity. Geology (Boulder) 33 (1), 1–4.

Wittlinger, G., Farra, V., 2007. Converted waves reveal a thick and layered tectosphere beneath the Kalahari super-craton. Earth and Planetary Science Letters 254 (3-4), 404.

Wood, B. J., 1995. The effect of $H_2O$ on the 410-kilometer seismic discontinuity. Science 268 (5207), 74–76.

Woodland, A. B., 1998. The orthohombic to high-P monoclinic phase transition in Mg-Fe pyroxenes; can it produce a seismic discontinuity? Geophysical Research Letters 25 (8), 1241–1244.

Workman, R., Hart, S., 2005. Major and trace element composition of the depleted MORB mantle (DMM). Earth and Planetary Science Letters 231 (1-2), 53–72.

Xuzhang, S., Zhou, H., Kawakatsu, H., 2008. Mapping the upper mantle discontinuities beneath China with teleseismic receiver functions. Earth Planets Space 60 (7), 713–719.

Yoshii, T., 1979. A detailed cross-section of the deep seismic zone beneath northeastern Honshu, Japan. Tectonophysics 55 (3-4), 349.

Yoshino, T., Nishihara, Y., Karato, S., 2007. Complete wetting of olivine grain boundaries by a hydrous melt near the mantle transition zone. Earth and Planetary Science Letters, 256 (3-4), 466–472.

Zang, S., Zhou, Y., Jiang, Z., 2003. Mantle Discontinuities Beneath Izu-Bonin and the Implications. Science in China (Series D) 46 (12), 1201–1211.

Zang, S. X., Chen, Q. Y., Ning, J. Y., Shen, Z. K., Liu, Y. G., 2002. Motion of the Philippine Sea plate consistent with the NUVEL-1A model. Geophysical Journal International 150 (3), 809.

Zhang, J., Herzberg, C., 1994. Melting experiments on anhydrous peridotite KLB-1 from 5.0 to 22.5 GPa. Journal of Geophysical Research 99 (B9), 17–17,742.

Zhang, Z., Lay, T., 1993. Investigation of upper mantle discontinuities near northwestern Pacific subduction zones using precursors to sSH. Journal of Geophysical Research 98 (B3), 4389–4405.

Zhao, D., 2004. Global tomographic images of mantle plumes and subducting slabs: insight into deep Earth dynamics. Physics of The Earth and Planetary Interiors, 146 (1-2), 3–34.

# Appendix A

This appendix contains the codes used for tremor analysis. The first program, detect.m, is used to analyze the seismic traces for possible tremor. The second program, compareFiles.m, compares the results from two stations to check for coherency. Additionally, it creates files (used for plotting) that list tremor activity in seconds, minutes, and hours per day. There is a flag (M) that is used to define how the tremor is summed. If M is set to 1, tremor is counted second by second. If M is set to 5, tremor is counted by 5 minute windows which is more comparable to how tremor is counted in Cascadia. The third program, plot_week.m, is used to convert the daily results from comparFiles.m to weekly values used for plotting (if necessary). Plotting is easily accomplished by using Gnuplot.

## detect.m

```
% Non-volcanic tremor detection code
% Brian Bagley
% University of Minnesota
% May 2011

% INPUT: 20 Hz seismogram 1 day long
% OUTPUT: Array of possible tremor - 1 file for each station
% Multiple stations can be compared using compareFiles.m
% REQUIRED FUNCTIONS: rms.m

% ##########     VARIABLE DEFINITIONS     ##########
% A         Butterworth filter coefficient (denominator)
% B         Butterworth filter coefficient (numerator)
% bp        Counter for bandpass filter
% fid       File name to save array for compareFiles.m - trem_pos_array.txt
% fid2      File name to save diag results - trem_pos.txt
```

```
% fn        Filename of data file to be analyzed
% hour      Hour
% j         Temporary index for duration check
% k         Array index
% min       Minute
% m         Mean of window
% n         Size of envelop array (i.e. data / 20), currently 86400
% Pos       4 X n matrix to store 'possible' tremor detections
% PosSum    Sum of Pos, this is 1 X n with largest possible value of 4
% r         Counter (actually the same value as bp)
% s         Seconds (range = 0 to 60, compare with sec)
% s1        Standard deviation of window
% s2        Standard deviation of window + mean of window (NOT USED)
% s3        ( Standard deviation of window * 4 ) + mean of window
% sec       Seconds (range = 0 to 86400, compare with s)
% str       Filename (fn) converted to a string
% thold     Threshold used to detect tremor, mean of m * 2
% Thresh    Same as thold (except this is an array), used for plotting
% tmp       Temporary location for data file
% Tplot     Used for plotting purposes only, indicative of possible tremor
% TREM      Set to 1 if possible tremor duration exceeds 3 minutes
% Tremor    Tremor detections that remain after comparing all filter banks
% wh        Middle of the window (Int math)
% w         Window size (must be odd), currently set to 5 min and one sec
% x         Data array
% Y         Copy of envelop, used for plotting only
% ye        RMS envelop of filtered data
% y         Filtered data
%
% Function Calls
%
% Butter    [B,A]=butter(filter order,[low corner, high corner])
% rms       ye=rms(data, # of samples per window, sample overlap, padding)
% filter    y=filter([filter coefficients],data to filter)
% ##########       END OF VAR DEF         ##########

clear all; close all;

for fn=<jday>:1:<jday>
    str=sprintf('/home/brian/Desktop/Tremor/DATA/<filename>.%i.<filename>',fn);
    tmp=load(str);
```

```
    x=tmp(1:1728000);   % Save data file to array, 1 day at 20 Hz
    clear load;
    n=size(x,1)/20;     % Array length of envelop function, 1 day at 1 Hz
    w=301;              % Window size, odd for window centering
    wh=int32(w/2);      % Center of window
    Pos=zeros(4,n);     % Possible tremor for each filter bank
    Tremor=zeros(1,n);  % Possible tremor after comparing filter banks
    r=1;     % Counter (range 1 to 4)

% Filter loop
    for bp=1:1:4
        fprintf(1,'%i %i to %i Hz\n',fn,bp,bp+1)
        [B,A]=butter(4,[bp/10, (bp+1)/10]);   % Build Butterworth filter
        y=filter(B,A,x);                      % Filter data
        ye=rms(y, 20, 0, 0);                  % Create RMS envelope
        Y=ye; % Save envelope, used for plotting only
        k=wh;            % Index for storing mean, SD, etc.
        m=zeros(n,1); Thresh=zeros(n,1);   % m = mean of window
        s1=zeros(n,1); s2=zeros(n,1);
        s3=zeros(n,1);          % s1=SD, s2=SD+mean, s3 = SD*4+mean

% Calculate values for first window
        m(1:k)=mean(ye(1:w));        % Value stored at center of window
        s1(1:k)=std(ye(1:w));        % Values prior to center are constant
        s2(1:k)=s1(k)+m(k);          % and equal to center value
        s3(1:k)=(s1(k)*4)+m(k);

% Advance 5 minute window 1 sec at a time
        for i=2:1:n-w+1
            if (ye(i+w-1) > s3(k)) % Check next value BEFORE advancing k
                %ye(i+w-1)=m(k);
                ye(i+w-1)=0;    % These values are spikes, eq's, etc.
            end
            k=k+1;    % Advance k and get the next window
            m(k)=m(k-1) + ( (ye(i+w-1)-ye(i-1) ) / w ); % Calc new values
            s1(k)=std(ye(i:i+w-1));
            s2(k)=s1(k)+m(k);
            s3(k)=(s1(k)*4)+m(k);
        end

% Calculate windows at the END of trace
```

```
        m(k+1:k+wh-1)=m(k);
        s1(k+1:k+wh-1)=s1(k);
        s2(k+1:k+wh-1)=s2(k);
        s3(k+1:k+wh-1)=s3(k);
        thold=mean(m)*2;           % Set tremor detection threshold

% Search 30 sec windows, advance 1 second at a time
% If maximum of window exceeds threshold it's possible tremor
% This is a 4 X n array to hold values for each filter bank
        for i=1:1:n-29
            %if (max(m(1:1+29)) >= thold)
            if (max(ye(i:i+29)) >= thold)
                Pos(r,i)=1;
            end
        end
        r=r+1;
    end % End bp loop

% Check for possible tremor
% Must be present in all filter banks with duration longer than 3 mins
    PosSum=sum(Pos); % If present in all filter banks value will be 4
    Tplot=zeros(1,n); % For plotting purposes
    TREM=zeros(1,n); % Used to store possible tremor hits

    fid=fopen(<filename>, 'a');

    for i=2:1:n
        if (PosSum(i)==4)
            Tremor(i)=Tremor(i-1)+1;    % Check for coherency
        end                             % between all filter banks
        if (Tremor(i)>180 && Tremor(i+1) < 2) % Check 3 min duration
            j=Tremor(i);
            Tplot(i-j+1:i)=thold*10;    % Set possible tremor to yes
            TREM(i-j+1:i)=1;
        end
    end

    % Print array, 1's for possible tremor
    % This file is read by compareFiles.m
    fprintf (fid,'%3i ',fn);
    for i=1:1:n
```

```
        fprintf (fid,'%1i ',TREM(i));
    end
    fprintf (fid,'\n');

    % plot(Tplot,'y')       % Diagnostic

% Diagnostic Section
% Creates trem.pos.txt and contains start and stop times
% of possible tremor - not needed for compareFiles.m
% Store results for start time
% fid2=fopen(<filename>, 'a');  % Open output file
% for i=1:1:n-1
%         if (TREM(i)==1 && TREM(i-1)==0)
%             sec=i; hour=idivide(sec,int32(3600));
%             min=idivide(sec,int32(60))-int32((hour*60)); s=sec -
              int32((hour*3600)) - int32((min*60));
%             fprintf (fid,'%3i %5i %02i:%02i:%02i',fn,sec,hour,min,s);
%         end
%
% % Store results for stop time
%         if (TREM(i)==1 && TREM(i+1)==0)
%             sec=i; hour=idivide(sec,int32(3600));
%             min=idivide(sec,int32(60))-int32((hour*60)); s=sec -
              int32((hour*3600)) - int32((min*60));
%             fprintf (fid,' %5i %02i:%02i:%02i\n',sec,hour,min,s);
%         end
%     end
% fclose(fid2);
end %fn loop
fclose(fid);
```

# compareFiles.m

```
% Program to find coherent tremor between 2 stations
% Brian Bagley
% May 2011
% University of Minnesota
%
% Input is trem_poss_array.[station name].txt (output from detect.m)
% Need to setup station names
% Pick how to count tremor
% i.e. second by second for Parkfield or 5 minute windows for Cascadia
```

```
% ##########     VARIABLE DEFINITIONS     ##########
% c          Column index
% fid2       File name used to save tremor plotting file
% fid        File name used to save coherent tremor times
% hour       Hour
% j          Array index
% M          Flag for which counting method to use
% min        Minute
% n          Number of rows in s1 file
% r          Row index
% s          Seconds (Range 0 to 60 seconds)
% s1         First station file
% s2         Second station file
% sec        Seconds (Range 0 to 86400 seconds)
% t1         Matrix for storing coherent tremor
% t2         Matrix for storing 5 minute segments
% Tcount     Counts cumulative tremor count per day
% tmp        Temp variable for checking array
% ##########       END OF VAR DEF         ##########

clear all;
format long g;

s1=load('/home/brian/Desktop/Tremor/<filename>');
s2=load('/home/brian/Desktop/Tremor/<filename>');
M=1;        % Choose method to count tremor (1 or 5)

% NOTE: M only effects the plot file. The tremor_times file
% will still be second by second

fid=fopen(<filename>, 'a');
fid2=fopen(<filename>,'a');

% Need to make the loop match the number of rows (Days)
% Add the rows for each station to check for coherency among stations
% If tremor is present at both stations sum=2
% First column contains Julian day
% Writes a file that contains the start and stop times for tremor

n=size(s1,1);        % How many rows are there
for r=1:1:n
```

```
    t1(r,1)=s1(r,1);
    t1(r,2:86401)=s1(r,2:86401)+s2(r,2:86401);

    for c=2:1:86401
        if (t1(r,c)==2 && t1(r,c-1)~=2)
            day=t1(r,1);
            sec=c; hour=idivide(sec,int32(3600));
            min=idivide(sec,int32(60))-int32((hour*60));
            s=sec - int32((hour*3600)) - int32((min*60));
            fprintf (fid,'%3i %5i %02i:%02i:%02i',day,sec,hour,min,s);
        end

        if (t1(r,c)==2 && t1(r,c+1)~=2)
            sec=c; hour=idivide(sec,int32(3600));
            min=idivide(sec,int32(60))-int32((hour*60));
            s=sec - int32((hour*3600)) - int32((min*60));
            fprintf (fid,' %5i %02i:%02i:%02i\n',sec,hour,min,s);
        end
    end
end

% Still need to count tremor / day to be used for plotting
% M=1 does second by second

if (M==1)
    for r=1:1:n
        Tcount=sum(t1(r,:)==2);
        fprintf (fid2, '%3i %5i %i\n', t1(r,1), Tcount, Tcount/60);
    end
end

% M=5 looks for tremor in each 5 minute window, if present
% count it as 5 minutes - the Cascadia way

if (M==5)
t2=zeros(r,289);     % Using 289 because 1st window is for jday
    for r=1:1:n
        j=2;
        t2(r,1)=t1(r,1);        % Insert jday into column 1
        for c=2:300:86401       % Search 5 minute windows for tremor
            tmp=ismember([2],t1(r,c:c+299));
```

```
            if (tmp==1)         % If tremor is found
                t2(r,j)=2;      % make 5 min window true
            end
            j=j+1;              % Advance 5 min window index
        end
    end
    % Tcount*5*60 = seconds     Tcount*5 = minutes Tcount*5/60 = hours
    for r=1:1:n
        Tcount=sum(t2(r,:)==2);
        fprintf (fid2, '%3i %5i %i %i\n', t2(r,1), Tcount*5*60, Tcount*5, Tcount*5/60);
    end
end
fclose(fid);
fclose(fid2);
```

# plot_week.m

```
% Brian Bagley
% May 2011
% University of Minnesota
% This script sums the daily output from compareFiles.m
% by week intervals. This makes the plots easier to read
% and compare

clear all; close all;

% NEED TO SET THE ARRAYS TO THE CORRECT COLUMN
% THE COLUMN WHERE MINUTES ARE STORED

col=3;
x=load('/home/brian/Desktop/Tremor/<filename>');

n=size(x,1);    % find number of rows
over=mod(n,7);  % This is the number of extra rows (less than a week)
r=1;

for i=1:7:n-over-6
    total(r,1)=x(i,1);            % set 1st column to jday
    total(r,2)=sum(x(i:i+6,col)); % set 2nd column to week sum
    r=r+1;
end

% This part calculates the sum for the last part that is less
```

```
% than one week
extra=n-over+1;
total(r,1)=x(extra,1);
total(r,2)=sum(x(extra:extra+over-1,col));

% Save the array (total) to a file to plotted by gnuplot
save  <filename> total -ascii
```